



COLLOIDAL GOLD NANOPARTICLES: INTERACTION WITH OZONE AND ANALYTICAL POTENTIAL

Franco Cataldo^{[a,b]*}, Ornella Ursini^[c] and Giancarlo Angelini^[c]

Keywords: gold nanoparticles; spherical particles; nanorods; ozone; ozone detection

Two different types of colloidal gold nanoparticles, produced as hydrosol, are recognized from their electronic absorption spectra. Gold nanorods with aspect ratio in the range between 2 and 4 and average diameter between 10 and 15 nm are produced using AuCl₃ and hydroxylamine. The surface plasmon resonance (SPR) band of gold nanorod undergoes a blue shift of about 50 nm on treatment with ozone. On the other hand, spherical gold nanoparticles with average diameter around 20 nm are produced from AuCl₃ reduced with black tea infusion. When treated with ozone the SPR band of the spherical gold nanoparticles show a red shift of more than 50 nm. This demonstrates that the shape of the gold nanoparticles deeply affects their response in the interaction with chemicals in view of the potential analytical application of gold nanoparticles as active materials in chemical sensors. A theoretical rationalization of the results is proposed.

* Corresponding Authors

E-Mail: franco.cataldo@fastwebnet.it

- [a] Actinium Chemical Research., Via Casilina 1626A, 00133 Rome, Italy
[b] Università della Tuscia, Dipartimento di Scienze Ambientali, Viterbo and Civitavecchia, Italy
[c] CNR–Istituto di Metodologie Chimiche, Area della Ricerca di Montelibretti, Via Salaria Km 29,300, 00016, Monterotondo, Scalo, Rome, Italy

The synthesis of gold nanoparticles is slightly less easier than the silver nanoparticles. However, a number of different synthetic methods are reported in some reviews.¹⁶⁻¹⁹ The shape of the gold nanoparticles can be controlled with a high degree of confidence using tailor-made synthetic approaches.¹⁹⁻²⁴ The resulting surface plasmon resonance (SPR) electronic transition, typical of the gold nanoparticles, is deeply linked to the shape and size of the resulting gold nanoparticles.^{23,24}

Introduction

The formation and stability of silver nanoparticles was studied with the aid of “green” reagents, intended as reducing agents from renewable sources.^{1,2} Tannin is found as an effective reducing agent of Ag⁺ ion in the formation and stabilization of colloidal silver nanoparticles.¹ Similarly, the black and green tea infusions are effective agents in the formation and stabilization of colloidal silver nanoparticles.² The effectiveness of black and green tea infusions as reducing agents is essentially attributed to the polyphenols and other components present in the tea infusions.² Another “green” reducing agent suitable for the preparation of silver nanoparticles is the infusion of *Hibiscus Sabdariffa*, commonly known as “karkadé”.³ The karkadé infusions contain a series of anthocyanins and other components which have a reducing power comparable to that of tea polyphenols.³ Using karkadé infusions it was possible to prepare silver nanoparticles in alkaline solutions by chemical reduction or in neutral-acidic solutions by radiation-induced nucleation reactions.³ The importance of the studies on “green” reducing and capping agents for the synthesis of metal nanoparticles is testified by the numerous reviews.⁴⁻¹¹ Unexpectedly, certain synthetic agents are found as effective as tannin, polyphenols and anthocyanins in the synthesis of colloidal silver nanoparticles.¹²⁻¹⁵ Heavily ozonized C₆₀ fullerene,^{12,13} as well as heavily ozonized C₇₀ fullerene,¹⁴ and ozonized single wall carbon nanohorns (SWCNH)¹⁵ are also as effective agents in the formation and stabilization of colloidal silver nanoparticles.

The interest in gold nanoparticles goes far beyond their antiseptic properties which is far surpassed by the silver nanoparticles.^{2,25-31} In fact, gold nanoparticles find consolidated application as staining medium of tissues and cells in biology and biochemistry microscopy,^{18,19} as well as effective antiarthritic agents.^{32,33} Emerging potential applications of gold nanoparticles regard their quite easy surface functionalization and their use as drugs vector in general and in cancer therapy in particular.^{34,35} Gold nanoparticles are also proposed as contrast agent to enhance the X-ray absorption on cancerous tissues or to enhance heating of tumor tissues in radio-frequency therapy.^{34,35} The anti-angiogenic properties of gold nanoparticles can be employed to inhibit the vascularization of tumor masses.^{34,35} Antiviral properties of functionalized gold nanoparticles were proved on laboratory scale and show great promise for larger scale applications.^{35,36,37} However, safety and toxicological properties of gold nanoparticles in humans and in the environment are object of careful reviews.³⁸ Other fascinating applications of gold nanoparticles regard their use as active materials for chemical and biochemical sensors taking advantage of their optical and electrochemical properties.^{19,23,39}

The present paper is related to the specific use of gold colloid hydrosols as sensitive material for the detection of ozone, and highlights the finding that the shape of gold nanoparticles in the form of nanorods or nanospheres give a completely different response in the interaction with ozone, a key know-how for future analytical applications.

Experimental

Materials and Equipment

$\text{AuCl}_3 \cdot 3\text{H}_2\text{O}$ (Sigma-Aldrich) hydroxylamine hydrochloride (puriss, Fluka) and black tea bags were common commercial samples.

The electronic absorption spectra is studied using a Shimadzu UV2450 spectrophotometer using quartz cuvettes at 20 °C. The reference cuvette is filled with distilled water. Ozone was produced by corona discharge in dry air or oxygen at a rate of 400 mg h^{-1} .

Reduction of $\text{AuCl}_3 \cdot 3\text{H}_2\text{O}$ with hydroxylamine

$\text{AuCl}_3 \cdot 3\text{H}_2\text{O}$ (7.6 mg) was dissolved in 100 ml of distilled water. $\text{NH}_2\text{OH} \cdot \text{HCl}$ (76.3 mg) was added to the gold solution, and the mixture stirred. The reduction reaction was followed spectrophotometrically monitoring the AuCl_3 absorption band at 310 nm. Although there was a disappearance of the band, no evidence for the formation of gold nanoparticles were detected.

Reduction of $\text{AuCl}_3 \cdot 3\text{H}_2\text{O}$ with hydroxylamine at higher dilutions

$\text{AuCl}_3 \cdot 3\text{H}_2\text{O}$ (6 mg) was dissolved in 500 ml of distilled water. $\text{NH}_2\text{OH} \cdot \text{HCl}$ (25 mg) was added to the solution and quickly dissolved. The formation of colloidal gold was immediately observed because the solution turned into a beautiful blue colour. The reduction reaction was followed spectrophotometrically monitoring the colloidal gold surface plasmon resonance band at about 630 nm. Further additions of $\text{AuCl}_3 \cdot 3\text{H}_2\text{O}$ in portions of 5-6 mg each caused a growth in the intensity of the SPR band and the solution changed its color from blue to blue-red although in transparency the solution appeared still deep blue.

Ozone treatment of blue gold hydrosol obtained with hydroxylamine

Blue colloidal gold solution (350 ml), prepared with hydroxylamine reduction as detailed in the previous section, having a nominal gold concentration of 20 mg L^{-1} was transferred in a Drechsel bottle and a mixture of ozone and air was bubbled in the hydrosol. Ozone was produced at a nominal rate of 400 mg h^{-1} . A series of spectra were taken after opportune intervals of time.

Reduction of $\text{AuCl}_3 \cdot 3\text{H}_2\text{O}$ with black tea infusion

Black tea bag (2.0 g) was used to prepare an infusion in 150 ml of hot water for 2 min. Then, 50 ml of the infusion was diluted to a final volume of 450 ml with distilled water. $\text{AuCl}_3 \cdot 3\text{H}_2\text{O}$ (6 mg) was dissolved in the diluted black tea infusion.

The reduction of Au^{3+} started immediately, was followed spectrophotometrically and confirmed by the development of the SPR band. The addition of further $\text{AuCl}_3 \cdot 3\text{H}_2\text{O}$ in portions of 5-6 mg each caused a further increase in the intensity of the SPR band. The resulting solution had a magnificent dark-red color and is stable for months.

Ozone treatment of dark-red gold hydrosol obtained with black tea infusion

The dark-red coloured gold hydrosol (250 ml with a nominal gold content of about 22 mg L^{-1}), prepared as above, was transferred in a Drechsel bottle and a stream of ozone and air was bubbled in the hydrosol. Periodically samples of the solution were taken to record the electronic absorption spectra and to follow the interaction between ozone and the gold particles.

Results and Discussion

Reduction of $\text{AuCl}_3 \cdot 3\text{H}_2\text{O}$ with hydroxylamine

The reduction of AuCl_3 into colloidal gold is not as easy as the reduction of silver into colloidal silver nanoparticles.

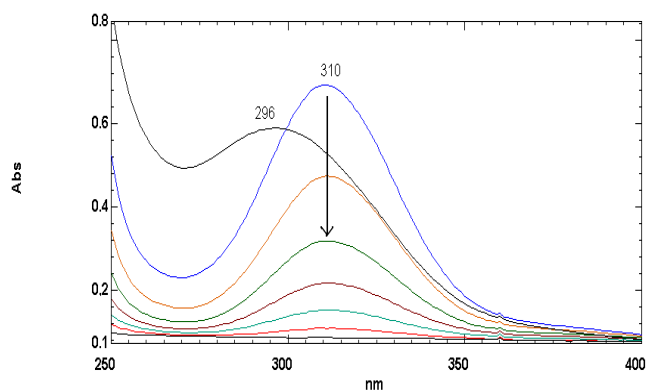


Figure 1. Electronic absorption spectra showing the reduction of the 310 nm absorption band of AuCl_3 by the action of hydroxylamine without the formation of colloidal Au.

Fig. 1 shows the absorption spectrum of a solution of $\text{AuCl}_3 \cdot 3\text{H}_2\text{O}$ (7.6 $\text{mg}/100 \text{ ml}$) with an absorption maximum at 296 nm which is shifted to 310 nm as soon as the reducing agent $\text{NH}_2\text{OH} \cdot \text{HCl}$ is added. The absorption band at 310 nm which is due to the AuCl_4^- anion,⁴⁰ started to decrease in intensity as function of time following pseudo-first order kinetics law as shown in Fig. 2 with a rate constant of $2.2 \times 10^{-3} \text{ s}^{-1}$, and is in agreement with published results.⁴¹ However, the expected growth of the surface plasmon resonance band (SPR) of Au nanoparticles at about 550 nm was not observed with respect to a decrease of the AuCl_4^- anion absorption band.

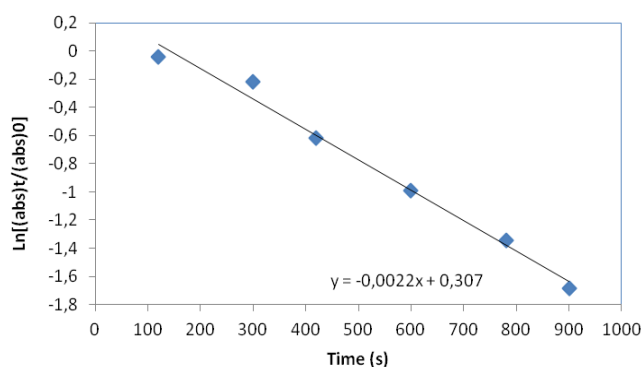


Figure 2. Absorbance data at 311 nm from Fig. 1 plotted according to the pseudofirst order kinetics law showing that the reduction of AuCl_4^- anion occurred with a rate constant of $2.2 \times 10^{-3} \text{ s}^{-1}$.

Therefore, it should be concluded that in the selected reaction conditions the reduction of Au(III) was stopped at Au(I) stage which was stabilized toward the disproportionation reaction $3\text{Au}^+ \rightarrow \text{Au}^{3+} + 2\text{Au}^0$.⁴²

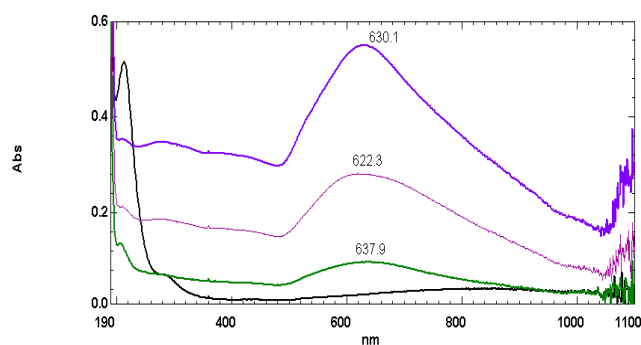


Figure 3. Electronic absorption spectra of gold nanorods. First curve from bottom (black) was taken 2 min after the addition of hydroxylamine to AuCl_3 ; The second curve from bottom (green) is due to the SPR band of colloidal gold taken 5 min after the addition of hydroxylamine. The other two absorption bands (red and violet) on the top were recorded after further additions of AuCl_3 in portions of 6 mg each.

At higher dilutions the just mentioned disproportionation reaction becomes feasible and indeed the formation of blue colloidal gold nanoparticles was observed using $\text{AuCl}_3 \cdot 3\text{H}_2\text{O}$ solutions at a concentration of 1.2 mg/100 ml. Fig. 3 shows the development of the SPR band of gold nanoparticles initially with an absorption peak at 638 nm which is then shifted to 622 nm and then to 630 nm as consequence of further $\text{AuCl}_3 \cdot 3\text{H}_2\text{O}$ additions to the solution. The formation of colloidal Au nanoparticles acts as seeds for further colloidal gold formation. This is the meaning of Fig. 3, where each increase in the optical density of the SPR band corresponds to a further addition of $\text{AuCl}_3 \cdot 3\text{H}_2\text{O}$ which is reduced in its turn. The SPR absorption bands of blue gold nanoparticles shown in Fig.3 between 622 and 638 nm appears considerably broad and suggests that gold nanorods with aspect ratio around 2 to 4 were obtained.^{43,44} In fact, the absorption spectra of gold nanorods is characterized by the dominant SP_1 band (at longer wavelength) corresponding to longitudinal resonance (the peak at 622–630 nm) and a much weaker transverse resonance at shorter wavelength, (about 520 nm) which

appears as a broad shoulder in the spectrum of Fig.3.^{43,44} An additional contribution to the intensity of the SP_1 band is possible by the amount of Au nanospheres which may exist in the dispersions of gold nanorods.⁴³

Ozone effect on gold nanorods

When ozone is bubbled in spherical gold nanoparticles hydrosol, the reduction of the intensity of the SPR band is accompanied by a red shift of the band.^{45–47} The entity of the SPR red shift is of the order of 50 nm toward longer wavelengths for a spherical gold hydrosol with average particles diameter of 7 nm and is reduced to only 10 nm red shift toward longer wavelengths when the gold nanoparticles have an average diameter of 32 nm.⁴⁷ The explanation of this phenomenon which changes also the color of the colloidal solution is based on the chemisorptions of ozone on the surface of gold nanoparticles. The chemisorptions shifts the electron density of the metal particle toward the adsorbate and consequently there is a change in the Fermi level in each particle.⁴⁷

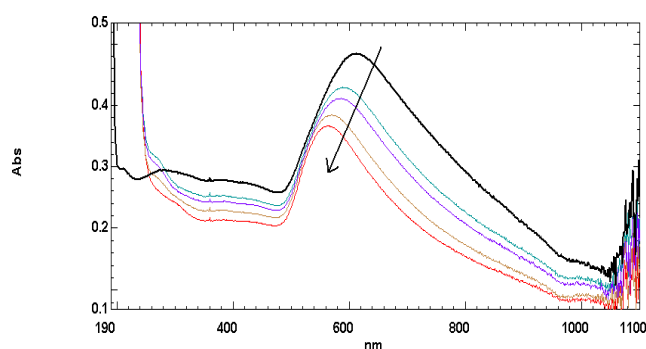


Figure 4. When ozone is bubbled in the colloidal gold nanorods hydrosol the SPR band undergoes a blue shift as indicated by the arrow.

In Fig. 4 is shown for the first time the response of gold nanorods with aspect ratio in the range between 2 and 4 and average diameter between 10 and 15 nm. The trend upon the O_3 adsorption on gold nanorods is exactly opposite to that of spherical nanoparticles reported in literature.^{45–47} This time the SPR band experiences a blue shift, or hypsochromic shift: a shift toward shorter wavelengths, rather than the common and known red shift. Furthermore, the entity of the blue shift from 612 nm to a limiting value of 564 nm, i.e. $\Delta\lambda = -48 \text{ nm}$ is of the same magnitude but opposite sign as that measured on spherical nanoparticles, i.e. $\Delta\lambda \approx 50 \text{ nm}$.⁴⁷ The blue shift effect can be appreciated in Fig. 5, where it is evident that a rapid blue shift $\Delta\lambda = -27 \text{ nm}$ from 612 nm to 585 nm, it follows a relatively slow further blue shift toward the limiting value of 564 nm with a $\Delta\lambda = -48 \text{ nm}$. Curiously, the same trend is observed in Fig. 6 in what is known as hypochromic effect. The absorption intensity of the SPR band falls down with the ozonization time and the shape of the curve of Fig 6 is same as that of the blue shift reported in Fig.5. Thus, not only the SPR band is shifted toward shorter wavelengths but its absorption intensity is also reduced.

Based on these experimental data it looks like that the ozone adsorption on gold nanorods affects almost exclusively the dominant SP_1 band (the component at longer wavelength)

corresponding to longitudinal resonance. The suppression of longitudinal resonance provides evidence in Fig. 4 that the residual transverse resonance which occurs at shorter wavelengths and seems much less affected by the ozone adsorption on gold nanorods.

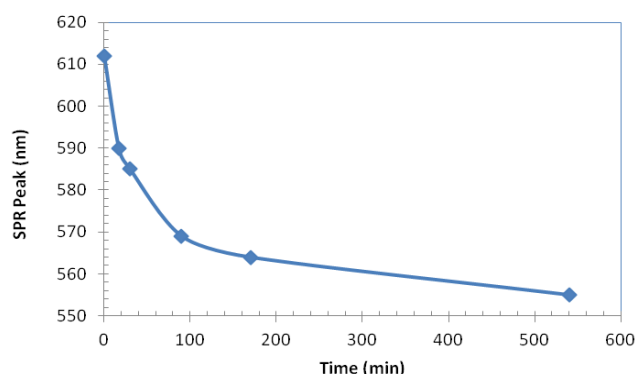


Figure 5. Blue shift of the SPR band when ozone is bubbled in the colloidal gold hydrosol made of nanorods; data from Fig. 4.

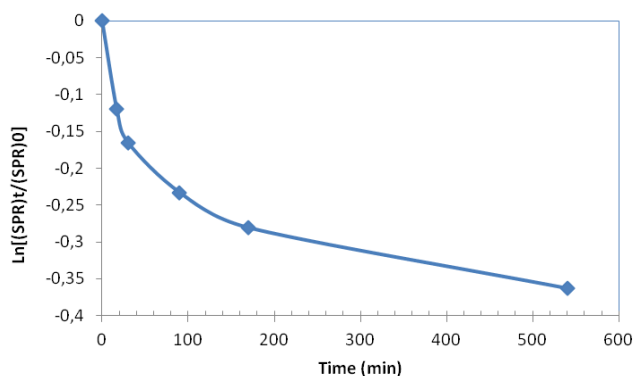


Figure 6. Trend of the SPR band when ozone is bubbled in the colloidal gold nanorod hydrosol; absorbance data from Fig. 4 reported in ordinate as $\ln[(SPR)_t/(SPR)_0]$.

Reduction of $AuCl_3 \cdot 3H_2O$ with black tea infusion

Black and green tea infusions were successfully used as green reducing and capping agents in silver nanoparticles formation.² Black tea infusion was also proposed as a green reducing agent of Au^{3+} with the formation of stable colloidal gold hydrosol.⁴⁸ The mechanism of action of tea infusions in the formation of noble metal colloidal nanoparticles is discussed elsewhere.² The polyphenols present in the tea infusions are the active agents which cause the reduction of silver or gold ions to metal nanoparticles. Furthermore, the mixture of natural products in tea infusion (see reference 2 for a detailed composition) act as excellent capping agents of the metal nanoparticles stabilizing indefinitely the hydrosol. As described in the experimental section, the production of a nice and stable red gold hydrosol was easily achieved by adding $AuCl_3 \cdot 3H_2O$ to a diluted black tea infusion. Fig. 7 shows that the initial absorption of the pristine diluted black tea has no absorption features from 400 to 800 nm (the green absorption curve at the bottom of Fig. 7) and the development of the SPR band at 532 nm as a consequence of the addition of $AuCl_3$ to the diluted black tea infusion.

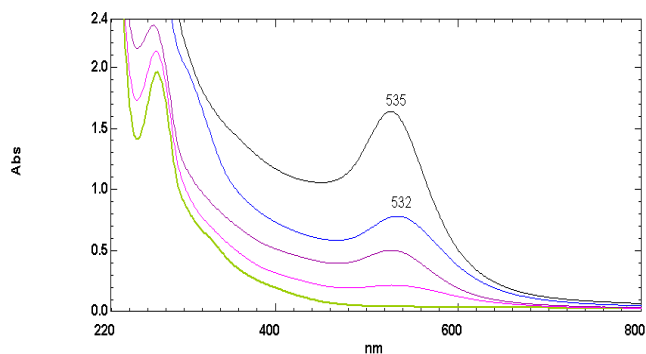


Figure 7. The bottom most green curve is related to pristine black tea absorption; other curves from bottom to top (red, amaranth, blue and black) are the SPR band of gold nanoparticles formed in diluted black tea infusion.

Each absorption curve was taken after the addition of 5-6 mg of $AuCl_3 \cdot 3H_2O$, so the final amount of gold was around 22 mg L^{-1} . The blue curve (fourth from the bottom) in Fig. 7 is the curve obtained after the third addition of $AuCl_3 \cdot 3H_2O$. The absorption curve of the solution left overnight is at the top of Fig. 7 the SPR absorption maximum at 535 nm, slightly shifted to longer wavelengths with respect to the original position at 532 nm. The SPR band in Fig. 7 is narrow and symmetric, completely different than the SPR band discussed in Fig. 3 for gold nanorods. From the SPR peak position, half width of the band and other related considerations,⁴⁹ it is possible to conclude that the colloidal particles produced in diluted tea infusion are spherical with an average diameter of 20 nm.

Ozone effect on spherical gold nanoparticles

Fig. 8 shows the spectral evolution of a gold hydrosol when exposed to a continuous stream of ozone. This time the gold hydrosol is constituted by spherical nanoparticles prepared by the action of black tea infusion on $AuCl_3$, as discussed in the preceding section. From Fig. 8 it is evident that the action of ozone on the Au nanoparticles is causing a shift of the SPR toward longer wavelengths (red or bathochromic shift). This phenomenon is already reported in literature,⁴⁵⁻⁴⁷ and consequently it is confirmed by our experimental results. However, the red shift of the SPR band, is completely in contrast with the results of the preceding experiment discussed in the previous section, when gold nanorods were exposed to ozone showing instead a blue shift in the SPR band position. Since the main difference between the two experiments is the shape of the gold nanoparticles, it can be anticipated here that the shift of the SPR band is deeply affected by the shape of gold nanoparticles.

In Fig. 9 it is reported the entity of the red shift of the SPR band in the case of the spherical gold nanoparticles. At the beginning of the ozonization the shift is from 525 nm to 527 nm and to 529 nm involving a $\Delta\lambda = 4 \text{ nm}$. However, above 90 min of ozone bubbling the SPR band is found at 546 nm with a $\Delta\lambda = 21 \text{ nm}$. Afterwards the hydrosol was left for 45 min saturated with ozone but without any further O_3 bubbling. As shown in Fig. 8 and reported in Fig. 9, the final SPR peak position was found at 587 nm which corresponds to a red shift $\Delta\lambda = 62 \text{ nm}$.

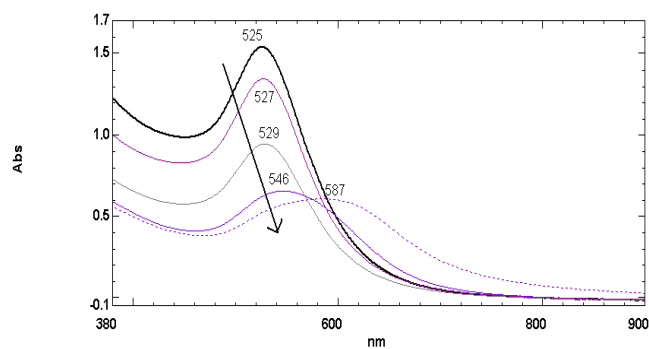


Figure 8. When ozone is bubbled in spherical gold nanoparticles hydrosol there is a red shift of the SPR band as indicated by the arrow.

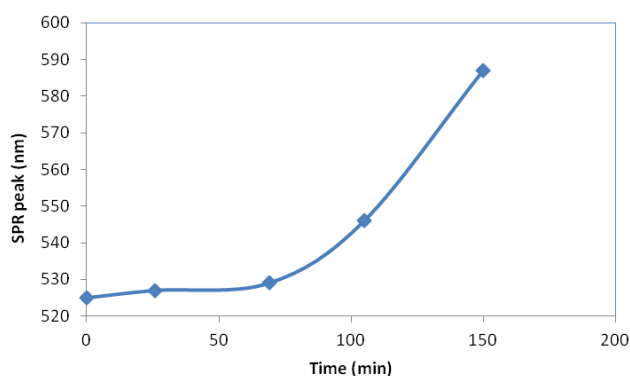


Figure 9. Red shift of the SPR band when ozone is bubbled in the colloidal gold hydrosol of spherical nanoparticles; data from Fig. 8.

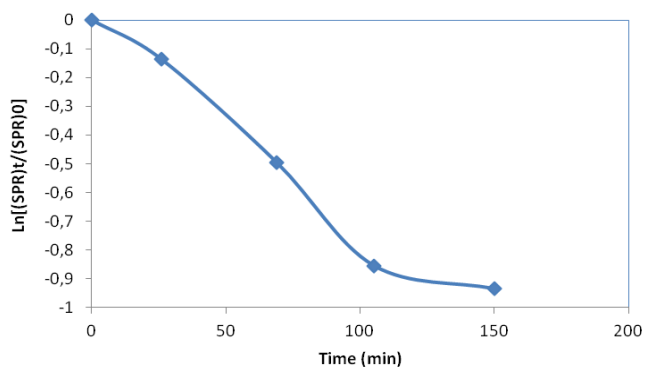


Figure 10. Trend of the SPR band when ozone is bubbled in the colloidal gold hydrosol made of spherical nanoparticles; absorbance data from Fig. 8 reported in ordinate as $\text{Ln}[(\text{SPR})_t/(\text{SPR})_0]$.

A similar trend was observed by other authors in the ozonation of spherical gold hydrosol stabilized with citrate.⁴⁷ In that case the maximum red shift measured was $\Delta\lambda = 50$ nm.⁴⁷ It would be instructive to compare the blue shift of the SPR in gold nanorods in Fig. 5 with the red shift of the SPR band in spherical gold nanoparticles in Fig. 9 during ozone treatment. In the former case the blue shift is quite fast for the first 100 min then reaching slowly to a limiting value. In the latter case the trend is opposite not only because of the red shift but also because the shift is initially slow at the beginning of the ozonation and becomes faster only after 90 min. In view of the potential

application of gold nanoparticles as active sensing material, the gold nanorods seem to ensure a faster response and a higher sensitivity than the spherical gold nanoparticles.

Fig. 10 shows the decreasing absorption intensity of the SPR band as a function of the ozonation time. This hypochromic effect on ozone-treated gold nanoparticles is observed in Fig. 6 and reported in literature.⁴⁷ It can be concluded from the comparison of Fig. 6 with Fig. 10 that in the former case the reduction of the intensity SPR is very fast from the beginning of ozonation and then it slows down, following the same trend of the blue shift. The analysis of the curve in Fig. 6 permits to distinguish two stages as suggested by the two slopes which can be derived from the curve. The first step is suggested by a steep slope. In the case of Fig. 10, the reduction of the intensity of the SPR band practically conforms to the pseudo-first order kinetics law up to 100 min of ozonation and afterwards a kind of “saturation” is reached. It must be remembered here that in Fig. 10 the ozonation was interrupted at 105 min. Thus, the latest step to 150 min was achieved in a quiescent state of the hydrosol saturated with ozone.

Discussion

The practical application of the surface plasmon resonance (SPR) transition of metal nanoparticles is more than a promise in analytical and bioanalytical chemistry.⁵⁰⁻⁵⁴ Indeed, a number of applications are already under development or are being developed under various stages.⁴⁹⁻⁵³ The interaction of gold nanoparticles hydrosol with small molecules was very clearly explained by Ershov and colleagues,⁴⁷ and in greater detail by Girault and collaborators.⁵⁵ In brief, the chemisorptions of a given molecule, for example ozone, on the spherical gold nanoparticle shifts the electron density of the metal nanoparticle toward the adsorbate. This is accompanied by a reduction in the Fermi level of the gold nanoparticle and the colour of the gold hydrosol changes upon the chemisorption of a given molecule.⁴⁷ The change of colour can be measured spectrophotometrically as a shift in the SPR band. In particular the interaction of spherical gold nanoparticles hydrosol produces a red shift of the SPR band, a shift toward longer wavelengths or a bathochromic shift.⁴⁷ In other words, the SPR transition is less energetic after the chemisorption of a molecule. Ershov and colleagues,⁴⁷ have pointed out that the entity of the bathochromic shift is linked to the electron affinity of the analyte being maximum with molecules with high electron affinity (E_A) like O_3 , NO_2 , Cl_2 respectively with $E_A = 2.1$ - 2.4 eV and less pronounced with molecules having lower E_A like SO_2 , O_2 (in the range of 1.1 to 0.5 eV). Furthermore, the entity of the bathochromic shift is linked also with the average diameter of the nanoparticles being maximum for smaller nanoparticles ($d \leq 10$ nm).^{47,55} A similar way to describe the interaction between ozone and gold surface is to compare their respective ionization potentials which are 12.53 eV for the former and 9.226 eV for the latter.⁵⁵ Consequently, it appears obvious that the electrical charge will be displaced from gold surface to the ozone adsorbate. From the entity of the bathochromic or red shift in Fig. 8 and 9 we have measured a $\Delta\lambda = 62$ nm (which refers to the gold nanoparticle electrons displaced toward the adsorbed ozone), a value significantly larger than $\Delta\lambda = 51$ nm found by other authors.⁵⁰ From the bathochromic

shift $\Delta\lambda = 62$ nm it is possible to estimate the bonding energy between ozone and gold nanoparticle surface which is $5.75 \text{ kcal mol}^{-1}$ or $24.07 \text{ kJ mol}^{-1}$. These values suggest more a charge-transfer complex interaction between adsorbent and adsorbate rather than a real chemisorption.⁵⁶

To explain the blue shift or hypsochromic shift observed in the interaction between gold nanorods and ozone as shown in Fig. 4 and 5 it is necessary to admit that in this case electron charges are injected by the adsorbate to the metal surface. This fact will be accompanied by an increase of the Fermi level in the gold nanoparticles and the entity of the SPR blue shift $\Delta\lambda = -48$ nm is quite large as in the case of the red shift discussed previously. Also in this case the energy of the SPR displacement can be calculated to $\approx 4 \text{ kcal mol}^{-1}$ or $16.63 \text{ kJ mol}^{-1}$ in line with the charge-transfer interaction. The blue shift of the SPR band in gold nanorods was detected with electrochemical measurements on a ITO substrate and in other conditions.^{57,58}

The reason of this opposite behavior between spherical gold nanoparticles which give a red shift in the SPR band when they interact with ozone and gold nanorods which instead give a blue shift in the interaction with ozone is explainable by the form of the outer nanoparticle potential which in the case of spherical nanoparticle is described by the following equation:⁵⁵

$$\psi_{\text{spherical}} = \frac{Ze}{4\pi\epsilon r} \quad (1)$$

while for a cylindrical nanoparticle the potential has opposite sign as follows:⁵⁹

$$\psi_{\text{cylinder}} = -\frac{Ze}{2\pi\epsilon} \ln \frac{r}{R} \quad (2)$$

Since the ionization energy of the nanoparticle is given by:⁵⁵

$$I_{\text{E(NP)}} - I_{\text{Ef}} = e\psi \quad (3)$$

and hence

$$I_{\text{Ef}} = I_{\text{E(NP)}} - \frac{Ze^2}{4\pi\epsilon r} \quad (4)$$

$$I_{\text{Ef}} = I_{\text{E(NP)}} + \frac{Ze^2}{2\pi\epsilon} \ln \frac{r}{R} \quad (5)$$

Equation 4 shows that the energy of the Fermi level of the spherical gold nanoparticle is that of the ionization energy of the nanoparticle lowered by the outer potential given by Eqn. 1. This is the case of the red shift of the SPR band and charges donated from the nanoparticle to the adsorbate. Equation 5 instead illustrates the opposite case, that relative

to gold nanorods, where the energy of the Fermi level is due to the ionization energy of the nanorods enhanced by the outer potential given by Eqn. 2. This is the case of the blue shift of the SPR band and charges injected from the adsorbate to the nanoparticle.

Conclusions

Gold nanoparticles interact with ozone giving a large shift in the SPR band. Spherical gold nanoparticles give a red or bathochromic shift of the SPR band in their interaction with O_3 and the electric charges are donated from the adsorbent spherical nanoparticles to the adsorbate ozone molecules lowering the Fermi level of the metal nanoparticles. Gold nanorods interact with ozone more readily than gold nanospheres. Gold nanorods give a blue or hypsochromic shift of the SPR band in their interaction with O_3 and the electric charges are injected by the adsorbate ozone molecule to the adsorbent gold nanorods. The opposite behavior of gold nanospheres and gold nanorods toward ozone can be explained by the different sign and equation form of the potential developed respectively by the two geometrical structures.

References

- Cataldo, F., Ursini, O., Angelini, G., *Eur. Chem. Bull. Sect. B.*, **2013**, 2, 700.
- Cataldo, F., *Eur. Chem. Bull. Sect. B.*, **2014**, 3, 280.
- Cataldo, F., Ursini, O., Angelini, G., *J. Radioanal. Nucl. Chem.*, **2016**, published online, DOI 10.1007/s10967-015-4141-2.
- Sharma, V.K., Yngard, R.A., Lin, Y., *Adv. Colloid Interface Sci.* **2009**, 145, 83.
- Abou El-Nour, K. M. M., Eftaiha, A., Al-Warthan, A., Ammar, R. A. A., *Arabian J. Chem.*, **2010**, 3, 135.
- Tolaymat, T. M., El Badawy, A. M., Genaidy, A., Scheckel, K. G., Luxton, T. P., Suidan, M., *Sci. Total Environ.*, **2010**, 408, 999.
- Moritz, M., Geszke-Moritz, M., *Chem. Eng. J.*, **2013**, 228, 596.
- Mittal, A. K., Chisti, Y., Banerjee, U. C., *Biotechnol. Adv.* **2013**, 31, 346.
- Sharma, T. K., Chopra, A., Sapra, M., Kumawat, D., Patil, S. D., Pathania, R., Navani, N. K., *Int. J. Green Nanotech.*, **2012**, 4, 1.
- Roy, N., Gaur, A., Jain, A., Bhattacharya, S., Rani, V., *Environ. Toxicol. Pharmacol.*, **2013**, 36, 807.
- Kharissova, O. V., Dias, H. V. R., Kharisov, B. I., Olvera Perez, B., Perez, V. M. J., *Trends Biotechnol.*, **2012**, 31, 240.
- Cataldo, F., *Fullerenes, Nanotubes Carbon Nanostruct.*, **2014**, 23, 523.
- Cataldo, F., Iglesias-Groth, S., *Fullerenes, Nanotubes Carbon Nanostruct.*, **2014**, 23, 253.
- Cataldo, F., Hafez, Y., Iglesias-Groth, S., *Fullerenes, Nanotubes Carbon Nanostruct.*, **2015**, 23, 1037.
- Cataldo, F., Putz, M. V., Ursini, O., Hafez, Y., Iglesias-Groth, S., *Fullerenes, Nanotubes Carbon Nanostruct.*, **2015**, 23, 1095.
- Hayat, M. A. (Ed.) "Colloidal Gold: Principles, Methods and Applications" Vol. 1, Academic Press, San Diego, **1989**, Chapter 2.

- ¹⁷Daniel, M. C., Astruc, D., *Chem. Rev.*, **2004**, *104*, 293.
- ¹⁸Mingos, D. M. P. (Ed.) “*Gold Clusters, Colloids and Nanoparticles*”, Structure and Bonding Series Vol. 161, Springer, Heidelberg, **2014**.
- ¹⁹Wikipedia, “*Colloidal Gold*” https://en.wikipedia.org/wiki/Colloidal_gold#cite_note-Sharma.2C_RK_2012-36.
- ²⁰Henglein, A., Meisel, D., *Langmuir*, **1998**, *14*, 7392.
- ²¹Jana, N. R., Gearheart, L., Murphy, C. J., *Adv. Mater.*, **2001**, *13*, 1389.
- ²²Sun, Y., Xia, Y., *Science*, **2002**, *298*, 2176.
- ²³Eustis, S., El-Sayed, M. A., *Chem. Soc. Rev.*, **2006**, *35*, 209.
- ²⁴Grzelczak, M., Pérez-Juste, J., Mulvaney, P., Liz-Marzán, L. M., *Chem. Soc. Rev.*, **2008**, *37*, 1783.
- ²⁵Ho, V. A., Le, P. T., Nguyen, T. P., Nguyen, C. K., Nguyen, V. T., Tran, N. Q., *J. Nanomater.*, **2015**, *2015*, Article ID 241614, 7 pages.
- ²⁶Nisha, M. H., Tamileaswari Sr, R., Jesurani, S., *Int. J. Eng. Sci. Res. Technol.*, **2015**, *4*, 733.
- ²⁷Tufail, A., *J. Nanotech.*, **2014**, *2014*, Article ID 954206, 11 pages.
- ²⁸Cruz, S. M. A., Nogueira, H. I. S., Marques, P. A. A. P., *Ciência Tecnol. Mater.*, **2014**, *26*, 102.
- ²⁹Chekuri, M., Gangarudraiah, S., Roopavatharam, L. B., Kaphle, A., Chalimeswamy, A. *Eur. Chem. Bull.*, **2015**, *4*, 454.
- ³⁰Praba, P. S., Vasantha, V. S., Jeyasundari, J., Jacob, Y. B., *Eur. Chem. Bull.*, **2015**, *4*, 117.
- ³¹Pavliashvili, T., Kalabegishvili, T., Janjalia, M., Ginturi, E., Tsertsvadze, G., *Eur. Chem. Bull.*, **2015**, *4*, 30.
- ³²Brown, C. L., Bushell, G., Whitehouse, M. W., Agrawal, D. S., Tupe, S. G., Paknikar, K. M., Tiekink, E. R., *Gold Bull.*, **2007**, *40*, 245.
- ³³Brown, C. L., Whitehouse, M. W., Tiekink, E. R. T., Bushell, G. R., *Inflammopharmacology*, **2008**, *16*, 133.
- ³⁴Wikipedia, “*Gold Nanoparticles in Chemotherapy*”, https://en.wikipedia.org/wiki/Gold_nanoparticles_in_chemotherapy.
- ³⁵Giljohann, D. A., Seferos, D. S., Daniel, W. L., Massich, M. D., Patel, P. C., Mirkin, C. A., *Angew. Chem. Int. Ed.*, **2010**, *49*, 3280.
- ³⁶Galdiero, S., Falanga, A., Vitiello, M., Cantisani, M., Marra, V., Galdiero, M., *Molecules*, **2011**, *16*, 8894.
- ³⁷Muñoz, A., Sigwalt, D., Illescas, B. M., Luczkowiak, J., Rodríguez-Pérez, L., Nierengarten, I., Holler, M., Remy, J. S., Buffet, K., Vincent, S. P., *Nature Chem.*, **2016**, *8*, 50.
- ³⁸Dwivedi, A. D., Dubey, S. P., Sillanpää, M., Kwon, Y. N., Lee, C., Varma, R. S., *Coord. Chem. Rev.* **2015**, *287*, 64.
- ³⁹Ghosh, S. K., Pal, T., *Chem. Rev.*, **2007**, *107*, 4797.
- ⁴⁰White, R. G., “*Handbook of Ultraviolet Methods*”, Plenum Press, New York, **1965**, methods 1516 and 1518.
- ⁴¹Soni, V., Mehrotra, R. N., Mechanism of the oxidation of hydrazoic acid by tetrachloroaurate (III) ion. *Transition Metal Chem.*, **2008**, *33*, 367-376.
- ⁴²Housecroft, C. E., Sharpe, A. G., “*Inorganic Chemistry*” 3rd Ed., Pearson Education, Harlow, Essex, UK, **2008**, p. 795.
- ⁴³Yu, Y. Y., Chang, S. S., Lee, C. L., Wang, C. R. C., *J. Phys. Chem. B*, **1997**, *101*, 6661.
- ⁴⁴Sharma, V., Park, K., Srinivasarao, M., *Matei. Sci. Eng.*, **2009**, *65*, 1.
- ⁴⁵Puckett, S. D., Heuser, J. A., Keith, J. D., Spindel, W. U., Pacey, G. E. *Talanta*, **2005**, *66*, 1242
- ⁴⁶Pisarenko, A. N., Spindel, W. U., Taylor, R. T., Brown, J. D., Cox, J. A., Pacey, G. E., *Talanta*, **2009**, *80*, 777.
- ⁴⁷Ershov, B. G., Abkhalimov, E. V., Roldughin, V. I., Rudoy, V. M., Dement'eva, O. V., Solovov, R. D., *Phys. Chem. Chem. Phys.*, **2015**, *17*, 18431.
- ⁴⁸Sharma, R. K., Shikha G., Shilpa M., *J. Chem. Educ.*, **2012**, *89*, 1316.
- ⁴⁹Haiss, W., Thanh, N. T., Aveyard, J., Fernig, D. G., *Anal. Chem.*, **2007**, *79*, 4215.
- ⁵⁰Aoki, P. H., Constantino, C. J., Oliveira Jr, O. N., Aroca, R. F., “*Plasmonics in Analytical Spectroscopy*” Chapter 14 in *ACS Symposium Series*, **2015**, *1215*, 43.
- ⁵¹Maier, S. A. “*Plasmonics: fundamentals and applications*.” Springer, Heidelberg, **2007**.
- ⁵²Uechi, I., Yamada, S., *Anal. Bioanal. Chem.*, **2008**, *391*, 2411.
- ⁵³Chon, J. W. M., Iniewski, K. (Ed.), “*Nanoplasmonics: Advanced Device Applications*”, CRC Press, Taylor & Francis Group, Boca Raton, **2014**.
- ⁵⁴Valcarcel, M., Lopez-Lorente, A. I., “*Gold Nanoparticles in Analytical Chemistry*”, Elsevier, Amsterdam, **2014**.
- ⁵⁵Scanlon, M. D., Peljo, P., Méndez, M. A., Smirnov, E., Girault, H. H., *Chem. Sci.*, **2015**, *6*, 2705.
- ⁵⁶Gregg, S. J., “*The Surface Chemistry of Solids*”, Chapman & Hall Ltd, London, **1965**, p.84-95.
- ⁵⁷Novo, C., Funston, A. M., Gooding, A. K., Mulvaney, P., *J. Am. Chem. Soc.*, **2009**, *131*, 14664.
- ⁵⁸Chen, H., Shao, L., Li, Q., Wang, J., *Chem. Soc. Rev.*, **2013**, *42*, 2679.
- ⁵⁹Benenson, W., Harris, J. W., Stocker, H., Lutz, H. (Ed.) “*Handbook of Physics*”, Springer-Verlag, New York, **2002**, p.450.

Received: 14.01.2016.

Accepted: 19.02.2016.



THE LONG TERM EFFECT OF MATERNAL OLIVE OIL SUPPLEMENTATION ON METABOLIC AND REDOX STATUS IN OFFSPRING OF OBESE RATS

Salima Derouiche,^[a] Fatima Zohra Baba Ahmed,^{[a]*} Hafida Merzouk,^[a] Samira Bouanane,^[a] Abdettouweb Saidi,^[a] Sid Ahmed Merzouk^[b] and Narce Michel^[c]

Keywords: Maternal nutrition, metabolic and redox status, olive oil, obesity, offspring.

The aim of this study was designed to determine whether maternal supplementation with olive oil influence plasma lipid profile and oxidant/antioxidant status later in life of rats with cafeteria- diet-fed during gestation and in their offspring throughout adulthood. Altering the fatty acid profile of rat diets during the gestation has long-term consequences for the growth and development of their offspring. Our results clearly demonstrate that maternal intake of olive oil before gestation, during gestation and during lactation display remarkable health benefits for the prevention of obesity and associated metabolic disorders by decreasing the lipoprotein metabolism and oxidant/antioxidant status alterations brought about by obesity in offspring at birth until adulthood.

* Corresponding Authors

Tel: 00 213 558445086

E-Mail: fatimazohra_7@yahoo.fr

- [a] Laboratory of Physiology and Biochemistry of Nutrition, Department of Biology, Faculty of Science of Nature and Life, Sciences of Earth and Universe. Abou Bekr Belkaïd University –Tlemcen-13000, Algeria
- [b] Department of Technical Sciences, Faculty of Engineering, University of Tlemcen 13000, Algeria
- [c] INSERM UMR 866, “Lipids Nutrition Cancer”, University of Burgundy, Faculty of Sciences, 6 Boulevard Gabriel, Dijon 21000, France

adverse effects of maternal obesity on offspring metabolism have been demonstrated, including increased adult body weight and fat mass, reduced insulin sensitivity, increased blood glucose and triglycerides levels, increased lipid deposition and defects in fatty acids metabolism in adult liver, as well as increased leptin levels.^{8,9} Intrauterine oxidative stress can be generated by maternal over nutrition, which increases risk of adult disease.¹⁰

More recently, attention has shifted towards the role of individual components of the maternal diet in affecting fetal and neonatal development. Polyunsaturated fatty acids (PUFA), in particular the ω -3 PUFA alpha-linoleic acid (ALA) and ω -3 long-chain PUFA (LC-PUFA), eicosapentaenoic acid (EPA) and docosahexaenoic acid (DHA), play an important role in fetal development.

It has been reported that a diet enriched in omega-3 long chain polyunsaturated fatty acids (ω -3 LC-PUFA) administered to gestating rats protected against metabolic syndrome which reduced cardiovascular risk.^{11, 12}

Olive oil, the main source of fat in the Mediterranean diet, is rich in unsaturated fatty acids, mainly oleic acid, and phenolic compounds, which contribute to its cardioprotective effects, and has several health benefits prior and during pregnancy on obesity development in offspring.^{13,14,15}

Here, we aimed to assess whether supplementation of maternal cafeteria diet with olive oil before and during gestation has any effect on plasma glucose, lipid profile, and oxidant-antioxidant status of offspring.

Experimental

Animals and Experimental Protocol

Female Wistar rats (aged 1 months, n = 40), weighing 90 to 100 g each, were obtained from Animal Resource Centre (Algeria).

Introduction

Obesity is a major public health issue in both industrialized and semi-industrialized nations across the world, in part because of increasing adoption of a Western diet, high in saturated fat.^{1,2} The development of obesity often results in the onset of further metabolic complications, including insulin resistance and cardiovascular diseases, together termed as metabolic syndrome. Several abnormalities in lipid metabolism have been observed including elevated low-density lipoprotein (LDL) cholesterol, triacylglycerols and apolipoprotein B, and lower high density lipoprotein (HDL) cholesterol concentrations.

Additionally, many studies have shown that obesity is coupled with altered redox state and increased metabolic risk.^{3,4} Oxidative stress can be a consequence but also a trigger of obesity.

Whilst many factors contribute to the development of obesity, there is now an increasing amount of evidence that maternal nutrition during pregnancy and/or lactation is directly related to the adequate development of the fetus, newborn and future adult, likely by modifications in fetal programming and epigenetic regulation, which induce phenotypic changes.⁵

In humans, offspring of obese mothers seem to have increased insulin resistance already at birth, indicating very early life effects on offspring metabolic profile and oxidative stress status.^{6,7} In experimental animals, several

Animals were housed at 20 ± 2 °C with 2-3 in each cage, and maintained on a 12:12 h light/dark cycle. Rats were assigned to each diet group during 8 weeks of experimental period. The control group (control, C, $n=10$) was fed standard laboratory chow (ONAB, Algeria) before and during pregnancy. The second group (cafeteria group, CAF, $n=10$) was fed a fat-rich hypercaloric diet before and during pregnancy. In group three (control olive, CO, $n=10$) rats were on standard chow supplemented with olive oil (5 %) before and during pregnancy. In group four (cafeteria olive oil 5 % (CAFO, $n=10$), rats were on cafeteria diet supplemented with olive oil (5 %) before and during gestation.

The control diet (386 kcal 100 g⁻¹) was composed of 20 % of energy as protein, 20 % of energy as lipids and 60 % of energy as carbohydrates. The components of the cafeteria diet were grinded pâté, cheese, bacon, chips, cookies and chocolate (in a proportion of 2:2:2:1:1:1, by weight) and control diet (mix/control diet) as published previously.¹⁶ The composition of the cafeteria diet (523 kcal 100 g⁻¹) was 16 % of energy as protein, 24 % of energy as carbohydrates and 60 % of energy as lipids. The composition of the four diets is listed in (Table 1). Pure olive oil was obtained from INRA (INRA, Algeria). Fresh food was given daily and body weights were recorded.

After mating, the first day of gestation was estimated by presence of spermatozooids in vaginal smears. Pregnant dams of each group were maintained on their respective diets throughout pregnancy and lactation. After delivery, the newborn rats were continued to feed similar diet of their mothers.

The study was conducted in accordance with the national guidelines for the care and use of laboratory animals. All the experimental protocols were approved by the Regional Ethical Committee.

Blood samples

At birth (day 0), 20 newborn rats in each group (control and experimental) were killed by decapitation, and blood was collected by pooled from four animals as per the protocol of Garcia-Molina et al to obtain sufficient serum samples for chemical determinations.¹⁷

On days 30 and 90 for pups, eight rats from each group were anesthetized with intraperitoneal injection of sodium pentobarbital (60 mg kg⁻¹ of body weight). The abdominal cavity was opened and blood was drawn from the abdominal aorta into EDTA tubes. Blood samples were centrifuged to obtain plasma for glucose, lipids, and oxidant/antioxidant status parameters determinations. After removal of plasma, erythrocytes were washed three times with two volumes of isotonic saline solution. Erythrocytes were lysed with ice-cold distilled water (1/4), stored in the refrigerator at -4 °C for 15 min and the cell debris were removed by centrifugation (2000 g for 15 min). Erythrocyte lysates were assayed for antioxidant enzyme activities.

Chemical analysis

Plasma glucose, total cholesterol (TC), and triacylglycerols (TG) were measured using enzymatic assays kit (Sigma). Plasma creatinine, uric acid and urea were measured using enzymatic colorimetric methods (Kits from BioAssay Systems, CA). Plasma aspartate aminotransferase (AST) (EC 2.6.1.1) and alanine aminotransferase (ALT) (EC 2.6.1.2) activities were determined by the colorimetric method using Randox Diagnostic kits (Randox Laboratories Ltd, Co Antrim, UK), with an interassay CV of 2.8 %.

Table 1. Composition of experimental diets.

Component	Energy sources (% energy)			
	C	CO	CAF	CAFO
Protein	19	18.5	20	20
Carbohydrate	60	60	24	24
Fat	10	10	50	50
Olive oil	/	05	/	5
Vitamin (mg 100 g ⁻¹)	1	1	1	1
Energy values (kcal 100 g ⁻¹)	386	386	523	523
% Fatty acids				
SFA ^α	27	22	42	39.5
C _{18:1} n-9 ^β	24	30	30	33
C _{18:2} n-6	45	44	27	26.5
C _{18:3} n-3	3	3	1	1
C _{20:4} n-6	1	1	0	0

Note: The control and cafeteria diets, in powder form, were supplemented with the purified oils as indicated. α : saturated fatty acids. β : monounsaturated fatty acid Fatty acid composition was analyzed by gas liquid chromatography, INSERM UMR 866, "Lipids Nutrition Cancer", University of Burgundy, France.

Plasma lipoprotein (LDL $d = 1.063$, HDL $d = 1.21$ g mL⁻¹) were separated by sequential ultracentrifugation in a Beckman ultracentrifuge (Model L5-65, 65 Titorot), using sodium bromide for density adjustment. HDL cholesterol and LDL cholesterol concentrations were also measured by enzymatic kits (Sigma).

Erythrocyte reduced glutathione (GSH) was determined using 5, 5-dithiobis-2-nitrobenzoic acid (DTNB or Ellman reagent).¹⁸ Superoxide dismutase (SOD) (EC 1.15.1.1) activity was measured by the NADPH oxidation procedure.¹⁹

The radical nature of NOS and its short half-life make the measure of its production so difficult. Thus the determination of stable products of NOS, nitrite and nitrate, is used to determine NOS concentration. The procedure comprises two steps; the first step consists in chemical reduction of nitrate to nitrite by cadmium, followed by the spectrophotometric detection of nitrite at 540 nm.²⁰

Superoxide level determination in plasma was based on the superoxide anion mediated nitro blue tetrazolium (NBT) reduction to monofarmazan, a chromophor that absorbs at 550 nm.²¹

Table 2. Body weight of the studied rats.

Sample	Control rats		Cafeteria obese rats		p (ANOVA)
	C	CO	CAF	CAFC	
Mothers					
BW before pregnancy	164.70±3.08 ^c	161.14±1.25 ^c	244.38±2.91 ^a	186.39±1.78 ^b	0.0001
BW at the end of pregnancy	219.39±10.09 ^b	216.47±4.12 ^b	331.33±2.80 ^a	210.26±5.36 ^b	0.0001
Offspring					
BW at birth	4.90±0.35 ^c	5.42±0.64 ^b	7.97±0.28 ^a	5.93±0.54 ^b	0.0001
BW on 30th day	57.04±4.00 ^b	68.16±4.62 ^b	78.5±1.87 ^a	70.83±3.60 ^b	0.0001
BW on 90th day	190.48±2.36 ^b	196.5±13.08 ^b	266.83±6.49 ^a	261±3.34 ^a	0.0001

Note: BW = body weight in g. Values are presented as means ± standard deviations (SD). C: rats fed control diet, CAF: obese rats fed cafeteria diet, CO 5 %: rats fed control diet enriched with olive oil at 5 %, CAFO 5 %: obese rats fed cafeteria diet enriched with olive oil at 5 %. Values with different superscript letters (a, b, c, d) are significantly different ($P < 0.05$).

Statistical analysis

Results are expressed as means ± standard deviation (SD). The results were tested for normal distribution using the Shapiro-Wilk test. Data not normally distributed were logarithmically transformed. Significant differences among the groups were analyzed statistically by a one-way analysis of variance (ANOVA). When significant changes were observed in ANOVA tests, Fisher least significant difference tests were applied to locate the source of significant difference. The individual effects of the diets and the oil supplementations were distinguished by two-way ANOVA. The significance level was set at $P < 0.05$. These calculations were performed using STATISTICA version 4.1 (STATSOFT, Tulsa, OK).

Results

Body weight

The cafeteria diet consumption led to significantly higher body weight as compared with standard chow in both mothers and their offspring. However, supplementation with olive oil at 5 % induced a significant reduction in body weight in both control and obese rats of mothers and their offspring ($p = 0.0001$) but had no effects on the offspring of CAFO group at the ages of 1 and 3 months (Table 2).

Plasma biochemical parameters

Plasma glucose, urea, creatinine, uric acid, AST and ALT activities were significantly higher in diet induced obese rats fed on basal cafeteria diet (CAF). Oil supplementation induced a significant reduction in CAF group but had no effects on the CO group. Neither the cafeteria diet nor oil supplementation affected APL activities in the offspring, as revealed by 2-way ANOVA (Table 3).

Lipid and lipoproteins concentrations

Blood levels of triglycerides and cholesterol decreased in the group fed with olive oil compared with the other samples (Table 4). We also note a decrease in LDL-C in the offspring of control rats and rats treated with olive oil compared with obese rats. However, the plasma levels of

HDL-C are increased in control rats and rats treated with olive oil compared to obese rats in offspring at birth (Table 4).

Oxidative stress biomarkers

Erythrocyte antioxidant enzyme activities were markedly different among the four groups studied. The SOD and GSH activities were significantly higher ($p < 0.05$) in rat adult offspring feeding with cafeteria. The administration of olive oil at 5 % to obese rats leads to an increase in GSH and SOD activities in both control (CO) and obese treated rats (CAFO). There is no significant difference of oxidants and antioxidants results in offspring at birth and at weaning (Figure 1). A significant increase was observed in the levels of plasma NO, O₂ in cafeteria group compared to control group and supplemented groups with olive oil (CO, CAFO) (Figure 2).

Discussion

The intake of an excess of fat during pregnancy and lactation may have negative consequences on the metabolic health of offspring in the long term. In the present study, a palatable cafeteria diet was given to dams 8 weeks before mating to induce long-term dietary obesity in breeders. Maternal cafeteria diet feeding induced a marked reduction in body weight, an increase in serum glucose, cholesterol, triglyceride, urea acid, urea, creatinine, aminotransferases and lipid concentrations in offspring at birth and they remained obese throughout adulthood, in agreement with previous studies.^{8,9}

A higher foetal weight of high fat fed dams may be caused by changes in nutritional transport through placenta, either up-regulation of specific nutrition's like glucose and amino acids indicating from higher protein gene expression of glucose transport Glut 4 and sodium coupled neutral amino acid transport SANAT 2 or either to the ability of placenta to take up chylomicron remnants core lipids by increasing mRNA expression of fatty acid oxidation protein PPAR rather than fatty acid transport.^{22,23} Currently, we know that a diet rich in saturated fatty acids might lead to changes in the action of insulin, with hyperglycemia, increased body mass, and a systemic pro-inflammatory state, which can be transmitted to other generations.²⁴

Table 3. Effect of the different diets on the biochemical parameters of the offsprings.

Parameter	Control rats		Cafeteria obese rats		P (ANOVA)
	C	CO	CAF	CAFO	
At birth					
Glucose (mg dL ⁻¹)	64.02±1.21 ^d	89.62±1.02 ^b	92±1.16 ^a	85.07±0.72 ^c	0.0001
Creatinine (mg dL ⁻¹)	4.08±0.31 ^c	4.00±0.24 ^c	6.46±0.35 ^a	5.17±0.33 ^b	0.0001
Uric acid (mg dL ⁻¹)	22.80±0.91 ^b	23.07±2.04 ^b	56.34±2.84 ^a	26.57±3.25 ^b	0.01
Urea (mg dL ⁻¹)	17.10±0.01 ^b	17.71±0.91 ^b	36.19±0.92 ^a	19.02±0.99 ^b	0.0001
GTO (UI L ⁻¹)	31.99±0.71 ^c	31.98±0.71 ^c	51.51±0.67 ^a	41.02±0.74 ^b	0.0001
GTP (UI L ⁻¹)	28.04±2.68 ^c	26.99±1.01 ^c	42.79±0.76 ^a	32.65±0.91 ^b	0.0001
ALP (UI L ⁻¹)	86.17±4.47 ^a	88.29±3.48 ^a	84.83±5.20 ^a	86.92±4.18 ^a	0.2438
Day 30					
Glucose (mg dL ⁻¹)	79.83±7.13 ^c	90.45±13.98 ^b	100.29±4.61 ^a	81.36±4.47 ^c	0.0001
Creatinine (mg dL ⁻¹)	5.33±0.33 ^b	5.07±0.13 ^b	7.98±0.10 ^a	5.65±0.45 ^b	0.01
Uric acid (mg dL ⁻¹)	35.38±0.93 ^b	39.19±1.64 ^b	72.77±1.82 ^a	39.44±2.73 ^b	0.0001
Urea (mg dL ⁻¹)	22.34±6.20 ^c	23.97±1.72 ^c	58.66±2.44 ^a	29.73±0.96 ^b	0.0001
GTO (UI L ⁻¹)	36.86±4.00 ^b	34.11±3.18 ^b	50.51±0.71 ^a	40.03±3.04 ^b	0.0001
GTP (UI L ⁻¹)	26.99±1.02 ^d	32.65±0.91 ^c	49.15±0.83 ^a	41.51±0.99 ^b	0.0001
ALP (UI L ⁻¹)	100.77±3.87 ^a	103±5.44 ^a	99.76±1.53 ^a	101.10±4.11 ^a	0.4152
Day 90					
Glucose (mg dL ⁻¹)	87.2±8.53 ^b	86.33±8.18 ^b	140±11.33 ^a	121±17.43 ^a	0.0001
Creatinine (mg dL ⁻¹)	9.3±0.42 ^b	9.63±0.47 ^b	12.16±0.87 ^a	9.95±0.95 ^b	0.0001
Uric acid (mg dL ⁻¹)	47.66±1.82 ^b	44.48±1.43 ^c	57.74±4.35 ^a	40.70±1.89 ^c	0.0001
Urea (mg dL ⁻¹)	25.38±1.00 ^b	26.52±1.11 ^b	54.12±0.72 ^a	26.74±0.83 ^b	0.0001
GTO (UI L ⁻¹)	46.85±0.58 ^c	44.05±0.68 ^c	56.40±0.70 ^a	51.14±0.81 ^b	0.0001
GTP (UI L ⁻¹)	42.45±1.47 ^b	42.06±1.34 ^b	52.94±0.88 ^a	41.54±5.29 ^b	0.0001
ALP (UI L ⁻¹)	83.35±4.15 ^b	87.66±2.80 ^a	84.34±4.62 ^b	88.33±3.83 ^a	0.0341

Note: Values with different superscript letters (a, b, c, d) are significantly different ($p < 0.05$).

Table 4. Lipid and lipoprotein concentrations in the offsprings.

Parameter	Control rats		Cafeteria obese rats		P (ANOVA)
	C	CO	CAF	CAFO	
At birth					
TG (mg dL ⁻¹)	30.10±2.16 ^b	23.46±3.03 ^c	56.28±1.78 ^a	33.45±2.98 ^b	0.0001
TC (mg dL ⁻¹)	40.32±1.41 ^b	32.77±3.12 ^c	61.83±2.25 ^a	42.92±3.95 ^b	0.0001
LDL (mg dL ⁻¹)	13.23±0.88 ^b	9.99±1.16 ^c	20.73±1.69 ^a	13.46±0.76 ^b	0.0001
HDL (mg dL ⁻¹)	20.15±1.61 ^c	25.13±1.19 ^b	30.46±1.55 ^a	26.55±1.87 ^b	0.0001
Day 30					
TG (mg dL ⁻¹)	63.03±1.64 ^b	31.40±1.80 ^d	87.78±2.58 ^a	57.93±2.97 ^b	0.0001
TC (mg dL ⁻¹)	103.82±7.20 ^b	95.6±4.36 ^c	150.23±2.44 ^a	120.39±14.10 ^b	0.0001
LDL (mg dL ⁻¹)	30.47±1.73 ^c	16.27±2.09 ^d	56.73±2.77 ^a	44.84±4.86 ^b	0.0001
HDL (mg dL ⁻¹)	57.55±1.91 ^a	60.75±4.82 ^a	58.09±1.36 ^a	56.56±1.85 ^a	0.0003
Day 90					
TG (mg dL ⁻¹)	89.46±1.93 ^b	60.89±2.12 ^d	133.72±3.49 ^a	79.67±1.78 ^c	0.0001
TC (mg dL ⁻¹)	121.42±5.92 ^b	104.91±10.76 ^c	160.53±2.62 ^a	137.63±18.33 ^a	0.0001
LDL (mg dL ⁻¹)	35.31±2.34 ^b	20.10±1.37 ^c	53.79±1.80 ^a	33.86±2.87 ^b	0.0001
HDL (mg dL ⁻¹)	62.12±1.99 ^a	53.36±2.11 ^b	41.16±2.23 ^c	58.42±1.33 ^a	0.0001

Note: TG = triglycerides, TC = total cholesterol, LDL-C = LDL cholesterol, HDL-C = HDL cholesterol. Values with different superscript letters (a, b, c, d) are significantly different ($p < 0.05$).

A cafeteria diet is frequently associated with alterations in the plasma oxidative stress in rodent models. In our study, the offspring of obese dams presented the elevated levels of plasma nitric oxide, superoxide anion and proteins carbonyl accompanied by attenuated antioxidant enzymes' activities remains to the adulthood in agreement with previous studies.²⁵

The high antioxidant capacity of olive oil, the main source of fat in the Mediterranean diet, has been attributed to its richness in phenolic compounds with high antioxidant capacity, e.g., hydroxytyrosol, tyrosol, oleuropein aglycon and its derivatives, and to the high proportion of monounsaturated fatty acids (MUFA), namely oleic acid, which are naturally found in extra virgin olive oil

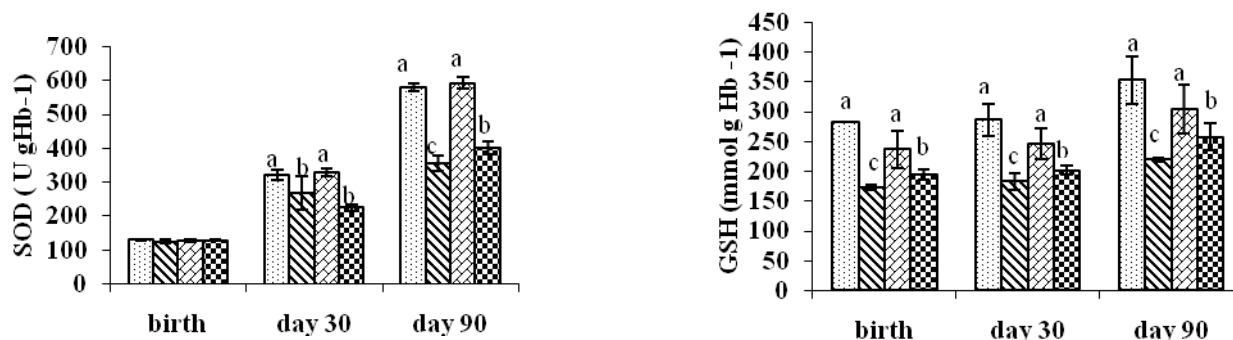


Figure 1. Erythrocyte antioxidant status in control and experimental rats. Values are presented as means \pm standard deviations (SD). SOD: superoxide dismutase, GSH: reduced glutathione. Values with different superscript letters (a, b, c, d) are significantly different ($p < 0.05$)

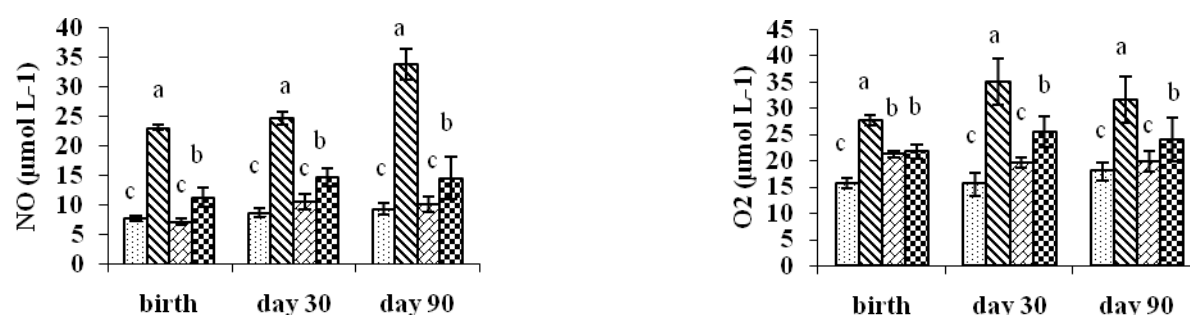


Figure 2. Plasma oxidant markers in control and experimental rats. NO = nitric oxide; O₂ = superoxide anion. Values with different superscript letters (a, b, c, d) are significantly different ($p < 0.05$).

Here, in an animal model of high-fat-diet-induced obesity, we show that maternal supplementation with olive oil at 5 % before gestation, during gestation and during lactation favorably affects body weight, biochemical parameters, lipid profile, and oxidant/antioxidant status in offspring at birth, on day 30 and on day 90.

In comparison to the control group, the obese (CAF) dams continued to get more body weight during gestation period, these may be related to increased fetal and placental weight, but supplementation of olive oil reduced gestational weight. These results may attribute to many factors, either the types of unsaturated fat (monounsaturated) or to the quantity of these fat in the diet or to the period of the experiment had an effect on the results. Our findings agreed with Sanaa Jameel Thamer et al study but they use olive oil 22.5 % after 12 weeks of high fat diet and before mating.¹⁵

Maternal olive oil supplementation results in a lower body weight of offspring at birth, but had no effects in obese offspring at weaning and at adulthood; however, under the challenge of a cafeteria diet, these animals show a greater increase in body weight and fat content. Animal studies have shown considerable disparity of this regard. In studies carried out in rats, a high fat maternal diet enriched in olive oil led to reduce postnatal weight gain in some studies, while other studies found no effect.^{26, 27}

Our data show that maternal dietary fatty acid balance does influence the development of the offspring. This becomes apparent in plasma glucose, urea, creatinine, uric acid and liver enzymes especially in cafeteria fed obese offspring, in agreement with previous reports,²⁸ but there is no effect on levels of ALP.

Laws *et al* using maternal diet supplementation with 10 % extra energy of olive oil (rich in MUFA) in the first half (G1) or second half of gestation, showed that MUFA supplementation during G1 reduced the incidence of low birth weight in piglets.²⁹

Furthermore, our study demonstrated that diet enriched with olive oil (5 %) considerably ameliorates lipid and lipoprotein disorders associated with higher HDL-cholesterol and lower LDL-cholesterol in offspring at birth and throughout adulthood. There is no significant difference in cholesterol values between CAFO and CAF at day 90 but remain within physiological limits.

Nitric oxide (NO) plays an important role in inflammatory process. Macrophages may greatly produce both levels of NO and superoxide, which rapidly react with each other to form peroxynitrite which oxidizes LDL, a key process in atherosclerosis. As it is recorded in our study, in obese offspring, maternal olive oil supplementation caused a reduction in plasma nitric oxide and superoxide anion with a concomitant increase in antioxidant enzyme activities.

We also observed a trend toward increase activity of glutathione reductase, which protects the mitochondrial inner membrane from oxidative stress damage. These findings are consistent with many studies that have shown that the antioxidant properties of olive oil are mainly due to its high content of polyphenolic compounds, which are strong antioxidants and radical scavengers.³⁰

Conclusion

Fetal programming has been a growing target of interest in scientific research, especially from the nutritional perspective. Our results clearly demonstrate that maternal intake of olive oil before gestation and during gestation display remarkable health benefits for the prevention of obesity and associated metabolic disorders by decreasing the lipoprotein metabolism and oxidant/antioxidant status alterations brought about by obesity in offspring at birth until adulthood.

Acknowledgments

This work was supported by the French Foreign Office (International Research Extension Grant TASSILI 08MDU723) and by the Algerian Research Project (PNR, 2011).

The authors declare that they have no conflicts of interest.

References

- ¹World Health Organisation., **2006**, <http://www.who.int/mediacentre/factsheets/fs311/en/print.html>.
- ²Rivera, C. A., Gaskin, L., Singer, G., Houghton, J., Allman, M., *BMC. Physiol.*, **2010**, 10, 20–27
- ³Warolin, J., Coenen, K. R., Kantar, J. L., Whitaker, L. E., Wang, L., Acra, S. A., Roberts, L.J., Buchowski, M. S., *Pediatr. Obes.*, **2014**, 9, 43-52.
- ⁴Karaouzene, N., Merzouk, H., Aribi, M., Merzouk, S. A., Berrouiguet, A. Y., Tessier, C., Narce, M., *Nutr. Metab. Cardiovasc. Diseases*, **2011**, 21, 792–799.
- ⁵Desai, M., Jellyman, J. K., Ross, M. G., *Int. J. Obes.*, **2015**, 39, 633–641.
- ⁶Catalano, P. M., Presley, L., Minium, Hauguel-de Mouzon, S., *Diabetes Care*, **2009**, 32, 1076-80.
- ⁷Malti, N., Merzouk, H., Merzouk, S. A., Loukidi, B., Karaouzene, N., Malti, A., Narce, M., *Placenta.*, **2014**, 35, 411-6.
- ⁸Mucellini, A. B., Goularte, J.F., de Araujo da Cunha, A. C., Caceres, R. C., Noschang, C., da Silva Benetti, C., Silveira, P. P., Sanvitto, G. L., *Brit. J. Nutr.*, **2014**, 111, 1499-506.
- ⁹Bouanane, S., Merzouk, H., Benkalfat, N. B., Soulimane, N., Merzouk, S. A., Gresti, J., Tessier, C., Narce, M., *Metabolism*. **2010**, 59, 1701–1709.
- ¹⁰Thompson, LP., Al-Hasan, Y., *J. Pregnancy.*, **2012**, 582748.
- ¹¹Kasbi-Chadli, F., Boquien, C-Y., Simard, G., Ulmann, L., Mimouni, V., Leray, V., Meynier, A., Ferchaud-Roucher, V., Champ, M., Nguyen, P., Ouguerram, K., *J. Nutr. Biochem.* **2014**, 25, 726–733
- ¹²Lorente-Cebrian, S., Costa, A. G., Navas-Carretero, S., Zabala, M., Martinez, J. A., Moreno-Aliaga M. J., *J. Physiol Biochem*, **2013**, 69, 633–651.
- ¹³Martín-Peláez, S., Covas, M. I., Fitó, M., Kušar, A., Pravst, I., *Mol. Nutr. Food Res.*, **2013**, 57, 760-771.
- ¹⁴Bogani, P., Galli, C., Villa, M., Visioli, F., *Atherosclerosis*, **2007**, 190, 181-186.
- ¹⁵Suker, D. K., Thamer, S. J., Al Taha, T. J., *Eur. J. Exp. Biol.*, **2013**, 3, 191-198
- ¹⁶Darimont, C., Yurini, M., Epitoux M, Zbinden, I., Richelle, M., Montell, E., Martinez, A. F., Mace, K., *Nutr. Metab.* **2004**, 1, 4-12.
- ¹⁷Garcia-Molina, V., Aguilera, Ja., Gil, A., Sdnchez-Pozo, A., *Comp. Biochem. Physiol.* **1996**, 113b, 789-793.
- ¹⁸Goldberg, D. M., Spooner, R. J., *Methods Enzym. Anal. (3rd Ed)*, **1992**, 258-265.
- ¹⁹Elstner, E. F., Youngman, R. J., Obwad, W., *Methods Enzym. Anal.*, 3rd Ed., **1983**, 293-302.
- ²⁰Guevara. I. Iwaneiko. J., Dembińska-Kieć. A., Pankiewicz. J., Wanat. A., Anna. P., Gołabek, I., Bartuś, S., Malczewska-Malec, M., Szczudlik. A., *Clin. Chim. Acta*, **1998**, 274, 177–188
- ²¹Auclair, C., Voisin, E., Greenworld, R. A., (Ed.), *Handbook of Methods for Oxygen Radical Research*, CRC Press, Inc., Boca Raton., **1985**, 123–132
- ²²Jones, H. N., Woollett, L. A., Barbour, N., Prasad, P. D., Powell, T. L., Jansson, T., *FASEB J.*, **2009**, 23, 271.
- ²³Sandra, L. R., Katie, T. B., Qing, Y., Patrick, T. S. O., Laura, A. W., *Am. J. Physiol. Endocrinol. Metab.*, **2011**, 301,416.
- ²⁴King, V., Dakin, R. S., Liu, L., Hadoke, P. W., Walker, B. R., Seckl, J. R., Norman, J. E., Drake, A. J., *Endocrinology*, **2013**, 154, 2514-24.
- ²⁵Bouanane, S., Benkalfat, B. N., Baba Ahmed, F. Z., Merzouk, H. S. Mokhtari, N., Merzouk, S. D., Gresti, J., Tessier, C., Narce, M., *Clin. Sci.*, **2009**, 116, 669-680.
- ²⁶Llopis, M., Sanchez, J., Priego, T., Palou, A., Pico, C., *J. Agric. Food Chem.*, **2014**, 62, 1590–1601.
- ²⁷ Sánchez, J., Priego, T., García, A. P., Llopis, M., Palou, M., Picó, C., Palou, A., *Mol. Nutr. Food. Res.*, **2012**, 56, 1715-28.
- ²⁸Salem, A. A., Elsayy, H. A., Gabal., S. S., *Int. J. Nutr. Food Sci.*, **2015**, 4, 509-517.
- ²⁹Law, J., Litten, J. C., Laws, A., Lean, I. J., Dodds, P. F., Clarke, L., *Brit. J. Nutr.*, **2009**, 101, 240-249.
- ³⁰Visioli, F., De La Lastra, C. A., Andres-Lacueva, C., Aviram, M., Calhau, C., Cassano, A., D'Archivio, M., Faria, A., Favé, G., Fogliano, V., Llorach, R., Vitaglione, P., Zoratti, M., Edeas, M., *Crit. Rev. Food Sci. Nutr.*, **2011**, 51, 524-46.

Received: 25.01.2016.

Accepted: 19.02.2016.



STRUCTURE OF 2-AMINO-4-(3-BROMOPHENYL)-7,7-DIMETHYL-5-OXO-5,6,7,8-TETRAHYDRO-4H-CHROMENE-3-CARBONITRILE

Balbir Kumar^[a], Goutam Brahmachari^[b], Bubun Banerjee^[b], Khondekar Nurjamal^[b], Rajni Kant^[a] and Vivek K. Gupta^{[a]*}

Keywords: Crystal structure, direct methods, hydrogen interactions.

The title compound, 2-amino-4-(3-bromophenyl)-7,7-dimethyl-5-oxo-5,6,7,8-tetrahydro-4H-chromene-3-carbonitrile (C₁₈H₁₇BrN₂O₂), was synthesized, in 86% yield, by one-pot multicomponent reaction of 3-bromobenzaldehyde, malononitrile and dimedone using 10 mol % urea as an organo-catalyst at room temperature. It crystallizes in the monoclinic space group C 2/c with the unit-cell parameters: a= 23.557(2), b= 9.2963(7), c= 15.7502(12) Å, β = 93.430(8)° and Z = 8. The crystal structure was solved by direct methods using single-crystal X-ray diffraction data collected at room temperature and refined by full-matrix least-squares procedures to a final R-value of 0.0585 for 1411 observed reflections. The packing between the molecules within the unit cell is stabilized by N-H...O and N-H...N type of intermolecular hydrogen interactions.

*Corresponding Author

Mob: +919419102467

E-Mail: vivek_gupta2k2@hotmail.com

[a] X-ray Crystallography Laboratory, Post-Graduate

Department of Physics & Electronics,

University of Jammu, Jammu Tawi - 180006, India

[b] Laboratory of Natural Products & Organic Synthesis,

Department of Chemistry, Visva-Bharati, Santiniketan –

731235, West Bengal, India.

Introduction

4H-Pyran-annulated heterocyclic scaffolds represent a “privileged” structural motif well distributed in naturally occurring compounds¹⁻³ with a broad spectrum of significant biological activities.⁴⁻⁷ Recently, a series of synthetic 2-amino-3-cyano-4H-pyrans have been evaluated to possess potent anticancer,⁸⁻¹¹ antibacterial and antifungal,^{12,13} and anti-rheumatic¹⁴ properties. In this communication, we wish to report on one-pot facile synthesis of a novel 4H-pyran-annulated heterocyclic compound, namely 2-amino-4-(3-bromophenyl)-7,7-dimethyl-5-oxo-5,6,7,8-tetrahydro-4H-chromene-3-carbonitrile via multi-component reaction (MCR) at room temperature using commercially available urea as inexpensive and environmentally benign organo-catalyst, and determination of its crystal structure. The structure of the title compound was elucidated by spectral methods and XRD studies.

Experimental

Synthesis

An oven-dried screw cap test tube was charged with a magnetic stir bar, 3-bromobenzaldehyde (0.183 g, 1 mmol), malononitrile (0.066 g, 1.1 mmol), urea (0.007 g, 10 mol % as organo-catalyst), and EtOH:H₂O (1:1 v/v; 4 mL) in a sequential manner; the reaction mixture was then stirred vigorously at room temperature for about 20 min. After that, dimedone (0.140 g, 1 mmol) was added to the stirred reaction mixture, and the stirring was continued for 6 h.¹⁵ The progress of the reaction was monitored by TLC. On completion of the reaction, a solid mass precipitated out that

was filtered off followed by washing with aqueous ethanol to obtain crude product. It was purified just by re-crystallization from ethanol without carrying out column chromatography. The structure of title compound was confirmed by analytical as well as spectral studies including FT-IR, ¹H NMR, ¹³C NMR, and TOF-MS.

Unit crystal was obtained from DMSO as a solvent. For crystallization 50 mg of compound dissolved in 5 mL DMSO and left for several days at ambient temperature which yielded white block shaped crystals. The chemical structure of the title compound is given in Figure 1.

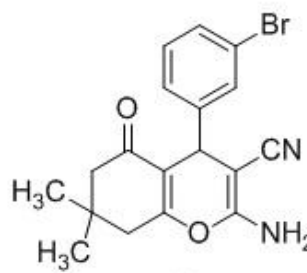


Figure 1. Chemical diagram of title compound

Characterisation

Infrared spectra were recorded using a Shimadzu (FT-IR 8400S) spectrophotometer using KBr disc. ¹H and ¹³C NMR spectra were obtained at 400 and 100 MHz, respectively, using a Bruker DRX-400 spectrometer and DMSO-*d*₆ as the solvent. Mass spectra (TOF-MS) were measured on a QTOF Micro mass spectrometer. Elemental analyses were performed with an Elementar Vario EL III Carlo Erba 1108 micro analyzer instrument. The melting point was recorded on a Chemiline CL-725 melting point apparatus and is uncorrected. Thin layer chromatography (TLC) was performed using silica gel 60 F254 (Merck) plates.

White solid, yield 86 %. m.p. 227-228 °C. IR (KBr): cm⁻¹: 3331, 3304, 3128, 3035, 2945, 2326, 2189, 1670, 1664, 1601, 1583, 1373, 1364, 1231, 1144, 1034, 876, 862, 631 cm⁻¹. ¹H NMR (400 MHz, DMSO-*d*₆) δ/ppm: 7.39 (1H, d, *J* = 8.4 Hz, aromatic H), 7.31 (1H, t, *J* = 1.6 Hz, aromatic H), 7.27 (1H, t, *J* = 8.0 & 7.6 Hz, aromatic H), 7.16 (1H, d, *J* = 7.6 Hz, aromatic H), 7.09 (2H, s, NH₂), 4.21 (1H, s, CH), 2.53 (2H, s, CH₂), 2.26 (1H, d, *J* = 16.4 Hz), 2.13 (1H, d, *J* = 16.0 Hz), 1.04 (3H, s, CH₃), 0.96 (3H, s, CH₃). ¹³C NMR (100 MHz, DMSO-*d*₆) δ/ppm: 196.16, 163.30, 158.95, 147.87, 131.05, 130.34, 129.95, 126.77, 121.97, 119.92, 112.51, 58.07, 50.33, 35.75, 32.25 (2C), 28.73, 27.19. TOF-MS: 395.0364 (M+Na)⁺. Elemental analysis: Calcd. (%) for C₁₈H₁₇BrN₂O₂: C, 57.92; H, 4.59; N, 7.51; found: C, 57.88; H, 4.56; N, 7.53.

X-Ray Structure determination

X-ray intensity data of 6665 reflections (of which 3385 unique) were collected on *X'calibur* CCD area-detector diffractometer equipped with graphite monochromated MoK α radiation (λ = 0.71073 Å). The crystal used for data collection was of dimensions 0.30 x 0.20 x 0.20 mm. The cell dimensions were determined by least-squares fit of angular settings of 1379 reflections in the θ range 3.58° to 24.51°. The intensities were measured by ω scan mode for θ ranges 3.46° to 26.00°. 1411 reflections were treated as observed ($I > 2\sigma(I)$). Data were corrected for Lorentz, polarization and absorption factors. The structure was solved by direct methods using SHELXS97.¹⁶ All non-hydrogen atoms of the molecule were located in the best E-map. Full-matrix least-squares refinement was carried out using SHELXL97.¹⁶ The final refinement cycles converged to an $R = 0.0585$ and $wR(F^2) = 0.1056$ for the observed data. Residual electron densities ranged from $-0.528 < \Delta\rho < 0.491 \text{ e}\text{\AA}^{-3}$. Atomic scattering factors were taken from International Tables for X-ray Crystallography (1992, Vol. C, Tables 4.2.6.8 and 6.1.1.4). The crystallographic data are summarized in Table 1.

Results and Discussion

An ORTEP17 view of the compound with atomic labelling is shown in Figure 2. The geometry of the molecule was calculated using the WinGX,¹⁸ PARST¹⁹ and PLATON²⁰ software. Packing view of the molecules in the unit cell viewed down the *b*-axis is shown in Figure 3.

The title compound comprises of three rings A, B and C in which ring A is pyran ring, ring B is cyclohexane ring and ring C is phenyl ring. The mean plane of phenyl ring C makes the dihedral of 88.86(14)° and 83.77(15)° with the mean planes of pyran ring A and cyclohexane ring B respectively. The pyran ring A deviates significantly from planarity and adopts boat conformation with one mirror plane passing through the atoms O1 and C4 and the other bisecting the bonds C2-C3 and C5-C6 with asymmetry parameters $\Delta C_s(O1) = 3.706$, $\Delta C_2(C2-C3) = 14.00$. Cyclohexane ring B adopts flattened sofa conformation with mirror plane passing through the atoms C3 and C8 with asymmetry parameters $\Delta C_s(C3) = 9.987$. Phenyl ring C is planar as reflected from small values of torsion angles. The

Table 1. Crystal data and other experimental details

CCDC Number	1444488
Crystal description	Block
Crystal size	0.30 x 0.20 x 0.20 mm
Empirical formula	C ₁₈ H ₁₇ BrN ₂ O ₂
Formula weight	373.25
Radiation, Wavelength	Mo K α , 0.71073 Å
Unit cell dimensions	$a = 23.557(2)$ Å $b = 9.2963(7)$ Å $c = 15.7502(12)$ Å $\alpha = 90.00^\circ$ $\beta = 93.430(8)^\circ$ $\gamma = 90.00^\circ$
Crystal system, Space group	monoclinic, C 2/c
Unit cell volume	3443.0(5) Å ³
No. of molecules per unit cell, Z	8
Absorption coefficient	2.398 mm ⁻¹
$F(000)$	1520
θ range for entire data collection	3.58 < θ < 24.51
Reflections collected / unique	6665 / 3385
Reflections observed $I > 2\sigma(I)$	1411
Range of indices	$h = -28$ to 16 $k = -11$ to 11 $l = -17$ to 19
No. of parameters refined	210
Final R-factor	0.0585
$wR(F^2)$	0.1056
Rint	0.0617
Rsigma	0.1252
Goodness-of-fit	0.934
Final residual electron density	$-0.528 < \Delta\rho < 0.491 \text{ e}\text{\AA}^{-3}$

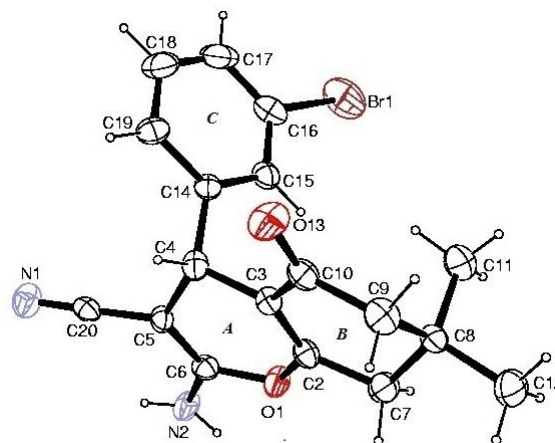
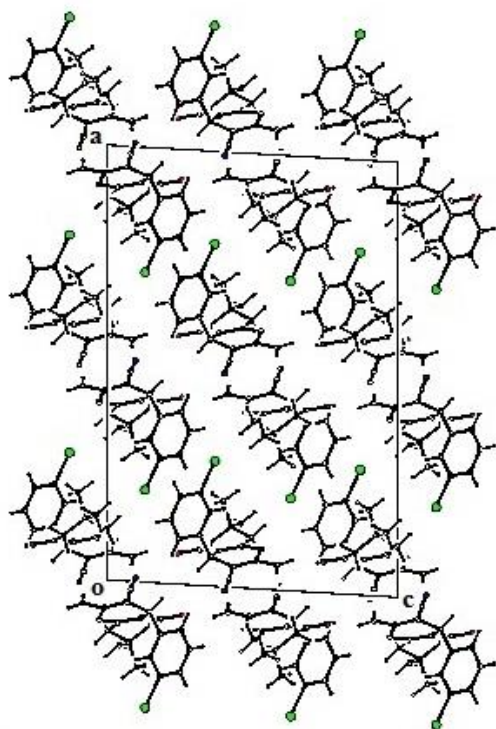
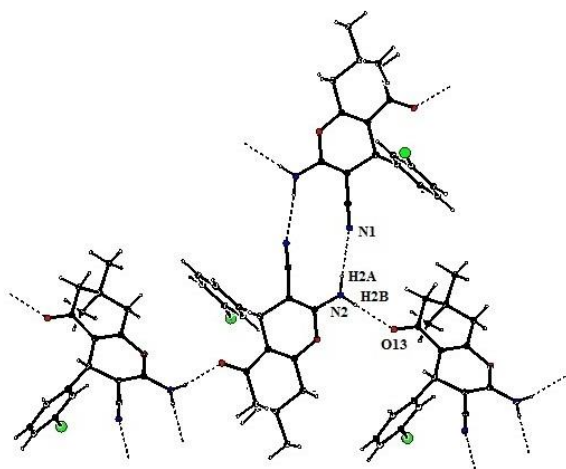


Figure 2. ORTEP view of the title molecule with displacement ellipsoids drawn at 50% probability level. H atoms are shown as small spheres of arbitrary radii.

bond distance Br1-C16 has the value 1.888(6) Å, close to literature value.²¹ The bond distances C10-O13 and N1-C20 are 1.215(5) Å and 1.137(5) Å respectively and agree well with the corresponding values in related structures.^{22,23} The bond angle N1-C5-C20 is 176.7(5)° confirms the linear character of carbonitrile group. The bond angles O13-C10-C3, O13-C10-C9 and C3-C10-C9 are 120.4(4)°, 122.9(4)° and 116.6(4)° respectively, are close to 120° and thus suggest the planar geometry about carbon atom C10.

Table 2. Selected bond lengths (Å), bond angles (°) and torsion angles(°) for non hydrogen atoms (e.s.d.'s are given in parentheses).

Bond distances(Å)		Bond angles(°)		Torsion angles(°)	
O1-C2	1.366(5)	C2-O1-C6	118.5(3)	C6-O1-C2-C7	168.7(4)
O1-C6	1.370(5)	C3-C2-O1	122.8(4)	C4-C3-C10-O13	-0.1(7)
N1-C20	1.137(5)	O13-C10-C3	120.4(4)	Br1-C16-C17-C18	179.2(4)
N2-C6	1.338(5)	O13-C10-C9	122.9(4)	C14-C15-C16-Br1	-179.9(3)
C5-C20	1.419(6)	C3-C10-C9	116.6(4)	C2-O1-C6-N2	-170.0(4)
C16-Br1	1.888(6)	N1-C20-C5	176.7(5)	C20-C5-C6-N2	1.2(8)
C10-O13	1.215(5)	N2-C6-C5	127.6(4)	C19-C14-C15-C16	1.0(7)
C8-C11	1.534(7)	N2-C6-O1	110.8(4)	O1-C2-C7-C8	161.2(4)

**Figure 3.** Packing view of molecules down to b-axis**Figure 4.** Partial view of intermolecular hydrogen interactions between the molecules.**Table 3.** Geometry of intermolecular hydrogen bonds

D-H...A	D-H (Å)	H...A (Å)	D...A (Å)	∠[D-H...A (°)]
N2-2A...N1 ⁱ	0.86	2.17	3.019(5)	168
N2-H2B-O13 ⁱⁱ	0.86	2.05	2.871(5)	159

Symmetry codes: i. -x,-y+1,-z+1, ii. x,-y, z+1/2

Selected bond lengths, bond angles and torsion angles are given in Table 2. The dihedral angle C20-C5-C6-N2 with value 1.2(8)° suggest the coplanarity of amino and carbonitrile groups. The packing view of molecules is shown in Figure 2. Analysis of the crystal packing of title compound shows the presence of intermolecular C-H...N and N-H...O hydrogen bonds in the structure (Table 3). The oxygen atom O13 of carbonyl group form hydrogen interactions with H2B attached to N2 of amino group. In addition H2A attached to N2 form intermolecular hydrogen interaction with the N1 atom of carbonitrile group. The N-H...O interactions link the molecules to form chain like structure whereas the adjacent chains are linked together by a pair of N-H...N hydrogen interactions to form dimeric structure as shown in Figure 4. In addition to these the crystal packing is also stabilized by weak Van der Waals interactions

Acknowledgments

GB is thankful to the SERB-DST, New Delhi for financial support [Grant No. EMR/2014/1220].

References

- ¹Feuer, G., *Progress in Medicinal Chemistry*; Ellis, G. P.; West, G. P., Eds.; North- Holland Publishing Company: New York, **1974**, *10*, 85.
- ²Dean, F. M., *Naturally Occurring Oxygen Ring Compounds*; Butterworths: London, **1963**, p. 176.
- ³Goel, A. and Ram, V. J., *Tetrahedron* . **2009**, *65*, 7865.
- ⁴Raj, T., Bhatia, R. K., Kapoor, A., Sharma, M., Saxena, A. K. and Ishar, M. P. S., *Eur. J. Med. Chem.* **2010**, *45*, 790.
- ⁵Flavin, M. T., Rizzo, J. D., Khilevich, A., Kucherenko, A., Sheinkin, A. K., Vilavchack, V., Lin, L., Chen, W., Mata, E., Pengsuparp, T., Pezzuto, J. M., Hughes, S. H., Flavin, T. M., Cibulski, M., Boulanger, W. A., Shone, R. L. and Xu, Z.-Q., *J. Med. Chem.* **1996**, *39*, 1303

- ⁶Morgan, L.R., Jursic, B.S., Hooper, C.L., Neumann, D.M., Thangaraj, K., Leblanc, B., *Bioorg. Med. Chem. Lett.*, **2002**, 12, 3407.
- ⁷Kumar, A., Maurva, R. A., Sharma, S. A., Ahmad, P., Singh, A. B., Bhatia, G. and Srivastava, A. K., *Bioorg Med Chem Lett* . **2009**, 19, 6447.
- ⁸Skommer, J., Wlodkowic, D., Matto, M., Eray, M. And Pelkonen, J., *Leuk. Res*, **2006**, 30, 322.
- ⁹Kasibhatla, S., Gourdeau, H., Meerovitch, K., Drewe, J., Reddy, S., Qiu, L., Zhang, H., Bergeron, F., Bouffard, D., Yang, Q., Herich, J., Lamothe, S., Cai, S. X. and Tseng, B., *Mol Cancer Ther.* **2004**, 3, 1365.
- ¹⁰Kemnitzner, W., Drewe, J., Jiang, S., Zhang, H., Zhao, J., Grundy, C. C., Xu, L., Lamothe, S., Gourdeau, H., Denis, R., Tseng, B., Kasibhatla, S. and Cai, S. X., *J. Med. Chem.*, **2007**, 50, 2858.
- ¹¹Bhavanarushi, S., Kanakaiah, V., Yakaiah, E., Saddanapu, V., Addlagatta, A. and Rani, V.J., *Med. Chem. Res.* 2013, 22, 2446.
- ¹²Paliwal, P. K., Jetti, S. R. and Jain, S., *Med. Chem. Res.*, **2013**, 22, 2984.
- ¹³Kumar, D., Reddy, V.B., Sharad, S., Dube, U. and Kapur, S., *Eur. J. Med. Chem.*, **2009**, 44, 3805.
- ¹⁴Smith, C. W., Bailey, J. M., Billingham, M. E. J., Chandrasekhar, S., Dell C. P., Harvev A. K., Hicks C. A., Kingston A. E. and Wishart G. N., *Bioorg. Med. Chem. Lett.* **1995**, 5, 2783.
- ¹⁵Brahmachari, G. and Banerjee, B., *ACS Sustainable Chem. Eng.*, **2014**, 2, 411.
- ¹⁶Sheldrick, G.M., *Acta Cryst.*, **2008**, A64, 112.
- ¹⁷Farrugia, L.J. *J Appl Cryst.*, **1997**, 30, 565.
- ¹⁸Farrugia, L.J., *J Appl Cryst.*, **1999**, 32, 837.
- ¹⁹Nardelli, M., *J Appl Cryst.*, **1995**, 28, 659.
- ²⁰Spek, A.L., *Acta Cryst.*, **2009**, D65, 148.
- ²¹Allen, F. H., Kennard, O., Watson, D.G., Brammer, L., Orpen, A.G., and Taylor, R. *J. Chem. Soc., Perkin Trans-II.*, **1987**, S1.
- ²²Kant, R., Gupta, V.K., Kapoor, K., Patil, D.R., Chandam D. R., and Deshmukh, M.B., *Acta Cryst.* **2013**, E69, o417–o418.
- ²³Kour, D., Patil, D.R., Deshmukh, M.B., Gupta, V.K. and Kant, R., *Eur. Chem. Bull.*, **2014**, 3, 224-226.

Received: 07.02.2016.

Accepted: 19.02.2016.



PHYSICAL, CHEMICAL AND CATALYTIC PROPERTIES OF β -SUBSTITUTED DERIVATIVES OF TETRAPHENYLPORPHYRIN

Svetlana Pukhovskaya,^{[a]*} Yuliya Ivanova,^[b] Dao The Nam,^[a] Ilya Kuzmin,^[a] Mikhail Razumov,^[a] Natalya Litova^[a] and Artur Vashurin^[a]

Keywords: porphyrins, structure, acid-base properties, metallocomplexes, catalytic activity

Acidic and basic properties of β -substituted derivatives of tetraphenylporphyrin are studied. First and second stage ionization constants for ligands investigated are reported. Acidic properties of porphyrins are in good agreement with classical theories about influence of substituent's nature and geometrical structure of macrocycle on their physical and chemical parameters. It is found that porphyrins have catalytic activity in heterogeneous oxidation of *N,N*-diethylcarbamodithioate.

*Corresponding Authors

E-Mail: Svetlana.puhovskaya@mail.ru

[a] Ivanovo State University of Chemistry and Technology, 153000, Russia, Ivanovo, Sheremetevsky ave. 7

[b] G. A. Krestov Institute of Solution Chemistry of Russian academy of Sciences, Russia, Ivanovo, 153045, Akademicheskaya str. 1

Introduction

Mercaptans and mercaptides present in light oil and associated gas lead to wear of equipment, oil pipelines and damage the environment. The removal of such compounds is crucial for the technology and environment safety. High yield of oxidation product of mercaptans, which have high toxicity and corrosive activity, may be reached while using the tetrapyrrole macroheterocyclic compounds (metal porphyrins and metal phthalocyanines) as catalysts for deodorant oil refinery. Currently, oxidation of C_1 - C_4 thiols to disulfides is carried out by air oxygen in presence of alkali with homogeneous and heterogeneous phthalocyanine catalyst. Investigation of central metal ion's influence showed,¹⁻³ that cobalt complex with disulfonic acid of phthalocyanine (Pc) has the highest catalytic properties. It is found that catalytic activity decreases in the series: $CoPc > CuPc > FePc > NiPc > (Cl)SbPc > AlPc > (Cl)AlPc > ZnPc > (Cl)CrPc$.⁴

A number of studies showed that the structure of macrocyclic ligand is also important for catalysis along with the nature of metal cation. Thus, catalytic activity of metallophthalocyanines changes significantly and unambiguously on introducing strong electron-withdrawing substituents into macromolecule. Metal complexes of porphyrins are interesting in this case. Introduction of the substituent in the periphery of porphyrin macrocycle leads to increasing influence of the electronic and structural effects on the coordination unit. Besides, the nature of peripheral substituent affects the way in which the heterogeneous catalysts are obtained. However, there is little information about porphyrins in this field with regard to phthalocyanines.^{5,6} Therefore, the influence of nature of substituents in porphyrin macrocycle on physical and

chemical properties of the ligand and on catalytic activity of porphyrin cobalt complexes (**PI** – **PIII**) (Figure 1) are investigated.

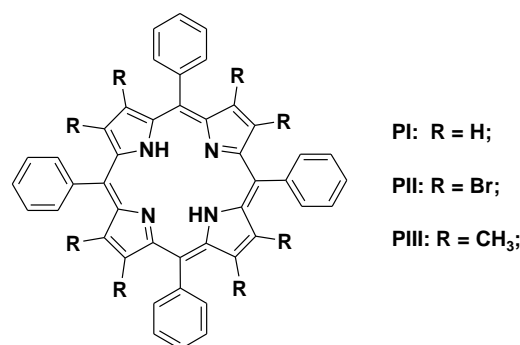


Figure 1. Structure of porphyrins

Experimental

5,10,15,20-Tetraphenylporphyrin (**PI**) was synthesized according to the method described in the literature.⁷ UV-vis (chloroform), $\lambda(\lg \epsilon)$: 413(5.60), 513(4.26), 546(3.90), 590(3.70), 650(3.73); ¹H NMR (500 MHz, CDCl₃, TMS): 8.30 (m, 8 H, phenyl *o*-H), 7.80 (m, 12 H, phenyl *m*- and *p*-H), 8.75 (8H, β -C), -3.75 (s, 2H, NH). Anal. Calcd for C₄₄H₃₀N₄: C, 87.12; H, 4.95; N, 7.92. Found: C, 87.15; H, 4.91; N, 7.91. Purification was carried out chromatographically on Al₂O₃ (III degrees of Brockmann activity).

The free-base 2,3,7,8,12,13,17,18-octabromo-5,10,15,20-tetraphenylporphyrin (**PII**) is prepared by bromination reaction of *meso*-tetraphenylporphyrinato copper(II) followed by an acidic demetalation reaction^{8,9} 2,3,7,8,12,13,17,18-octabromo-5,10,15,20-tetraphenylporphyrin is purified chromatographically on Al₂O₃ (II and III degrees of Brockmann activity). Eluent composition: chloroform – benzene. Electron absorption spectra were similar to described in literature.

UV-vis (toluene), $\lambda(\lg\epsilon)$: 470 (5.25); 622 (4.10); 738 (3.85). $^1\text{H NMR}$ (500 MHz, CDCl_3 , TMS), 8.21 (m, 8 H, phenyl *o*-H), 7.79 (m, 12 H, phenyl *m*- and *p*-H), -1.65 (bs, 2H, NH). Elemental analysis is consistent with porphyrins without solvent of crystallization. Anal. Calcd for $\text{C}_{44}\text{H}_{22}\text{N}_4\text{Br}_8$: C, 42.42; H, 1.78; N, 4.49; Br, 51.30. Found: C, 42.35; H, 1.90; N, 4.40; Br, 51.32.

The free-base 2,3,7,8,12,13,17,18-octamethyl-5,10,15,20-tetraphenyl-porphyrin (**PIII**) is prepared by the literature method.¹⁰ UV-Vis (chloroform), $\lambda(\lg \epsilon)$: 454 (5.27), 555(4.05), 602(3.98), 695(3.67). $^1\text{H NMR}$ (500 MHz, CDCl_3 , TMS), 8.35 (m, 8 H, phenyl *o*-H), 7.93 (m, 12 H, phenyl *m*- and *p*-H), 1.84 (s, 24H, Me), -1.14 (s, 2H, NH). Elemental analysis was consistent with porphyrins without solvent of crystallization. Anal. Calcd for $\text{C}_{52}\text{H}_{46}\text{N}_4$: C, 86.90; H, 6.40; N, 6.70;. Found: C, 86.91; H, 6.38; N, 6.68.

The purity of the compound was controlled by TLC method on aluminum plates with stacked silica gel F₂₅₄ layer of 0.5 mm thickness ("Merck").

The synthesis of Co(II) porphyrins is carried out according to known method.¹¹: 10 mg of porphyrin is dissolved in 50 ml of chloroform to which is added 10 times excess of cobalt acetate. Reaction mixture is heated and boiled for 40-50 minutes. Reaction is controlled by monitoring the change in electron absorption spectrum of the mixture. Degeneration of absorption bands of porphyrin and appearance of absorption bands of its metal complex indicates the completeness of the reaction. After reaction is finished the reaction mixture is cooled and the excess of the salt is removed by water extraction. The cobalt complex is chromatographed on aluminum oxide of III degree of Brockmann activity using chloroform as eluent. The crystalline complex is isolated by precipitation from chloroform.

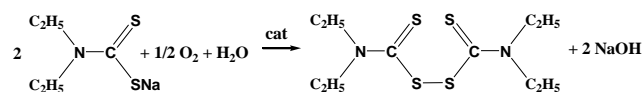
The dipolar aprotic solvent acetonitrile of high purity (water content is less than 0.03 %) is used as solvent for titration. Initial compounds are in molecular form in this solvent. 1,8-diazabicyclo[5.4.0]undec-7-ene (DBU) is used as deprotonating agent, in acetonitrile DBU has ionization constant of conjugated acid $\text{p}K_a = 13.2$.¹² The reagent is used without additional purification.

Spectrophotometric titration of porphyrin solutions in acetonitrile by DBU solution is carried out on Shimadzu UV-1800 spectrophotometer in a manner described in the literature.^{13,14} Error in the determination of the acid ionization constants is not more than 3 %.

Spectra $^1\text{H NMR}$ are recorded on spectrometer «Bruker-500» with an operating frequency of 500 MHz in CDCl_3 (internal standard – TMS).

The study of the kinetics of oxidation of sodium N,N-diethylcarbamodithioate (Fig.2) is carried out in specially constructed cell with volume of 650 ml in which 0.3 M solution of N,N-diethylcarbamodithioate (DTC) was loaded with 0.01 g of catalyst. The temperature is maintained 25 °C within ± 0.05 °C. The air is fed via microcompressor with constant rate of 2 L min^{-1} . After establishing a constant temperature the solution was mixed and sample of 2 mL was taken to determine initial concentration of DTC, then

compressor was turned on. This moment was taken as the beginning of the reaction. Samples of 2 mL were taken periodically during the experiment to determine current concentration of DTC.



Scheme 1. The reaction of DTC oxidation

The DTC concentration is determined by mixing 4 ml of 0.08 M solution of CuSO_4 to 2 mL of the sample solution. A dark-brown precipitate of copper complex is formed. Then 0.005 mL of 50% acetic acid is added and copper complex with DTC is extracted into the chloroform layer. Optical density of solution is determined spectrally at a wavelength of 436 nm. Current concentration of DTC is calculated with help of calibration line.¹⁵

Under condition of constant oxygen and catalyst concentration and pH of solution the rate of oxidation of DTC is described by first order kinetic equation:

$$\frac{\partial c}{\partial \tau} = -k_{\text{obs}} \cdot c \quad (1)$$

where c is the DTC concentration (M);
 τ is the time (s),
 k_{obs} is the the observed rate constant (s^{-1})

The first order dependence is confirmed by the linear dependence of $\ln c$ against (τ) and the constancy of the rate constants calculated from the equation.

$$k_{\text{obs}} = \frac{\ln \frac{c_0}{c}}{\tau} \quad (2)$$

where c^0 is the initial DTC concentration,
 c is the concentration at time (τ).

It was found in preliminary experiments that non-catalytic oxidation of DTC is very slow ($k_{\text{obs}} = 1.7 \times 10^{-5} \text{ s}^{-1}$).¹⁵

Activation energies are calculated by using the Arrhenius equation

$$E^\ddagger = 19.1 \left(\frac{T_1 T_2}{T_2 - T_1} \right) \lg \left(\frac{k_2}{k_1} \right) \quad (3)$$

The conversion was calculated from the equation:

$$\chi = \frac{C^0 - C^\tau}{C^0} \quad (4)$$

where C^0 – initial concentration of DTC,
 C^τ – DTC concentration at the current time.

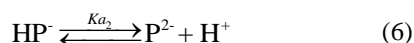
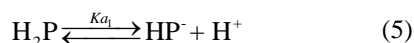
Results and Discussion

A review of literature¹⁶⁻¹⁹ showed that introduction of sterically demanding substituents at the periphery leads to a significantly nonplanar macrocycle conformation. Physical and chemical studies²⁰⁻²³ of the whole series of sterically-disturbed porphyrins brought a direct correlation between the nonplanarity degree of the porphyrin macrocycle and the properties of these compounds.

As shown in our previous work,^{24,25} the disturbing of the porphyrin macrocycle planarity leads to decreasing of aromaticity of the molecule and a certain isolation of pyrrole and pyrrolinone fragments. At the same time both basic and acidic properties are enhanced. It suggests that porphyrins with disturbed macrocycle structure will be easily deprotonating in presence of strong bases and hence metal complexation reactions will have higher rates.

Acid properties of porphyrins (PI - PIII) are studied by spectrophotometric titration method in the system of acetonitrile - 1,8-diazabicyclo[5.4.0]undec-7-ene (5) under 298.15 K. Anionic form of tetraphenylporphyrin (PI) was not obtained in this system obviously because of its low acid properties in regards to sterically disturbed derivatives PII – PIII.

Deprotonation of interior nitrogen atoms of tetrapyrrolic macrocycle proceeds in two steps according to the equations.²⁶



where H_2P ; HP^- and P^{2-} are respectively neutral and deprotonated forms of porphyrin.

Two families of spectral curves are obtained in absorption spectra of compounds II and III during titration. The isosbestic points are obtained and are shown on (Figure 3).

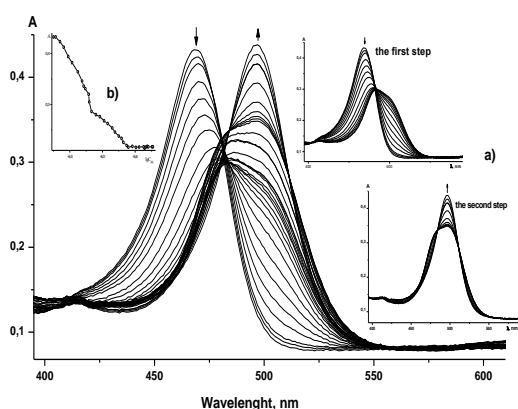


Figure 3. a) Changing in UV-Vis spectra of PII ($c_{\text{PII}} 2.11 \times 10^{-6}$ M) in the system AN – DBU ($0 \div 4.13 \times 10^{-6}$ M) under 298.15 K, b) Titration curve in the system AN – DBU ($0 - 3 \times 10^{-5}$ M) 298.15 K (λ 449 nm).

The electron absorption spectrum of molecular form (H_2PII ; λ_{max} , nm ($\lg \epsilon$) 470 (5.25), 568 (3.95), 622 (4.10), 738(3.85)) gradually transforms into spectrum of final dianionic form (PII^{2-} ; λ_{max} , nm ($\lg \epsilon$) 497 (5.30), 774 (4.80)) with increasing of titrant concentration (c_{DBU}). For compound III respectively: H_2PIII 463 (5.15), 548 (3.88), 636 (4.17), 690 (3.63) was transformed into PIII^{2-} 439 (4.93), 642 (4.23)

Determination of inflection point coordinate (and corresponding c_{DBU}) on titration curve allows to allocate two regions in absorption spectrum. These regions are likely with regard to the first and second steps of deprotonation, i.e. the formation of mono, and dianionic forms (HP^- , P^{2-}) of compounds (PII - PIII). (Figure 4,5) Calculation of current concentrations of deprotonated and molecular forms based on the material balance of the equation showed that the compound PII is almost twice deprotonated under the condition of DBU concentration of $3.5 - 4.13 \times 10^{-6}$ M.

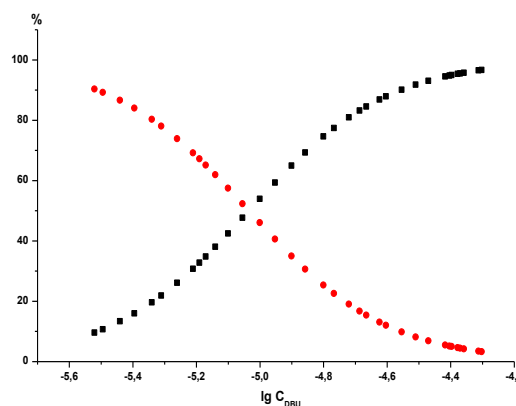


Figure 4. Fractions in % of the doubly deprotonated and the molecular forms in the course of titration for PII

For PIII: it transforms to final twice deprotonated form (Figs: 4-5) under the $c_{\text{DBU}} 3.68 \times 10^{-6} - 3 \times 10^{-5}$ M.

$$c_0 = c_{\text{H}_2\text{PII}} + c_{\text{PII}^{2-}} \quad (7)$$

The stage deprotonation constants for compounds PII and PIII were calculated according to equations (4) and (5). The values were respectively $\lg K_1 -6.35$; $\lg K_2 -5.80$ и $\lg K_1 -4.80$; $\lg K_2 -3.95$.

$$\lg K_1 = \lg \left(\frac{[\text{HP}^-]}{[\text{H}_2\text{P}]} \right) + \lg c_{\text{DBU}} \quad (8)$$

$$\lg K_2 = \lg \left(\frac{[\text{P}^{2-}]}{[\text{HP}^-]} \right) + \lg c_{\text{DBU}} \quad (9)$$

Here are K_1 and K_2 are the constants of acidity of the compound for the first and the second stage, $\lg(\text{HP}^-/\text{H}_2\text{P})$ $\lg(\text{P}^{2-}/\text{HP}^-)$ indicate the ratio for the first and for the second stages of the compounds PII and PIII, $\lg c_{\text{DBU}}$ is the analytical value of DBU titrant concentration.

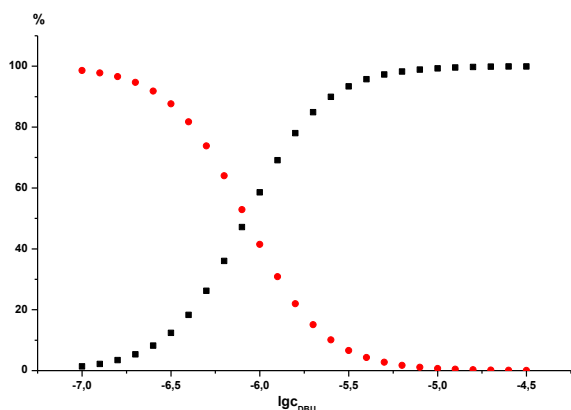


Figure 5. Fractions in % of the doubly deprotonated and the molecular forms in the course of titration for PIII

Comparison of values of deprotonation constants showed that in the system acetonitrile DBU 2,3,7,8,12,13,17,18-octabromo-5,10,15,20-tetraphenylporphyrin is easily deprotonated and has stronger acid properties than 2,3,7,8,12,13,17,18-octamethyl-5,10,15,20-tetraphenylporphyrin. Deprotonation of the macrocycle for the first and the second stage differ approximately by two orders.

The (Figure 6) presents kinetic curves of DTC oxidation in presence of cobalt complexes with investigating macrocycles.

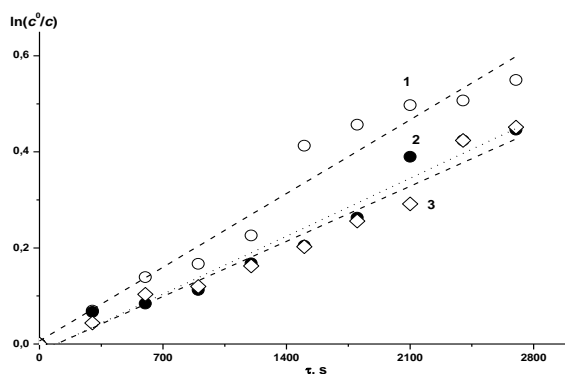
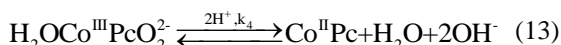
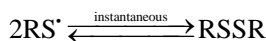
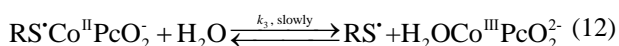


Figure 6. Kinetic curves of DTC oxidation in presence of cobalt complexes with 1) PII, 2) PI, 3) PIII, under 298.15 K, $C_{DTC} 3 \times 10^{-3}$ M.

Kinetic data of DTC oxidation and analysis of known results²⁷⁻³⁰ suggest a similar mechanism for homogeneous and heterogeneous conditions. It is known that RS^- anion is one stage (equations 10 - 13) in presence of cobalt complexes with tetrapyrrole macroheterocycles like phthalocyanine.



Supposing that the mechanism in equations (10)-(13) is realized in presence of co-porphyrins then introduction of electron-withdrawing substituents would lead to decreasing electron density in coordination center and eases the coordination of the substrate and the formation of triple complex with oxygen $RS^* \cdot Co^{II}Pc \cdot O_2^-$.

Table 1. Effective constants of DTC oxidation rate under 298.15 K and activation energies of the process.

Macrocycle	$k_{obs} \times 10^2, (s \times g)^{-1}$	$E^\ddagger, kJ mol^{-1}$	χ
CoPI	23.6 ± 0.2	2.37 ± 0.02	64.5
CoPII	59.1 ± 0.3	0.09 ± 0.01	73.6
CoPIII	13.7 ± 0.1	12.93 ± 0.05	67.3

Calculated values of activation energies (Table 1) for this process in presence of investigated porphyrins suggest that there is no diffusion inhibition for the reaction. It supposes that there are two factors affecting the rate of the process: the rate of oxygen supply and its diffusion and the stability of the triple complex which determines the electron effects of peripheral substituents affecting the coordination unit. Under condition of constant rate of oxygen supply the first factor is leveled. It allows determining the influence of macrocyclic molecule periphery on catalytic activity.

Obtained experimental data are in good agreement with classical theories about the influence of substituent's nature, geometrical structure of macrocycle on acid properties of porphyrins. It also shows good similarity with catalytic activity of the porphyrin's cobalt complexes in dithiocarbamic acids oxidation.

Acknowledgments

This work is supported by the Ministry of Education and Science of the Russian Federation, and partially supported financially by grant of the President of the Russian Federation (project No MK-2776.2015.3) and Russian Foundation of Basic Research.

References

- Bricker, J. C., Laricchia, L., *Topics Catal.* **2012**, 55, 1315.
- Joseph, J. K., Jain, S. L., Sain, B., *Ind. Eng. Chem. Res.* **2010**, 49, 6674.
- Das, G., Sain, B., Kumar, S., *Catal. Today* **2012**, 198, 228.
- Zagal, J. H., Griveau, S., Silva, J. F., Nyokong, T., Bedioui, F., *Coord. Chem. Rev.* **2010**, 254, 2755.
- Vashurin, A. S., Pukhovskaya, S. G., Semeikin, A. S., Golubchikov, O. A., *Macroheterocycles* **2012**, 5, 72.
- Marfin, Y.S., Vashurin, A.S., Pukhovskaya, S. G., Rummyantsev, E.V., *J. Sol-Gel Sci. Technol.* **2013**, 66, 306.
- Semeikin, A. S., Koifman, O. I., Berezin, B. D., *Chem. Heterocycl. Compd.* **1986**, 22, 629.
- Bhyrappa, P., Krishnan, V., *Inorg. Chem.* **1991**, 30, 239.
- Bhyrappa, P., Nethaji, M., Krishnan, V., *Chem. Lett.* **1993**, 869.

- ¹⁰Kuzmin, N. G., Koifman, O. I., *Russ. J. Appl. Chem.* **1988**, *61*, 1426.
- ¹¹Buchler, J. W., *Porphyrins and metalloporphyrins*, Ed. Smith K. M. Amsterdam : Elsevier, **1975**.
- ¹²Kaljurand, A., Kütt, L., Sooväli, T., Rodima, V., Mäemets, I., Leito, I., Koppel, A., *J. Org. Chem.* **2005**, *70*, 1019.
- ¹³Ivanova, Yu. B., Sheinin, V. B., Mamardashvili, N. Zh. *Russ. J. Gen. Chem.* **2007**, *77*, 1458.
- ¹⁴Ivanova, Yu. B., Churakhina, Yu. I., Mamardashvili, N. Zh., *Russ. J. Gen. Chem.* **2008**, *78*, 673.
- ¹⁵Vashurin, A. S., Badaukaite, R. A., Futerman, N. A., Puhovskaya, S. G., Shaposhnikov, G. P., Golubchikov, O. A., *Petr. Chem.* **2013**, *53*, 197.
- ¹⁶Senge, M. O., Kalisch, W. W., *Inorg. Chem.* **1997**, *36*, 6103.
- ¹⁷Senge, M. O., *In: The Porphyrin Handbook*, Eds. K. M. Kadish, K. M. Smith, R. Guilard. San Diego: Academic Press. **2000**.
- ¹⁸Golubchikov, O. A., Pukhovskaya, S. G., Kuvshinova, E. M. *Russ. Chem. Rev.* **2005**, *74*, 249.
- ¹⁹D'Souza, F., Zandler, M. E., Tagliatesta, P., Ou, Z., Shao, J., Van Caemelbecke, E., Kadish, K. M., *Inorg. Chem.* **1998**, *37*, 4567.
- ²⁰Comba, P., *Coord. Chem. Rev.* **1993**, *123*, 1.
- ²¹Pukhovskaya, S. G., Ivanova, Yu. B., Dao The Nam, Vashurin, A. S., *Russ. J. Phys. Chem. A* **2014**, *88*, 1670.
- ²²Ivanova, Yu. B., Chizhova, N. V., Pukhovskaya, S. G., Mamardashvili, N. Zh., *Russ. J. Gen. Chem.* **2014**, *84*, 939.
- ²³Fonda, H. N., Gilbert, J. V., Cormier, R. A., Sprague, J. R., Kamioka, K., Connolly, J. S., *J. Phys. Chem.* **1993**, *97*, 7024.
- ²⁴Pukhovskaya, S., Ivanova, Yu., Dao The Nam, Vashurin, A., Golubchikov, O., *J. Porphyrins Phthalocyanines* **2015**, *19*, 858.
- ²⁵Dao The Nam, Ivanova, Yu. B., Puhovskaya, S. G., Kruk, M. M., Syrbu, S. A., *RSC Adv.* **2015**, *5*, 26125.
- ²⁶Berezin, B. D., *Coordination compounds of porphyrins and phthalocyanines*, Wiley, New York, Toronto, **1981**.
- ²⁷Vashurin, A., Maizlish, V., Pukhovskaya, S., Voronina, A., Kuzmin, I., Futerman, N., Golubchikov, O., Koifman, O., *J. Porphyrins Phthalocyanines* **2015**, *19*, 573.
- ²⁸Borisenkova, S. A., *Russ. Petrol. Chem.* **1991**, *31*, 391.
- ²⁹Tyapochkin, E. M., Kozliak, E. I., *J. Mol. Catal. A: Chem.* **2005**, *242*, 1.
- ³⁰Tyapochkin, E. M., Kozliak, E. I., *J. Mol. Catal. A: Chem.* **2003**, *203*, 37.

Received: 26.11.2015.

Accepted: 21.02.2016.



REMOVAL OF Pb(II) FROM WASTEWATERS BY ACTIVATED CARBON FROM LEBANESE *CYMOPOGON CITRATUS* (LEMONGRASS): A COMPARATIVE STUDY

Hala Haidar^[a], Akram Hijazi^{[a,b]*}, Dania Houssein^[a], Wassef El Khatib^[a], Hassan Rammal^[a], Ali Mcheik^[a], Ziad Damaj^[a] and Abd-Al-Ameer Al Rekaby^[c]

Keywords: Activated carbon, adsorption, isotherm, kinetic, thermodynamic.

This study is made to prove the efficiency of the activated carbon (AC) of Lebanese *Cymbopogon citratus* in the adsorption of lead (Pb(II)) from aqueous medium. The adsorption was found to be dependent on initial metal ion concentration, pH of the solution, temperature, contact time and adsorbent dose. The maximum adsorption capacity was found for the concentration of 450 mg L⁻¹, pH 4, temperature 25 °C, contact time 2 h, and adsorbent dose 1g. The equilibrium adsorption was better described by Freundlich isotherm model rather than Langmuir model. The kinetic data were better represented by the pseudo-second-order than the pseudo-first-order kinetic model. Thermodynamic studies showed that the process was exothermic and spontaneous. The results of this study reveal that the activated carbon (AC) of Lebanese *Cymbopogon citratus* is a very effective and environmentally friendly adsorbent, with low cost for Pb(II) removal.

*Corresponding Authors

E-Mail: hijazi_akram@hotmail.com

- [a] Doctoral School of Science and Technology, Research Platform for Environmental Science (PRASE), Lebanese University, Lebanon.
 [b] Laboratory of Inorganic chemistry and Organometallic, Lebanese University, Lebanon.
 [c] Al-Mustansiriya University, College of Science, Department of Biology, Iraq.

Introduction

The problem of pollution have attracted increasing interest with the growth and development of the industrial sector, since it affects several vital sectors.¹ Heavy metals are among the factors that contribute to the pollution, their toxicity and the danger of their bioaccumulation in the food chain represent one of the major environmental and health problems of our modern society.² The term heavy metal refers to elements that have a relatively high density greater than 5.0 g cm⁻³ and exhibit metallic properties, it includes transition metals and metalloids arsenic and antimony.³

Lead is one of the most toxic heavy metals, it has several fields of application, including battery storage, production of insecticides and plastic water pipes.⁴ Lead is emitted into the atmosphere after the combustion of fossil fuels and the smelting of sulfide ores, it is also emitted in lakes and streams by acid mine drainage.⁵ According to the guidelines of World Health Organization (WHO) and American Water Works Association (AWWA), the quantity recommended for lead in drinking water is 0.05 mg L⁻¹.⁶ The U.S. Environmental Protection Agency has set the maximum dose of lead allowable in drinking water to be 15 ppb.⁷

Several techniques have been used for the decontamination of heavy metals.⁸ Adsorption has been recently recognized as an effective and economic method for heavy metal wastewater treatment. The adsorption

process offers flexibility in design and operation and in many cases will produce high-quality treated effluent. In addition, because adsorption is sometimes reversible, adsorbents can be regenerated by suitable desorption process.⁹ Many studies have been conducted to find low-cost adsorbents as replacement for costly current methods, an adsorbent is considered as low-cost if it is naturally abundant, requires little processing or is a by-product of waste material from industry according to Bailey et al.¹⁰ Many types of low-cost adsorbents have been used such as clay adsorbents,¹¹ marine sponges,¹² algae,¹³ activated carbon,¹⁴ biomass of plants^{15,16} and activated carbon.⁹

More recently, many studies have been made about the conversion of solid waste into porous materials,¹⁷⁻¹⁹ especially activated carbon.²⁰ The efficiency of the bio-sorption of Pb(II) by Lebanese *Cymbopogon citratus* is demonstrated by Hijazi et al.¹⁶

In this work, we have studied the benefits of natural by-products of Lebanese *Cymbopogon citratus*, and the effectiveness of use of activated carbon (AC) resulted from these plants as adsorbent. The effect of different parameters on the adsorption process such as initial concentration of the pollutant, pH, temperature, contact time and dose of the adsorbent has been investigated. Isotherms, kinetic and thermodynamic studies have also been performed.

Experimental

Adsorbent preparation

Crude Lebanese *C. citratus* plant was washed several times with deionized water and dried for one week at room temperature and then left in an oven at 60 °C for 2 days. Then, they were ground and sieved at 0.25 mm. After milling, pyrolysis of the raw material was realized in a

temperature-programmed oven (WiseTherm Furnace) at 600 °C. After pyrolysis, the char was cleaned from the ash and dried in the oven for 2 hours at 90 °C.

For every 10 g of charcoal, 100 ml of H₂O₂ (15 %) were added. They were stirred for 24 h before washing until neutralization of the rinsing water by regular check of pH. Finally, they are kept in the oven at 95 °C for 24 h to obtain a dry AC.

Batch adsorption studies

1000 mg L⁻¹ stock solution of Pb(II) (1000 mg L⁻¹) was prepared by dissolving Pb(NO₃)₂ (supplied by Aldrich, in analytical grade and without further purification) in deionized water. Other solutions with different concentrations were then prepared by mixing a determined volume of the stock solution with deionized water.

Batch experiments were carried out using Erlenmeyer flasks (50 ml) where 50 ml of solution of Pb(II) were mixed with 0.5 g of AC of *C. citratus* at room temperature (25 °C ± 2 °C) except studies concerning the effect of temperature.

To study the effect of pH, small amounts of nitric acid (0.1 mol) or sodium hydroxide (0.1 mol) solutions were added to the mixtures until the target pH was reached. All the experiments were conducted without adjusting the solution pH, except when the effect of pH on Pb(II) removal was studied. In this particular study, the solution pH was adjusted to the desired value throughout the experiment. Solutions are then stirred under a speed of 350 rpm for one hour, whereas, for studies of the effect of the contact time, stirring time was different.

Different batch operational conditions were examined including AC of *C. citratus* dose (0.2–2 g), initial Pb(II) concentration (25–600 mg L⁻¹), temperature (0–75 °C), contact time (5–180 min) and pH (2–12).

At the end of an experiment, the adsorbent was filtered out with filter-paper by Buchner filtration followed by a second filtration using a 0.45 μm syringe micro-filters. The filtrate was collected and analysed by atomic adsorption spectrometer (AAS) at 217 nm, for the determination of Pb(II) content.

The percentage removal efficiency *R* (%) was determined using Eqn.1.

$$R = 100 \frac{C_0 - C_e}{C_0} \quad (1)$$

where

*C*₀ is the initial concentration of Pb(II),
*C*_e is the equilibrium concentration of Pb(II).

The equilibrium adsorption capacity *q*_e (mg g⁻¹), and the adsorption capacity at time *t*, *q*_t (mg g⁻¹), were evaluated according to the Eqns. 2 and 3.

$$q_e = \frac{(C_0 - C_e)V}{m} \quad (2)$$

$$q_t = \frac{(C_0 - C_t)V}{m} \quad (3)$$

where

*C*_t is the concentration of Pb(II) at time *t*,
V is the volume of Pb(II) solution and *m* is the weight of adsorbent.

Adsorption isotherms

Adsorption isotherms are an essential way for the understanding of the mechanism of an adsorption system, since they represent the amount of compounds adsorbed on a surface as a function of concentration at a constant temperature.²¹

Langmuir isotherm is based on the assumption that predicts monolayer coverage of the adsorbate on the outer surface of the adsorbent. This model also suggests that there is no lateral interaction between the adsorbed molecules.²² Linear form of Langmuir isotherm is presented by Eqn. 4.

$$\frac{C_e}{q_e} = \frac{1}{q_{\max} K_L} + \frac{C_e}{q_{\max}} \quad (4)$$

where

*C*_e is the equilibrium pollutant concentration,
*q*_e is the amount of pollutant adsorbed onto adsorbent at equilibrium,
*q*_{max} is the maximum monolayer capacity of the adsorbent and
*K*_L is Langmuir isotherm constant.

The essential characteristics of the Langmuir isotherm parameters can be used to predict the affinity between the sorbate and sorbent using separation factor or dimensionless equilibrium parameter,²¹ “*R*_L” is expressed as follows.

$$R_L = \frac{1}{1 + K_L C_0} \quad (5)$$

Four cases are possible. If *R*_L = 0, the adsorption is irreversible, if 0 < *R*_L < 1, the adsorption is favorable, if *R*_L = 1, the adsorption is linear and if *R*_L > 1, the adsorption is unfavourable.

Freundlich isotherm

Freundlich isotherm model is the well-known earliest relationship which describes the adsorption process. It can be applied to non-ideal sorption on heterogeneous surfaces as well as multilayer sorption.²¹ This model assumes an exponential decrease in the adsorption energy with the increase in surface coverage. Adsorption is considered to

occur with negligible interaction between sorbed molecules.²³ linear form of Freundlich isotherm is expressed as Eqn. 6.

$$\log q_e = \log K_F + \frac{1}{n \log C} \quad (6)$$

where

K_F is the Freundlich constant indicating adsorption capacity,

n is the adsorption intensity and

n value indicates the degree of non-linearity between solution concentration and adsorption as follows, three cases are possible.

If $n = 1$ the adsorption is linear, if $n < 1$ the adsorption is a chemical process and if $n > 1$ the adsorption is a physical process.

Kinetic study

In order to evaluate the rate and mechanism of Pb(II) adsorption, the experimental kinetic data were examined with two reaction rate models i.e., pseudo-first-order kinetics and pseudo-second-order kinetics.

The pseudo-first-order kinetic model is based on the assumption that the sorption rate is proportional to the number of free available sites. It is usually used to determine the kinetic behaviour at the initial stage of the adsorption process.²⁴ The pseudo-first-order rate equation of Lagergren is presented as Eqn. 7.

$$\log(q_e - q_t) = \log q_e - \frac{k_1}{2.303} t \quad (7)$$

where k_1 is the pseudo-first-order rate constant.

The pseudo-second-order kinetic model covers the entire range of the adsorption process.²⁵ The pseudo-second-order rate equation given as Eqn. 8.

$$\frac{t}{q_t} = \frac{1}{k_2 q_e^2} + \frac{1}{q_e} t \quad (8)$$

where k_2 is the pseudo-second-order rate constant. The two kinetic models were tested for a time up to 180 min.

Thermodynamic Study

The thermodynamic parameters, of the adsorption of Pb(II) onto the AC of *C. Citrates*, such as the enthalpy of adsorption ΔH^0 , Gibbs free energy ΔG^0 , and entropy ΔS^0 , were determined following the equations:

$$\Delta G^0 = -RT \ln K_c \quad (9)$$

$$\Delta G^0 = \Delta H - T\Delta S \quad (10)$$

where

T is the temperature in Kelvin,

R is the gas constant ($8.314 \times 10^{-3} \text{ kJ mol}^{-1} \text{ K}^{-1}$) and

K_c is the distribution coefficient determined as²⁶: $K_c = q_e/C_e$, ΔH^0 and ΔS^0 were determined respectively from the intercept and gradient from the plot of ΔG^0 versus T .

Results and Discussion

Effect of initial concentration of Pb(II)

The removal percentage and adsorption capacity of Pb(II) were evaluated at different initial metal concentrations (Figure 1), between 25 and 600 mg L⁻¹. At low concentrations, the adsorption of the metal ion on the adsorbent increases rapidly with increasing concentration of the metal and is slowed when the metal concentration reached 300 mg L⁻¹ for an adsorption capacity of 29.98 mg g⁻¹. The rapid increase in the adsorption capacity can be attributed to the interaction between the metal ions and the active sites of the adsorbent as well as to an increase in the driving force for the mass transfer between the aqueous phases and the solid phase.²⁷ Beyond this value, the adsorption capacity increases slowly with the increase of the metal concentration, this is due to the filling of the majority of sorption sites of surface at higher initial concentrations.

There is no large difference between the removal percentages for different concentrations, it is between 99.46 and 99.95 %, with the highest removal being 99.95 % for a concentration of 450 mg L⁻¹. This indicates that the AC can eliminate efficiently a large amount of metal.

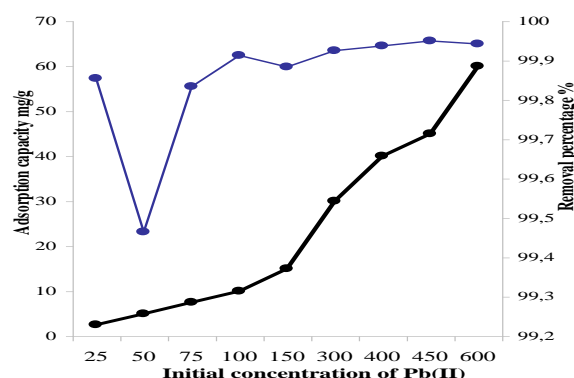


Figure 1. Effect of initial Pb(II) concentration on adsorption capacity (black) and extent of its removal (blue).

Effect of pH

pH is an important parameter affecting the adsorption process and surface properties as well as degree of ionization and speciation of the metal ions in aqueous solution²⁶ Hence, we have studied the effect of pH on the

removal percentage of Pb(II) by the AC of *C. citratus*, in the pH range of 2-12. Figure 2 shows that the removal percentage increases with the pH of medium until pH 6 corresponding to the optimal pH for adsorption of Pb(II), with a removal of 99.97 %.

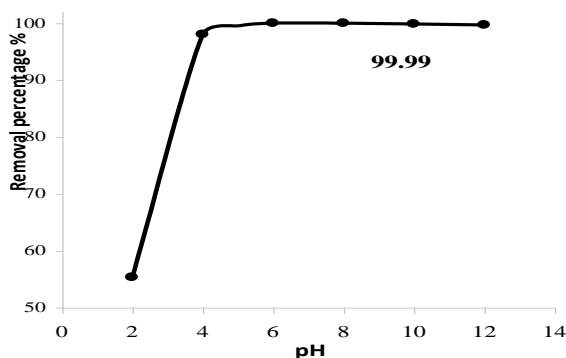


Figure 2. Effect of pH on the removal of Pb(II).

This is explained by the fact that at $\text{pH} < 4$, the active sites on the surface of AC are protonated, thus no interaction occurs with metal ions. At pH between 4 and 6, H^+ ions are released from the active sites and the adsorbed amount of the metal cation is usually found to increase. At higher pH values ($\text{pH} > 6$), the formation of hydroxyl Pb(II) species may cause a decrease of the concentration of free Pb(II), thereby decreasing the removal of Pb(II) by adsorption.²⁸

This is demonstrated by the percentage removal of 99.99 % at pH 8 greater than 99.97 % at pH 6, which is due to the removal of metal by precipitation in addition to adsorption.

Effect of temperature

Temperature is likely to affect on the adsorption process. We have studied the effect of temperature on the percentage removal of Pb(II) in a range between 0 and 75 °C (Figure 3). The effect of temperature is not striking. When the temperature increases from 0 to 25 °C, the removal percentage increases until it reaches 99.96 % at 25 °C. This may be explained by the increase in the rate of diffusion of metal ions across the external boundary and the internal pores of the adsorbent particle.²⁹ It was also observed that with an increase in temperature from 25 to 40 °C, there is a slight decrease in the percentage removal of metal ions which indicates that the adsorption is an exothermic process. The low temperature (25 °C) of maximum adsorption demonstrates the domination of a physical adsorption phenomenon. We noted that there is a small increase of the removal percentage at 60 °C, which may be due to the presence of a chemisorption process.

Effect of contact time

We have studied the effect of the contact time for a range between 0 and 180 min. As it can be shown on the Figure 4, AC can eliminate 99.8 % of the Pb(II) with a contact time of 120 min. It can be seen that the rate of adsorption was high within the first 5 minutes, then it decreases when equilibrium was reached after 20 min. Afterwards, a slight

increase from 99.62 to 99.8 % of the percentage removal of Pb(II) was detected as contact time passes from 30 to 120 minutes. After reaching the equilibrium at 120 min, the removal percentage remained constant with increasing contact time because of the saturation of the sorption sites. The rapid adsorption during the initial stage can be attributed to the availability of a large number of vacant sorption sites for adsorption at this stage.³⁰

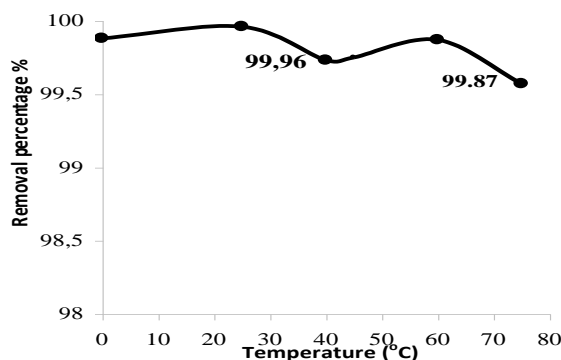


Figure 3. Effect of temperature on the removal of Pb(II).

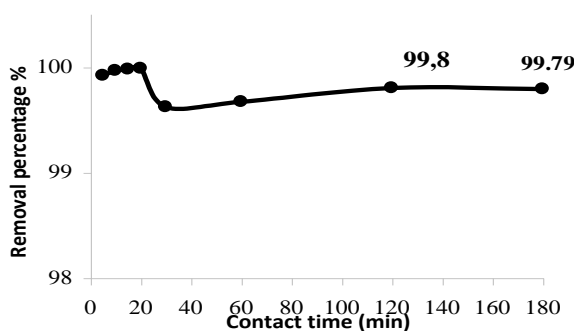


Figure 4. Effect of contact time on the extent of removal of Pb(II).

Effect of amount of adsorbent

The percentage removal of the metal ion increases with increasing amount of the adsorbent (Figure 5). This is due to an increase in the effective surface area, hence making it easier for Pb(II) to access the specific sorption sites. The graph shows that 1g of adsorbent is needed to remove substantially all of the metal ions (150mg L^{-1} of Pb(II)).

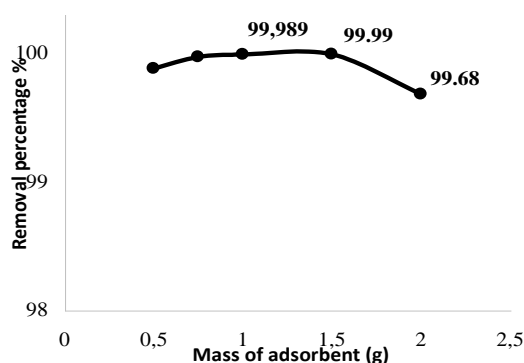


Figure 5. Effect of mass of adsorbant on the removal of Pb(II).

However, after equilibrium was reached, increasing the amount of the adsorbent has no effect on the Pb(II) removal, however the small decrease of the percentage removal corresponding to 2 g of mass adsorbent may be attributed to the formation of adsorbent aggregates at higher solid mass leading to a decrease in the surface area and an increase in diffusion path length.³¹

Isotherms

The experimental data were fitted to Langmuir and Freundlich models (Figures 6 and 7).

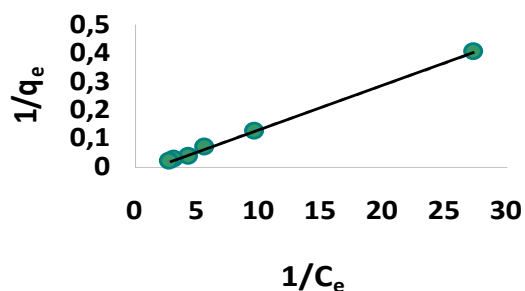


Figure 6. Langmuir isotherm of adsorption of Pb(II) on AC.

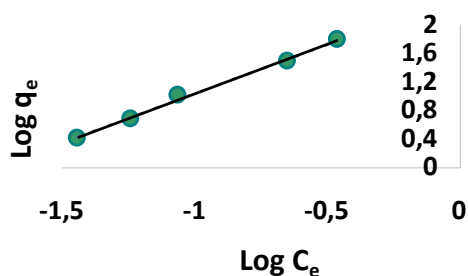


Figure 7. Freundlich isotherm of adsorption of Pb(II) on AC.

The linear plot of $1/q_e$ versus $1/C_e$ has a correlation coefficient $R^2 = 0.999$ for Langmuir isotherm. Freundlich isotherm represented by the plot of $\log q_e$ versus $\log C_e$ shows linearity with a correlation coefficient $R^2 = 0.995$. Langmuir model provided the best correlation for the experimental data. However, the maximum amount adsorbed, q_{max} , could not be calculated because the straight line $1/q_e = f(1/C_e)$ has a negative y-intercept. This negative value is most probably due to the weight of the points of the isotherm corresponding to very low concentrations of pollutant. Hence the adsorption of Pb(II) does not follow the Langmuir model.³²

The application of Freundlich isotherm showed a high correlation coefficient of 0.995 with the adsorption intensity $n = 1.3875$ and $K_F = 254.68$, indicating that the adsorption corresponds to a physical process. The Freundlich isotherm thus better models the adsorption of Pb(II) by the AC of *C. citratus* as compared to that by the Langmuir isotherm.

Kinetic study

To determine the kinetic for Pb(II) adsorption on the AC of *C. citratus*, the experimental data were analysed by the pseudo-first-order and pseudo-second-order kinetic models (Figures 8 and 9). The pseudo-first order model showed a very poor correlation coefficient ($R^2 = 0.6306$) and the value of q_e is 0.00327. In comparison, the pseudo-second order plot has an excellent coefficient correlation ($R^2 = 1$). The values of k_2 and q_e are 4.0566 and 14.97 respectively. These values obtained are comparable with the experimental ones. These observations indicate the applicability of the second kinetic model to the adsorption of Pb(II) onto the AC.

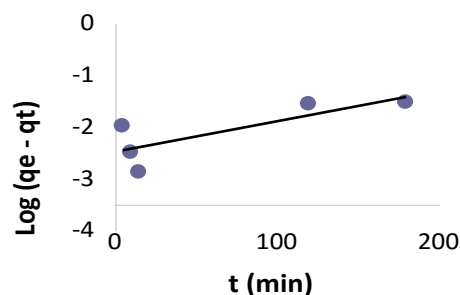


Figure 8. First order plot of the adsorption of Pb(II) on AC.

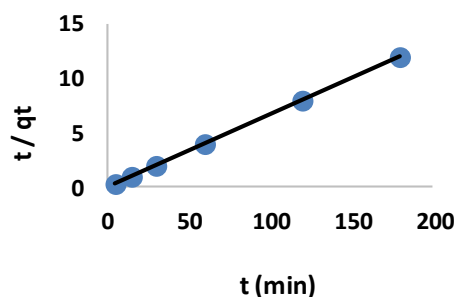


Figure 9. Second order plot of the adsorption of Pb(II) on AC.

Thermodynamic study

The thermodynamic parameters are recorded in Table 1. ΔH^0 is negative suggesting that the process is exothermic and it is not necessary to increase the temperature to be favourable, this is verified by the effect of the temperature (Figure 3) on the adsorption where the maximum capacity is at 25 °C. ΔS^0 is negative due to a decrease in randomness at the solid-liquid interface. However, its very small value suggests that there is no material change in randomness.

Table 1. The thermodynamic parameters.

T (K)	ΔG^0	ΔH^0	ΔS^0
298	13.91	-40.7	-0.09
333	-12.09		
348	-9.07		

Comparative study

We have earlier studied the removal of Pb(II) with the stem of *C. Citrates*.¹⁶ It is useful to compare the efficiency of the AC derived from the plant and the plant itself.

The maximum adsorption capacity, for the same concentrations of Pb(II), is shown to be greater for the AC than the original plant. This indicates the saturation of the surface of the crude *C. citratus* at lower concentration of Pb(II) than that of AC. The study of the effect of pH showed that the removal of Pb(II) by *C. citratus* requires a more acidic medium than the one required for the AC. Further, at the respective optimum pH values, the removal of Pb(II) the AC removed 99.97 % of Pb(II), which is greater than that by crude *C. citratus*. The adsorption of metal ions by *C. citratus* requires gentle heating while the AC can remove a larger amount at room temperature. The percentage removal of Pb(II) after 2 h by *C. citratus* is lower than that by AC and this shows a higher efficiency of the AC to eliminate almost whole of the metal in a relatively short time. Finally, weight to weight the AC is more efficient than the plant itself for the removal of Pb(II).¹⁶

Conclusion

This study was performed to determine the influences of batch parameters on the removal of Pb(II) in aqueous solution by the activated carbon of *C. Citrates*. We have demonstrated that it is better to transform *C. Citratus* to activated carbon to ensure more efficient removal of Pb(II). Therefore the AC of Lebanese *C. citratus* can be considered as a low cost, eco-friendly and effective adsorbent for treatment of waste water containing Pb(II).

The adsorption process was best described by the Freundlich model. The kinetic data were in good agreement with the pseudo-second-order kinetic model. Thermodynamic parameters which included Gibbs free energy, enthalpy and entropy of adsorption have also been determined.

Acknowledgement

The Lebanese University is gratefully acknowledged for the financial support.

References

- ¹Sekirifa, M.L., Hadj, M., *Sci. Technol.*, **2005**, 23, 55–59.
- ²Jadia, C. D., Fulekar, M. H., *Environ. Eng. Manag. J.*, **2008**, 7(5), 547–558.
- ³Blum, W. E. H., Horak, O., Mentler, A., Puschenreiter, M., *Trace Elements in: Environmental and Ecological chemistry*, vol. II, **2001**.
- ⁴Ponangi, S., Shyam, R.A, Joshi, S.G, *J. Indian Assoc. Environ. Manag.*, **2000**, 16-24.
- ⁵Moradi, S. E., Baniamerian, M. J., *Chem. Ind. Chem. Eng. Q.*, **2011**, 17(4), 397–408.
- ⁶WHO, *Guidelines for Drinking-Water Quality*, **1984**.
- ⁷EPA, *National Primary Drinking Water Regulation*, Washington, **2002**.
- ⁸Boeglin, J.-C., Petitpain-Perrin, P. G. F., Mouchet, P., Roubaty, J.-L. Delporte, C.A. Truc, Guibelin, E., Gay, J., *Techniques de l'ingénieur. Dossiers G1100, G1110, G1150, G1170, G1171, G1172, G1210, G1220, G1250, G1270, G1271, G1300, G1310, G1330, G1450, G1451, G1455 R.*, **2008**.
- ⁹Fu, F., Wang, Q., *J. Environ. Manage.*, **2011**, 92(3), 407–418.
- ¹⁰Bailey, S., Olin, T., Bricka, R., Adrian, D., *Water Research*, **1999**, 33, 2469–2479..
- ¹¹Miyah, Y., Idrissi, M., Zerrouq, F., *J. Mater. Environ. Sci.*, **2015**, 6(3), 699–712.
- ¹²Tarbaoui, M., Oumam, M., El Amraoui, B., Fourmentin, S., Benzina, M., Charrouf, M., Bennamara, A., Abourriche, A., *J. Mater. Environ. Sci.*, **2014**, 5, 2163–2168.
- ¹³Golab, Z., Smith, R. W., *Miner. Eng.*, **1992**, 5, 1003–1010.
- ¹⁴Jusoh, A., Shiung, L. S., Ali, N., Noor, M. J. M. M., *Desalination*, **2007**, 206, 9–16.
- ¹⁵Moussawi, M. A., Rammal, W., Hijazi, A., Naoufal, D., *Am. J. pharmtech Res.*, **2014**, 4(5), 389-398.
- ¹⁶Sobh, M., Moussawi, M.-A., Rammal, W., Hijazi, A., Rammal, H., Reda, M., Toufaily, J., Hamieh, T., *Am. J. Phytomedicine Clin. Ther.*, **2014**, 2(9), 1070–1080.
- ¹⁷Bamba, D., Dongui, B., Trokourey, A., Robert, D., Weber, B., *J. Soc. Ouest-Afr. Chim.*, **2008**, 25, 45–54..
- ¹⁸Lamoree, M. H., Swart, C. P., van der Horst, A., van Hattum, B., *J. of Chromatogr. A*, **2002**, 970, 183–190.
- ¹⁹kamura, H., Watanabe, T., Aoyama, I., Hasobe, M., *Chemosphere*, **2002**, 46(7), 945–951.
- ²⁰El Madani, M., Guillard, C., Perol, N., Chovelon, J. M., El Azzaoui, M., Zrineh, A., Herrmann, J. M., *Applied Catalysis B: Environmental*, **2006**, 65, 70–76.
- ²¹Al-afy, N., Hijazi, A., Rammal, H., Reda, M., Annan, H., *Am. J. Environ. Eng.*, **2013**, 3(4), 179–186.
- ²²Idris, S., Ndamitso, M. M., Iyaka, Y. A., Muhammad, E. B., *J. Chem. Eng.*, **2012**, 1(1), 11–24.
- ²³Freundlich, H.M. F., *J. Phys. Chem.*, **1906**, 57, 385–470.
- ²⁴Lagergren, S., *K Sven. Vetenskapsakad Handl*, **1898**, 4, 1 – 39.
- ²⁵Ho, Y. S., Mckay, G., *Chem. Eng. J.*, **1998**, 70, 115-124.
- ²⁶Kumar, P. S., Ramalingam, S., Kirupha, S. D., Murugesan, A., Vidhyadevi T., Sivanesan, S., *Chem. Eng. J.*, **2011**, 167(1), 122-131.
- ²⁷Kumar, P. S., Ramalingam, S., Senthamarai, C., Niranjanaa, M., Vijayalakshmi, P., Sivanesan, S., *Desalination*, **2010**, 261(1), 52–60.
- ²⁸Qiu, Y., Cheng, H., Xu, C., Sheng, G. D., *Water Res.*, **2008**, 42(3), 567–574.
- ²⁹Mulgund, M. G., Kininge, P. T., Pillai, M. M., Sanandam, M. R., *Int. J. Eng. Sci. Technol.*, **2011**, 3(2), 1642–1647.
- ³⁰Lee, L. Y., Lee, Chia, X. J., Tan, P. C., Gan, S., *J. Taiwan Inst. Chem. Eng.*, **2014**, 45(4), 1764–1772.
- ³¹Sari, A., Tuzen, M., Uluo D., Soylyk, M., **2007**, *Biochem. Eng. J.*, **2007**, 37(2), 8–151.
- ³²Sakr, F., Sennaoui, A., Elouardi, M., Tamimi, M., Assabbane, A., *J. Mater. Environ. Sci.*, **2015**, 6(2), 397–406.

Received: 14.01.2016.

Accepted: 21.02.2016.



HEAT-RESISTANT ELECTROPLATINGS OF INDUSTRIAL FUNCTION

Gulnara Kipiani^[a], Grigol Mamniashvili^[b], Nodar Gasviani^[a], Sergo Gasviani^[a], Lia Abazadze^[a], Tatiana Melashvili^[c].

Keywords: electrolysis of fused salts, electroplating, nickel, molybdenum, electrical and mechanical properties.

The heat-resistant nickel- and nickel-molybdenum electroplatings of high quality were prepared on copper and aluminum bases using the method of galvanic electrolysis. The platings are uniform, non-porous and are characterized by high adhesion. The optimal parameters of the process (current density, electrolysis duration, ratio between anode currents of molybdenum and nickel) are determined. MicroX-ray and fluorescence analyses of the obtained samples are carried out. Molybdenum content in the plating is determined. The existence of fine-dispersed phases of MoNi₃ and MoNi₄ are established. Electrical and mechanical properties of above – mentioned platings are studied after the heat treatment for their operation at high temperatures.

* Corresponding Authors

Fax:

E-Mail:

[a] Nodari Gasviani – Georgia, Tbilisi, Vazha-Pshavela avenue, block 5, building 4, flat 130. nodargasviani@mail.ru
+995 599 14 39 50

[b] Gulnara Kipiani - Georgia, Tbilisi, Maruashvili str. 40.

close to ruthenium, but the technology of its coating is less labor-intensive than the technology of ruthenium coating. Therefore its use in nuclear reactors, operating on molten-saline fuel compositions, is of particular importance.^{3,4}

EXPERIMENTAL

The goal of the present research is the preparation of nickel, nickel-molybdenum platings on copper and aluminum bases by electrochemical method, investigation of their metallographic, electrical and mechanical properties.

Nowadays the preparation of the mentioned platings by thermal method involves a number of technical difficulties. On the basis of the electrochemical properties the reduction of molybdenum from aqueous solution is impossible (it is obtained by fused electrolysis). Molybdenum is readily reduced from aqueous electrolytes as simultaneous co-deposit with nickel. The potentials of electrochemical reduction of Ni and Mo in aqueous solution are close to each other ($\varphi_{\text{Ni}/\text{Ni}^{+2}} = -0,257 \text{ V}$, $\varphi_{\text{Mo}/\text{Mo}^{+6}} = -0,200 \text{ V}$), which provides their combined electro-reduction in quasi-equilibrium condition and alloy formation at base surface.

Various compositions of the electrolytes for preparation of Ni-Mo platings are well-known.⁵⁻⁷ We have selected a pyrophosphate electrolyte, characterized by high stability and scattering power. It does not require the plating on aluminum bases, and has a high negative value of reduction potential and tendency to pass into ionic state. The immersion of aluminum into nickel plating electrolyte allows aluminum dissolution and electrolyte correction over a long period of time and the preparation of a qualitative plating.

Electrochemical investigations were performed by galvanic static method by using the Cu and Al cathodes and simultaneous application of Mo and Ni as the anodes at various ratio of anode current. The preliminary treatment of the base (Cu, Al) surface was carried out before the electrolysis.

INTRODUCTION

Rapid development of the technique and creation of new technologies enhances the demand on new materials. Preparation of new corrosion- and heat-resistant and heatproof composite materials as well as the plating on the basis of rare and high-melting metals is necessary. The mentioned platings are used in a number of fields including agriculture, atomic and space industries etc. This clearly demonstrates a necessity for the study of the processes of preparation of mentioned platings.

As is well-known, chromium platings are characterized by good physical-mechanical properties, but toxicity and cancerogenicity of chromium electrolytes and the reduction of hardness at high temperatures requires the search of alternative technologies for preparation of heatproof and corrosion-resistant platings.

Electrochemical deposition of nickel-based alloys with high-melting metals (Mo, W, Co and etc.) is one of the alternatives. By combining these metals the hard materials are obtained, characterized by high wear-resistance and strength at elevated temperatures together with a good heat- and electrical conduction. Alloys of nickel with Mo, W, Co and other high-melting metals are characterized by considerably higher corrosion resistance than nickel, cobalt, molybdenum and tungsten.^{1,2} Ni-Mo alloys possess a high mechanical strength and are wear resistance (microhardness of nickel-molybdenum galvanic deposition comprises 550-600 kg-force mm⁻² at 20 mass %). Above listed indexes determine its advantageous use in magnetically operated contacts (sealed switches), as barrier sub-layers for gold, ruthenium and gold alloys, which gives an economy of 60-90% depending on sealed switch type. By its physical characteristics and corrosion resistance the alloy Ni-Mo is

Table 1. Dependence of current efficiency and plating (Ni-Mo on Cu and Al bases) thickness on the ratio I_{Ni}/I_{Mo} and on electrolysis duration. [Electrolyte:pyrophosphate, current density: 0.05A/cm², T=313K, anode: (Ni, Mo)]

Base	Ratio I_{Ni}/I_{Mo}	Electrolysis duration, min.	Plating thickness, μm	Current efficiency, %
Cu	2	30	25	84
		60	44	69
	2,5	30	21	75
		60	14	25
	3,0	30	21	75
		60	14	25
3,5	30	21	75	
	60	14	25	
Al	2	30	18	57
	3	60	14	23
Al-Ni	2	30	15	50
	3	30	8	22
	4	30	11	34
Al-Cu	2	30	4	63
	3	30	8	25
	7	90	58	13

The complexity of aluminum plating on the surface is due to the presence of hard oxide film. Another reason is complicating technology of plating on aluminum bases, the high negative value of its reduction potential and its tendency to pass into ionic state. In immersing aluminum into nickel plating electrolyte, there is aluminum dissolution and contact deposition of loose nickel precipitate ($\varphi_{st,Al}=-1.66$ V, $\varphi_{st,Ni}=-0.25$ V). This process inhibits an adhesion of plated metal with a base. Therefore, aluminum samples after pickling and washing are treated by zincate solution.

As a result of contact exchange reaction an oxide film at aluminum surface is dissolved and is plated by a thin layer of metallic zinc. This fact provides a high adhesion of nickel plating with aluminum base.

RESULTS AND DISCUSSION

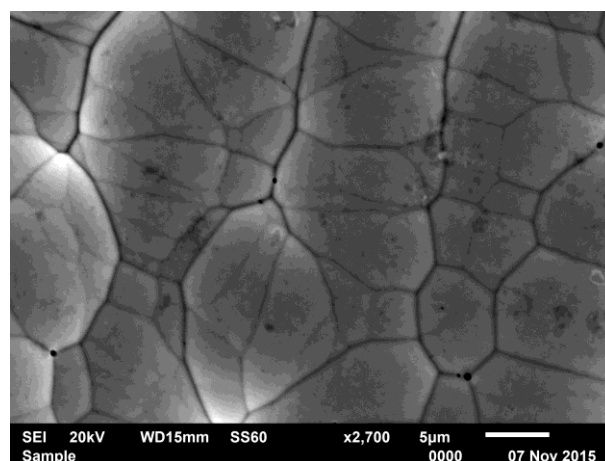
For preparation of Ni-Mo plating (on copper and aluminum bases) the galvanic static investigations are performed at various electrolysis parameters (current density, electrolysis duration, various ratio of I_{Ni}/I_{Mo}).

Results for Ni-Mo plating (on copper and aluminum bases), obtained from pyrophosphate electrolyte, are presented in Table 1.

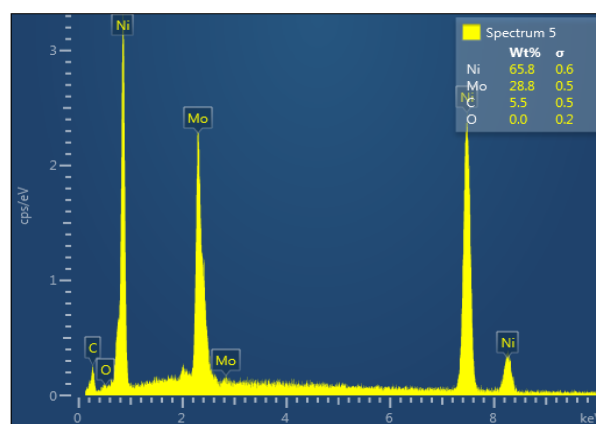
Optimal parameters of the electrolysis are defined. The presence of the intermetallides, MoNi_3 and MoNi_4 , as fine-dispersed phases is established. The platings are uniform, non-porous and are characterized by a high adhesion. The content of molybdenum in the alloy is determined which correlates well with the results of X-ray fluorescence analysis.

The Mo content on copper and aluminum bases is 31.95 mass% and 27.22mass% respectively. .

Comparison of the results obtained with the state diagram of binary metallic systems⁸ have shown that MoNi_4 and MoNi_3 intermetallides –are obtained on aluminum and copper bases.

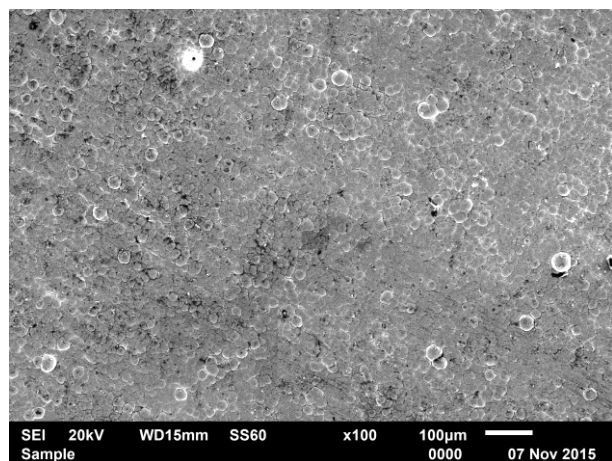


a

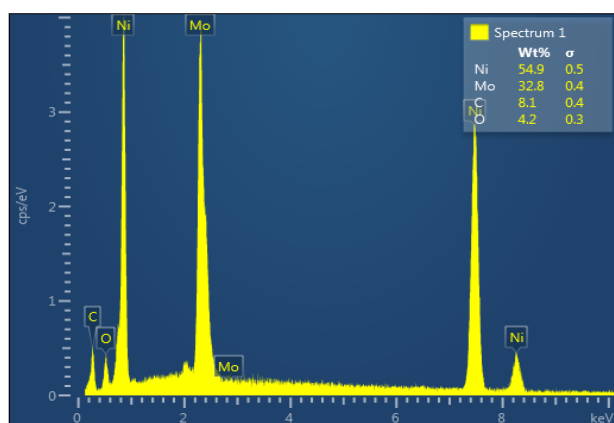


b

Figure 1. Results of microscope research of Ni-Mo plating on aluminum: a) electronic image; b) micro X-ray spectrum;



a



b

Figure 2. Results of microscope research of nickel-molybdenum plating on copper: a) electron image; b) microX-ray spectrum.

The analysis of obtained Ni-Mo platings was carried out at scanning electron microscope of JSM-65102V type. Electrical (specific resistance) and mechanical (Young modulus and internal friction) properties of nickel and nickel – molybdenum plating are studied by electron beam technology. The samples of required size are cut out at electro-spark discharge machine for particular exactness. The samples are annealed, before an experiment, in vacuum at 673K for one hour. Thereafter the specific resistance was measured for base material (copper and aluminum) as well as for the samples plated by nickel and nickel – molybdenum at various temperatures. Hereafter, the mentioned samples were placed in vacuum chamber and were subjected to short term heating at 873-1273 K for 30 seconds and their specific resistance was measured afresh. The standard four-point contact method was used for measuring the electric resistance, which is highly useful for control of composition structure.⁹ The results obtained for nickel platings on copper and aluminum bases are presented in Fig. 3 and those for nickel-molybdenum platings are in Fig. 4.

Measurement of internal friction is one of the most sensitive methods to determine the structural defects, relaxation and diffusion providing the necessary information about the processes in the solids (metals and alloys) in the conditions of strong mechanical and heat effects of various type.¹⁰

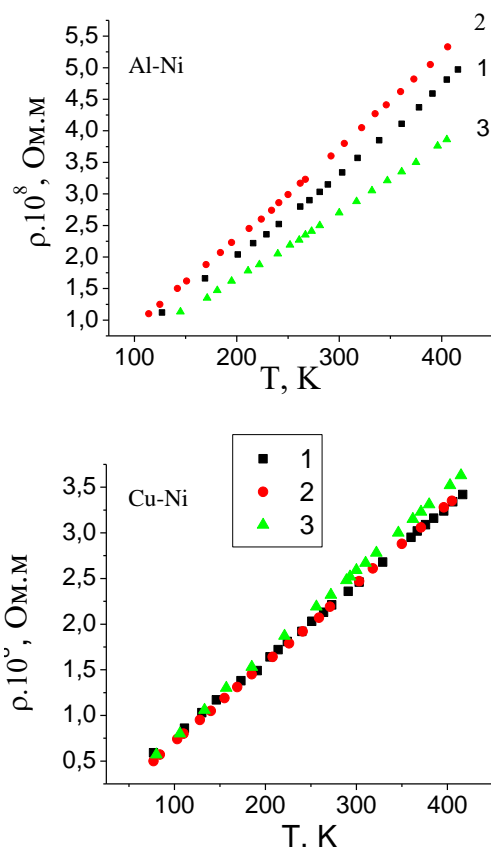


Figure 3. Temperature dependence of specific electrical resistance of nickel plated aluminum and copper, $\rho=f(T)$. 1-initial sample, 2- after annealing at 673K, 3- after annealing at 873K (for aluminum base) and at 1273K (for copper base)

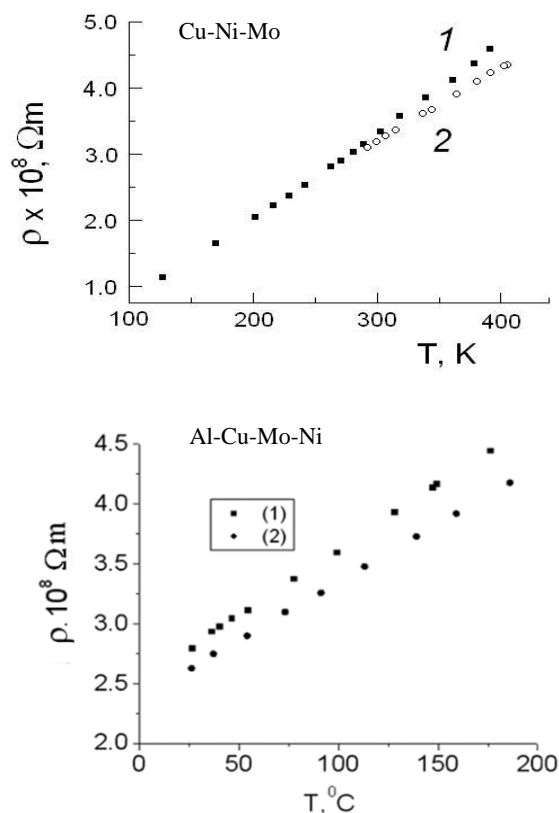


Figure 4. Temperature dependence of specific electrical resistance of nickel-molybdenum plated copper and Al-Cu, $\rho=f(T)$. 1-Initial sample, 2- after annealing at 873K (for aluminum base) and at 1273K (for copper base).

Young modulus and internal friction of aluminum and copper bases, plated with nickel (Fig. 5) and Ni-Mo (Fig. 6), were measured with acoustic spectrometer. $E(T)$ and $Q^{-1}(T)$ for initial samples were compared before and after thermal treatment with the shock heating (over one minute) of aluminum plated bases to 873K and copper bases to 1273K (in helium atmosphere). Thereafter these samples were kept in vacuum for 30 seconds and cooled to room temperature (Fig. 5)

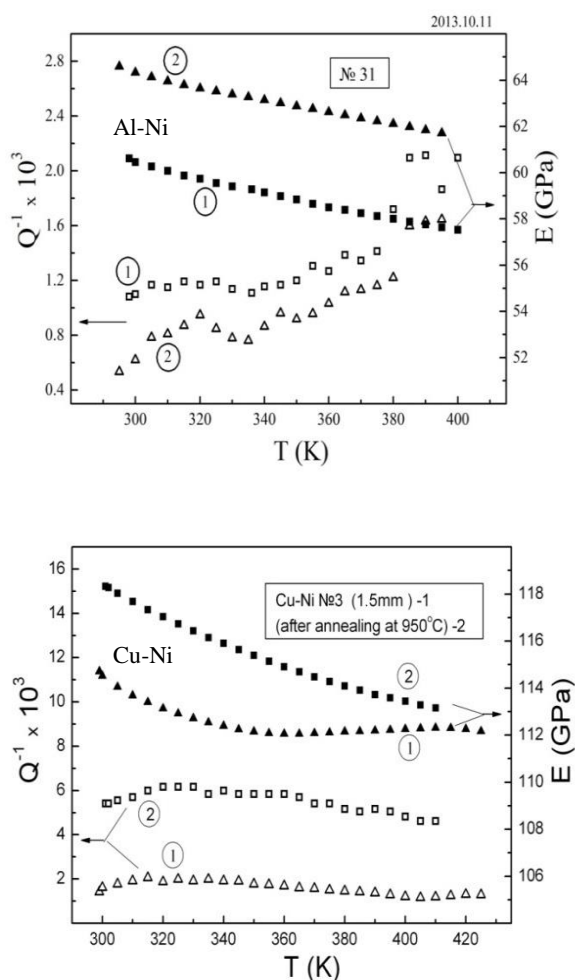


Figure 5. Temperature dependences of Young modulus (E) and of internal friction (Q^{-1}) for a nickel plated aluminum and copper, $\rho=f(T)$. 1-Initial sample, 2- after annealing at 873K (for aluminum base) and at 1273K (for copper base).

It is evident from Fig. 5 that the values of Young modulus for aluminum bases lie in the range of 40-65 GPa which are much the same as that for aluminum (70 GPa). Modulus variation in the range under measurement is $\approx 4\%$.

The level of internal friction after thermal treatment decreases. The values of Young modulus for copper bases lie in the range of 112-118 GPa and are much the same as for copper (110 GPa). There are slight variations of Young modulus and the level of internal friction. At higher temperatures, Young modulus coincides with the Young modulus of copper.

It is evident from results in Fig.6 that the values of Young modulus lie in the range of 95-105 GPa which are much the same as that for pure copper (110 GPa). It varies by $\approx 2\%$ up to 393-423 K and increases slightly after heating to 1273 K. There is no significant variation of Q^{-1} , the internal friction, in the temperature range under measurement and increases slightly after heating at 1273K.

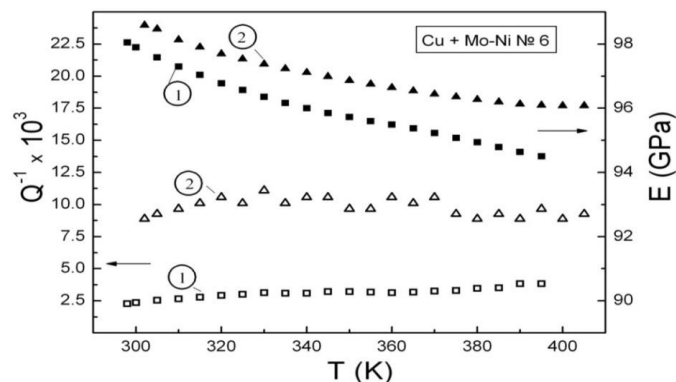


Figure 6. Temperature dependences of Young modulus (E) and of internal friction (Q^{-1}) for a nickel-molybdenum plated aluminum and copper, $\rho=f(T)$: 1- Initial sample, 2- after annealing at 873K (for aluminum base) and at 1273K (for copper base).

Electrical and mechanical properties of copper and aluminum bases, plated by nickel and nickel-molybdenum, were studied. On the basis of performed investigations it may be concluded that prepared corrosion- and heat resistant platings retain their electrical and mechanical properties after thermal treatment to 873K for aluminum bases and to 1273K for copper base.

REFERENCES

- Vasko, A. T., Kovach, S. K., *Electrochemistry of high-melting alloys*. -K: Technique, **1983**, p.160 (Russian)
- Marlot, A., Kern, P., Landolt, D., *Electrochim. Acta.*– **2002**, *48*; 29-36.
- Shiskina, L. V., Karabanov, S. M., Lokshantova, O. G., *Herald of RSTU №3*, (issue 29), Ryazan, **2009**, p/p. 124-127 (Russian).
- Vyacheslavov, P. M. *Electrolytic deposition of alloys*. L. Mashinostroenie, **1971**, p.294 (Russian).
- Kuznetsov, V. V., Pavlov, M. R., Kuznetsov, K. V., Kudryavtsev, V. *NElectrochimia*, *39*(12), 2003, 1494-1498 (Russian).
- Pavlova, N. V., Nanda, T. U., Pavlov, M. R., Kudryavtsev, B. N., *Galvanotechn. Surface Treatment*, **2008**(4), p.22-29 (Russian).
- Kuznetsov, V. V., Morozova, N. V., Kudryavtsev, V. N. *Electrochimia*, **2006**, *42*(6), p. 741-745(Russian).
- State diagrams of binary metallic systems*. Edited by Lyakishev H.P. Mashinostroenie, **1996**, p.1036 (Russian).
- Peikrshvili, A. B., Kecskes, L. J., Chagelishvili, E. Sh., Klotz, B. R., Mamniashvili, G. I., Godibadze, B. A. *EURO PM2009*. Proc.**2009**, *3*, p. 33-40.
- Nowick, A.S., Berry, B.S. "Inelastic Relaxation in Crystalline Solids", Academic Press, New York/London, 1972.

Received: 20.12.2015.

Accepted: 22.02.2016.



QUANTITATIVE ANALYSIS ON CELLULAR UPTAKE OF LANTHANUM OXIDE NANOPARTICLES IN THE PRIMARY OSTEOBLASTS IN VITRO

Yanyan Ma, Zhu Liu, Yunfei Li, Demin Zhu, Da Wang, Wenying Wang, Zhilin Li*, Guoqiang Zhou*

Keywords: Rare earth metal oxides; Lanthanum oxide nanoparticles; Cellular uptake; Osteoblasts; Nanotoxicity

With the fast developing nanotechnology, questions are being raised about the potential toxic effects of the nanomaterials on human health. The effects of lanthanum oxide nanoparticles on the primary osteoblasts are investigated in the present study. As an indicator of membrane damage, lactate dehydrogenase is quantitatively assessed. The quantitative analysis on cellular uptake of lanthanum oxide nanoparticles could be detected by flow cytometer and inductively coupled plasma mass spectrometry respectively. The results demonstrate that lanthanum oxide nanoparticles can enter cells through cell membrane and the nanoparticles taken up by the cells followed dose and time dependent effect. The method could be used for the initial screening of the uptake potential of nanoparticles as an index of nanotoxicity.

*Corresponding Authors

E-Mail: lizhilin@hbu.edu.cn, zhougq1982@163.com
Key Laboratory of Chemical Biology of Hebei Province,
College of Chemistry and Environmental Science, Hebei
University, Baoding, 071002, China

evaluated using cultured primary osteoblasts (OBs) in vitro. The analytical method using flow cytometer and inductively coupled plasma mass spectrometry can accurately reflect the amounts of La_2O_3 taken up by cells. This method can be used for the initial screening of uptake by cells as an index of nanotoxicity.

Introduction

The rapidly developing nanotechnology is providing a wide range of applications for nanomaterials.¹ Several of these have been proposed for application in fields of material, medical, biosciences, computer, and information technology.² Nanoparticles of metal oxide have attracted significant interests because of their atom-like size dependent properties.³ Rare earth elements have unique physical and chemical properties due to their 4f orbital electron, such as high density, high melting point, high thermal conductance and conductivity.⁴ Because of these unique properties, rare earths have been extensively used in medical, biomedical, electronics, and agronomic fields.⁵ Lanthanum oxide (La_2O_3), as one of rare earth metal oxides, has a band gap of 4.3 eV and the lowest lattice energy with high electric constant.⁶ La_2O_3 is used in several areas including electronics, fuel cells, optics, magnetic data storage, ceramics, catalysis, water treatment and biomedicine.⁷⁻⁹ La_2O_3 is used to make optical glasses and improves the density, refractive index, and hardness of the glass.¹⁰ It is also used as a catalyst for the oxidative coupling of methane.¹¹ The possible applications of these materials have not been fully explored especially in the field of biomedical sciences. To the best of our knowledge, no studies have looked into the cellular uptake and potential toxicity of La_2O_3 nanoparticles in cultured primary osteoblasts (OBs).

In this report, the size, morphology, structure and chemical composition of La_2O_3 nanoparticles are characterized using scanning electron microscopy (SEM), X-ray powder diffraction (XRD), and dynamic light scattering (DLS) techniques. Furthermore, the cellular uptake and potential toxicity of La_2O_3 nanoparticles were

Experimental

Materials and reagents

The Lanthanum nitrate hexahydrate ($\text{La}(\text{NO}_3)_3 \cdot 6\text{H}_2\text{O}$), and urea ($(\text{NH}_2)_2\text{CO}$) are the products of Kemiou Chemical Reagent (Tianjin, China). Kunming (KM) mice are procured from the Animal Center of Hebei Medical University. Dulbecco's modified Eagle's medium (DMEM) and trypsin are sourced from Gibco. 3-(4,5-dimethylthiazol-2-yl)-2,5-diphenyltetrazolium bromide (MTT), penicillin, streptomycin and cetylpyridium chloride are from Sigma-Aldrich. Fetal bovine serum (FBS) is obtained from Hangzhou Sijiqing Organism Engineering Institute. A LDH kit is obtained from the Nanjing Jiancheng Biological Engineering Institute (Jiangsu, China). All other reagents used in this study are of analytical grade.

Preparation of La_2O_3 nanoparticles

The La_2O_3 nanoparticles are prepared via an urea-based homogeneous precipitation process. 5 mL of $\text{La}(\text{NO}_3)_3$ (1 M) is dissolved in 300 ml of deionized water and stirred for 15 minutes to obtain a clear solution. Next, 15 g of $(\text{NH}_2)_2\text{CO}$ is slowly added to the clear solution of $\text{La}(\text{NO}_3)_3$ with vigorous stirring. The resulting solution is homogenized using a magnetic stirrer at 25 °C for 1 h. This solution is heated at 95 °C for 3 h. The final precipitate is centrifuged and washed several times with water and anhydrous ethanol, and subsequently dried at 100 °C for 5 h. The obtained precursor is heat treated at 800 °C for 2 h with a heating rate of 2 °C min⁻¹.

Characterization of La₂O₃ nanoparticles

The morphology and size of La₂O₃ nanoparticles are measured by field emission scanning electron microscope (JSM-7500F, JEOL). A minute drop of nanoparticles solution is cast on to a carbon-coated copper grid and subsequently dried in air before transferring it to the microscope. X-ray powder diffraction is performed on a Bruker D8 Advance X-ray diffractometer employing Cu-K α radiation with 40 kV and 50 mA (D8 ADVACE, Bruker). The size distribution of the nanoparticles in medium is evaluated by dynamic light scattering (Delsa Nano C, Beckman). Data analysis is carried out on six replicated tests.

Cell viability assay

The primary OBs are prepared mechanically from three-days-old KM mouse calvarias following the sequential enzymatic digestion method described previously.¹² The viability of OBs is measured according to MTT method. In brief, OBs are seeded in 96-well culture plates at a density of 2×10^4 /well and incubated for 24 h. After incubation, La₂O₃ nanoparticles are added to the wells at concentrations of 5, 10, 20, and 40 $\mu\text{g mL}^{-1}$ and incubation continued for 24 h. The cells are incubated with La₂O₃ nanoparticles for 48 h at the same concentrations. Nanoparticles are sonicated and vortexed before being added to the cells. Cells without nanoparticles are used as control group. 10 μl of MTT solution is added to each well and the plates incubated for 4 h. The supernatant is removed and 100 μl DMSO is added to solubilize the MTT. The absorbance at 570 nm of each well is measured with a microplate spectrophotometer (BioRad Model 3550). The cell viability is calculated according to the formula: $\text{OD}_{\text{sample}}/\text{OD}_{\text{control}} \times 100$.

LDH measurement

Lactate dehydrogenase (LDH) activity in the cell medium is determined using a commercial LDH Kit. One hundred microlitres of cell medium is used for LDH analysis. Absorption is measured using a microplate spectrophotometer (BioRad Model 3550) at 340 nm. Released LDH catalyzed the oxidation of lactate to pyruvate with simultaneous reduction of NAD⁺ to NADH. The rate of NAD⁺ reduction is directly proportional to LDH activity in the cell medium and is measured as an increase in absorbance at 340 nm.

Flow cytometry assay

Cells are treated with La₂O₃ nanoparticles at several concentrations (5, 10, 20, and 40 $\mu\text{g/ml}$) for 24 h. Subsequently, the cells are washed three times with PBS, digested with trypsin, centrifuged and re-suspended in PBS. The amount of particles taken up by the cells is analyzed using a flow cytometer (FCM) (FACS Calibur, BD). In FCM, the laser beam (488 nm) illuminates cells in the sample stream which pass through the sensing area. The side scatter (SSC) light is the laser light scattered at about a 90° angle to the axis of the laser beam, and its intensities are proportional to the intracellular density.

Lanthanum content analysis

Cells treated with several doses of La₂O₃ nanoparticles are reacted with trypsin, then digested and analyzed for La content. Briefly, the cells are digested in nitric acid overnight and heated at about 160 °C the next day. At the same time, H₂O₂ solution is used to drive off the vapor of nitrogen oxides until the solution is colorless and clear. The volume of remaining solutions is fixed to 3 ml with 2 % nitric acid. Inductively coupled plasma-mass spectrometry (ICP-MS, Thermo Elemental X7, Thermo Electron Co.) is used to analyze the La concentration in each sample. Indium of 20 ng mL⁻¹ is chosen as an internal standard element.

Statistical analysis

Data are expressed as mean \pm standard deviation (S.D) from three independent experiments. Statistical evaluation is analyzed by a one-way ANOVA, followed by Tukey post-hoc analysis for multiple group comparisons. *P* values less than 0.05 are regarded as indicative of the statistical differences.

Results and discussion

Nanoparticle characterization

The SEM images provide information on the size and shape of the nanoparticles, however, it does not provide information whether the nanoparticles exist in single or aggregated forms in the culture medium. The morphology of La₂O₃ nanoparticles is rod (Figure 1). The length of rod is about 300 nm and the diameter is about 80 nm.

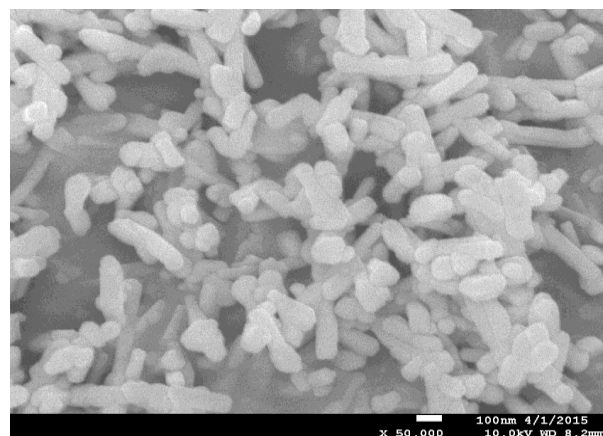


Figure 1. SEM image of La₂O₃ nanoparticles.

The XRD patterns of La₂O₃ nanoparticles indicate that only the La₂O₃ phase is found without any other phase, and all diffraction peaks could be indexed to hexagonal crystal system (JCPDS No. 00-054-0213). It also reveals that La₂O₃ nanoparticles exhibit sharp diffraction peaks, indicating a high crystallinity (Figure 2). The size distribution in the culture medium is investigated using a DLS method,¹² which shows that the average size of La₂O₃ in the culture medium is 183.5 ± 21.3 nm (Figure 3). The DLS analysis also shows that the La₂O₃ nanoparticles are homogeneously dispersed in culture medium.

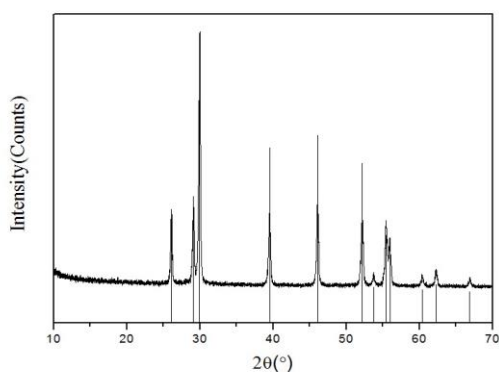


Figure 2. XRD patterns of La_2O_3 nanoparticles.

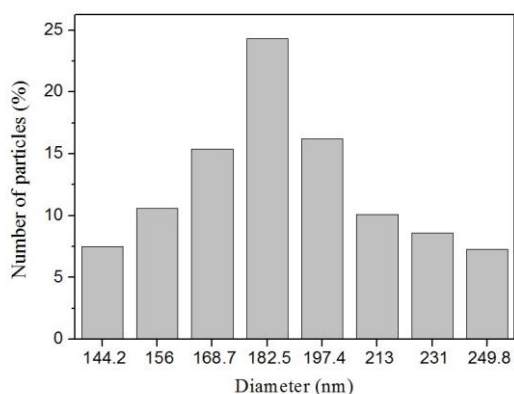


Figure 3. Size distribution of La_2O_3 nanoparticles in culture medium measured by DLS

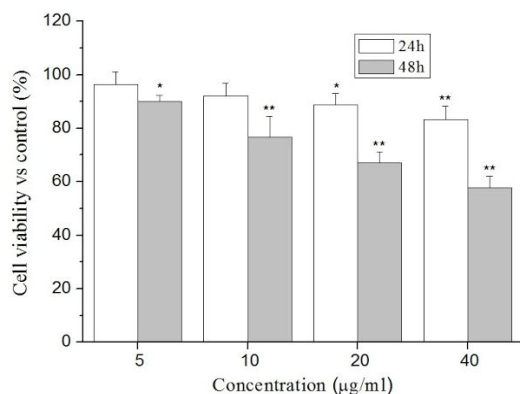


Figure 4. Viability of OBs after exposure to La_2O_3 nanoparticles. Values are mean \pm SD from three independent experiments. (* $P < 0.05$, ** $P < 0.01$ compared with the corresponding control group, $n=6$.)

Effects of La_2O_3 nanoparticles on the cell viability

The cell viability of OBs, after exposure to La_2O_3 nanoparticles at 10, 20, and 40 $\mu\text{g mL}^{-1}$, decreased to 92.1 %, 88.8 %, and 83.1 % respectively after 24 h, and the corresponding decrease after 48 h is 76.8 %, 67.1 %, and 57.7 % compared to the control. The inhibition effect of La_2O_3 nanoparticles is time and dose dependent and is lower at 24 h than that at 48 h (Figure 4).

LDH release after exposure to La_2O_3 nanoparticles

The cell membrane damage is reflected in the elevated LDH levels in the cell medium. The LDH levels in the cell culture increased in all groups. The increase in the cells after these have been exposed to La_2O_3 nanoparticles at 5, 10, 20 and 40 $\mu\text{g mL}^{-1}$, respectively for 48 h is 38.5 %, 61.5 %, 86.2 %, and 110.7 % compared with the control (Figure 5).

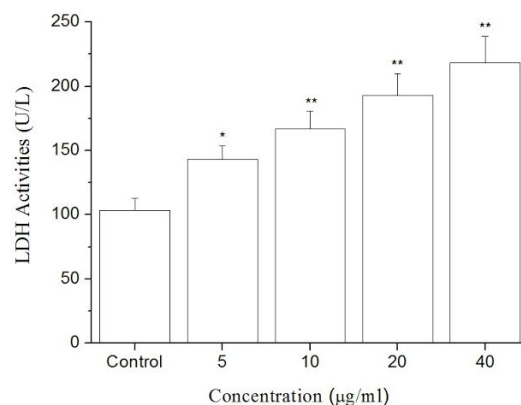


Figure 5. The LDH activities in the cell culture medium after exposure to La_2O_3 nanoparticles for 48 h. Values are mean \pm SD from three independent experiments. (* $P < 0.05$, ** $P < 0.01$ compared with the corresponding control group, $n=6$.)

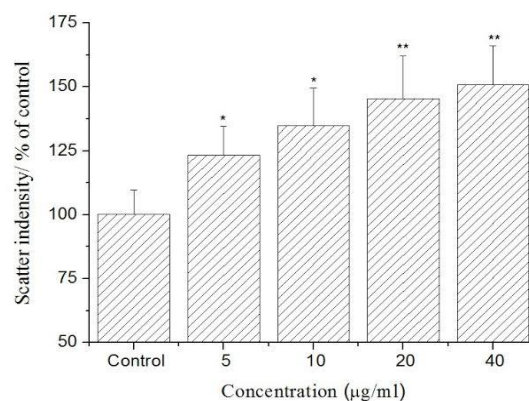


Figure 6. The cellular uptake of La_2O_3 nanoparticles. The cells were incubated with different concentrations of La_2O_3 nanoparticles for 24 h. Data are expressed as mean values \pm SD. (* $P < 0.05$, ** $P < 0.01$ compared with the corresponding control group, $n=6$.)

Flow cytometry analysis of La_2O_3 nanoparticles uptake

The scatter intensity of La_2O_3 nanoparticles is measured by quantitative analysis of the intracellular side scatter signal by flow cytometry. The scatter intensity increases markedly after cells are treated with nanoparticles compared with untreated group (Figure 6). The intensities of SSC reflect inner cell density and higher concentrations of La_2O_3 nanoparticles, i.e. the cells which take up higher doses of nanoparticles show higher intensities of SSC. This result suggests that the determination of SSC is a good way to judge the uptake potential of La_2O_3 nanoparticles. Using this experimental approach, a dose-dependent increase in cellular uptake of La_2O_3 nanoparticles is detected at doses from 5 to 40 $\mu\text{g mL}^{-1}$ after 24 h exposure.

ICP-MS analysis of the contents of lanthanum

ICP-MS analyses are further used to verify the uptake of La_2O_3 nanoparticles in OBs at different doses and time intervals. The contents of lanthanum in cells exposed to La_2O_3 nanoparticles are shown in Figure 7. Lanthanum could not be detected in controls. However, a dose- and time-dependent accumulation of La_2O_3 nanoparticles are measured in OBs after 24 and 48 h. The lanthanum content of the cells, after these are exposure to La_2O_3 nanoparticles at 5, 10, 20 and 40 $\mu\text{g mL}^{-1}$, is 8.9 ± 0.4 , 11.7 ± 0.8 , 23.8 ± 1.1 and 23.6 ± 1.2 ng mm^{-2} respectively after 24 h. The corresponding content of the cells at the same dose after 48 h of exposure increased to 9.8 ± 0.2 , 17.1 ± 0.7 , 29.0 ± 1.1 and 30.0 ± 1.2 ng mm^{-2} (Figure 7).

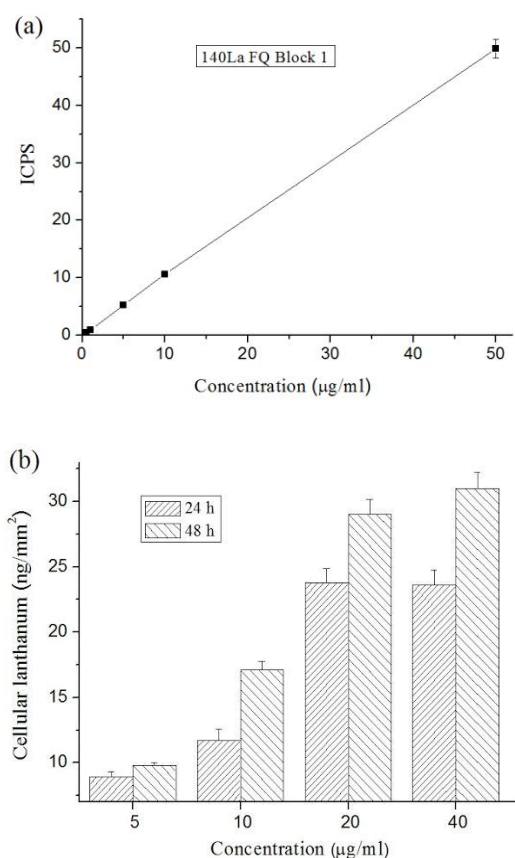


Figure 7. The contents of lanthanum in cells. The contents of lanthanum in cells are determined by ICP-MS. The data are expressed as mean \pm SD of three independent experiments. (a) Standard curve of the instrument. (b) The contents of lanthanum in cells.

Conclusion

In summary, rod-like La_2O_3 nanoparticles are synthesized successfully using urea-based homogeneous precipitation method. The results show that La_2O_3 nanoparticles have cytotoxic effects towards primary osteoblasts. La_2O_3 nanoparticles enter cells following dose and time-response effect.

At present, accurate, sensitive and cost-effective measurement techniques for characterizing them do not exist. Usage of nanomaterial will increase with the development of nanotechnology, and assessments of their risks to the environment and human health will also be required. Academia, industry, and regulatory governmental agencies should seriously consider the view that nanomaterial has new and unique biologic properties and the potential risks are not the same as those of bulk materials of the same chemistry. The simple method introduced in this study is useful for the initial screening of the uptake potential of insoluble nanomaterial in biological tissues and cells.

Acknowledgments

This work is supported by the National Natural Science Foundation of China (21471044 and 21001038), the Youth Talent Fund Project of Hebei Education Department (BJ2014007), the College Students Innovative Training Project of Hebei University (201410075072), and the Opening Laboratory Project of Hebei University (sy2015035).

References

- Wendelin, J. Stark., *Angew. Chem. Int. Ed.*, **2011**, *50*, 1242.
- Grainger, D. W., Castner, D. G., *Adv. Mater.*, **2008**, *20*, 867.
- Bojari, H., Malekzadeh, A., Ghiasi, M., *J. Clust. Sci.*, **2014**, *25*, 387.
- Huang, P. L., Li, J. X., Zhang, S. H., Chen, C. X., Han, Y., Liu, N., Xiao, Y., Wang, H., Zhang, M., Yu, Q. H., Liu, Y. T., Wang, W., *Environ. Toxicol. Pharmacol.*, **2011**, *31*, 25.
- Mekhemer, G. H., *Phys. Chem. Chem. Phys.*, **2002**, *4*, 5400.
- Bahari, A., Anasari, A., Rahmani, Z., *J. Eng. Technol. Res.*, **2011**, *3*, 203.
- Balusamy, B., Kandhasamy, Y. G., Senthamizhan, A., Chandrasekaran, G., Subramanian, M. S., Tirukalikundram, S. K., *J. Rare. Earth.*, **2012**, *30*, 1298.
- Nejad, S. J., Abolghasemi, H., Moosavian, M. A., Golzary, A., Maragheh, M. G., *J. Supercrit. Fluids.*, **2010**, *52*, 292.
- Khanjani, S., Morsali, A., *J. Mol. Liq.*, **2010**, *153*, 129.
- Ghiasi, M., Malekzadeh, A., *Superlattices. Microstruct.*, **2015**, *77*, 295.
- Vishnyakov, A. V., Korshunova, I. A., Kochurikhin, V. E., Salnikova, L. S., *Kinet. Catal.*, **2010**, *51*, 273.
- Zhou, G. Q., Gu, G. Q., Li, Y., Zhang, Q., Wang, W. Y., Wang, S. X., Zhang, J. C., *Biol. Trace. Elem. Res.*, **2013**, *153*, 411.

Received: 13.01.2016.

Accepted: 24.02.2016.



THE EFFECT OF SOME ANTHROPOMETRIC MEASUREMENTS AND SERUM LACTATE DEHYDROGENASE ON KNEE OSTEOARTHRITIS

Rana Kareem Al- Saady^[a] and Salah Mohammed Fizea^{[a]*}

Keywords: osteoarthritis, LDH, obesity, BMI.

Osteoarthritis (OA) is the most common degenerative joint disorder that ultimately results in the progressive destruction of articular cartilage. The occurrence of knee osteoarthritis (OA) increases with obesity and is more common in women compared with men. Thirty patients (20 females, 10 males) clinically diagnosed with knee OA admitted to Baghdad teaching hospital between January 2015-June 2015. Patients between 35-70 year of age and 30 healthy subject (20 females, 10 males) ages matched. The results showed that increased body mass index (BMI) is a well-recognized risk factor for knee osteoarthritis, and the effect of obesity is a stronger predictor of developing knee OA symptoms in women than men. There was also a significant difference between lactate dehydrogenase (LDH) in serum patients and control ($p < 0.01$). This study supported a positive association between systemic BMI and OA. Furthermore, serum LDH activity could be of diagnostic value for identifying osteoarthritis.

*Corresponding author

E-Mail: salahmf79@yahoo.com

[a] Department of Chemistry, College of Education for Pure Science, Ibn Al-Haitham, University of Baghdad, Iraq.

Introduction

Osteoarthritis (OA) has been characterized by progressive articular cartilage loss and osteophyte formation. Although OA was long considered to be due only to an imbalance between loss of cartilage and an attempt to repair cartilage matrix, it is now known that OA, at least in the knee, is a heterogeneous disease involving all the articular tissues including cartilage, subchondral bone, menisci, and periarticular soft tissues such as the synovial membrane. Synovitis is often present and is considered to be secondary to the alterations in other joint tissues. Yet, findings indicate that synovial inflammation could be a component of even the early events leading to the clinical stage of the disease.¹

Lactate dehydrogenase (LDH) is mainly an intracellular enzyme. It is responsible for interconversion of pyruvate and lactate in the cells. Its levels are several times greater inside the cells than in the plasma and are an enzyme that is expressed at higher levels when cells are distressed and damaged. Elevating LDH is a possible indication of disease progression.²

LDH helps facilitate the process of turning sugar into energy for cells to use. In inflammatory conditions like (rheumatoid arthritis) RA and OA, LDH may be released into the bloodstream causing its levels to increase and higher levels of LDH in the blood indicate acute or chronic cell damage.³

OA affects joint cartilage, adjacent skeleton, and surrounding soft tissue⁴ and may affect most joints. Major risk factors for OA include age and obesity. The mechanism concerning the association between Body mass index (BMI) and knee OA is not clearly understood. BMI is an established risk factor for knee OA.⁵

The mechanism of the association between BMI and knee OA traditionally was thought to be purely biomechanical, with the excess weight inducing deleterious effects on the joints. This makes the differing associations between knees OA with BMI surprising because the forces from body weight pass through the hips as well as the knees, although the different morphology of the joints might explain different abilities to withstand adverse mechanical loading. However, recent advances in adipose biology have suggested the possibility that other factors may affect the joints. Patterns of distribution of adipose tissue within the body and associations with metabolic syndrome are now known, and adipocytokines are secreted by and related to adipose tissue. The adipocytokine, leptin, is not related to metabolic syndrome but also has direct effects on chondrocytes.⁶

The present study aims to investigate the effect of other anthropometric measures on knee OA and estimation of LDH value compared with control.

Experimental

Thirty patients (20 females, 10 males, between 35 and 70 year of age) clinically diagnosed with knee OA, attending rheumatology outpatient clinic in Baghdad teaching hospital between January 2015-June 2015, were selected. Healthy subjects (20 females, 10 males) of similar age group were selected as control. The OA was diagnosed based on physical examination, laboratory results and radiological findings. Blood was collected in a red vial and was centrifuged to separate serum from it and stored until the assay time.

Measurement of BMI

BMI was calculated in kg m^2 for the male and female groups, classifying as normal ($< 25 \text{ kg m}^2$), overweight (25 and $< 30 \text{ kg m}^2$) and obese (30 kg m^2 or more). Waist and hip was measured for every patient and control according to world health organization (WHO) criteria.⁷

Table 1. Demographic features and anthropometric measurements of the patient and control groups.

Characteristics	Male (patient)	Male (control)	p-value	Female (patient)	Female (control)	p-value
Number	10	10	--	20	20	-
Age (Years)	48.85±11.0	46.7 ± 10.2	0.34*	44.84±7.17	42.33±7.55	0.63*
BMI (Kg m ²)	29.9 ± 2.0	23.9±2.1	0.001	34.37±2.50	25.39±0.50	0.001
WHR	0.80± 0.04	0.70±0.04	0.001	0.88±0.05	0.72±0.04	0.001

* Not significant

Assay of serum lactate dehydrogenase

The concentration of serum LDH levels were determined by using kits from Randox, U.K.

Statistical Analysis

Values were calculated as mean ± SD and the statistical analysis was done using SPSS software and Microsoft Excel 2010. The *p*-value of less than 0.01, 0.001 was considered as statistically significant.

Results and discussion

The demographics of the present study are shown in Table 1. Twenty of the patients were female and ten were male, while twenty of the control patients were female and ten were male. The control groups had lower BMI and WHR and were younger than the knee OA.

The mean levels of serum LDH of the patient group is 253±55.7, whereas that of the control group is 161.4±23.9. This indicates that there is highly significant difference between the patients and control groups (*p* = 0.01).

Obesity is of particular interest amongst the risk factors for knee osteoarthritis. The effect of obesity on osteoarthritis is associated with the greater load that is observed in the lower extremities. It is possible that an excessive body mass for prolonged periods may increase the risk of subsequently developing knee OA and worsening of the disease.⁸ In present study we have observed that being overweight or obese has a strong association with knee OA. High BMI is a well-known risk factor for knee OA and overweight has been found to precede the disease in the knee. Contact stress in knee-joint cartilage is a significant predictor of developing symptoms that are interpreted to indicate the presence of knee OA. Obesity has been consistently shown to be higher risk factor for knee OA for in the case of women than in the case of men.

In their large case-control study, Holliday et al investigated by using BMI the effects of obesity and other anthropometric measurements associated with obesity on severe knee OA and HOA (Hip osteoarthritis).⁹ It has been observed that higher WC (waist circumference) and HC hip circumference values were associated with the risk of development of knee and hip OA, however, this association is lower in comparison to that with the BMI. When only women were evaluated, the HOA risk was observed to be associated with the waist: hip ratio.¹⁰

LDH is an enzyme that helps facilitate the process of turning sugar into energy for cells to use. In inflammatory conditions like RA, OA, LDH may be released into the bloodstream causing the levels to increase and higher levels of LDH in the blood indicate acute or chronic cell damage.¹¹

Veys et al had shown that cases of rheumatoid arthritis had high LDH activity both in cell-free fluid and in cellular material.¹² In our study, we have observed a significant increase in serum LDH level in patients with OA in comparison with that in control groups.

From previous reports, degenerative joint diseases are deemed to be associated with increased LDH activity in the synovial fluid. In order to verify the distribution of LDH, Eveline et al have made a study to examine healthy and degenerative stifle joints for the goal of clarifying the origin of LDA in synovial fluid through many technical means, such as transmission electron microscopy (TEM), immunolabeling and enzyme cytochemistry. And then all techniques corroborated the presence of LDH in chondrocytes and in the interterritorial matrix of degenerative stiff joints. Whereas LDH is retained in healthy cartilage due to permeability limitations, it is released into synovial fluid through abrasion as well as through unrestricted diffusion as a result of degradation of collagen and increased water content in degenerative joints.¹³

Other studies have LDH levels in serum and synovial fluid of osteoarthritic patients.^{14,15} LDH is an enzyme that catalyses the conversion of pyruvate to lactate and was found to be elevated in the synovial fluid of osteoarthritic joints.

Conclusion

These results indicate that obesity is a significant risk factor for the development of knee OA, and that the association is stronger for women than for men. LDH have become key targets in the development of the diagnosis and treatment of osteoarthritis, and significant progress has been made over the decades.

References

- ¹Qazi, N., Ruqaya A., International Journal of Science and Research (IJSR), 2013, 4, 1069-1072.
- ²Mansi, G., Rutwa, C., Saini, H. B., *Inter. J. Biomed. Res.*, **2015**, 6, 25-28.
- ³Brown, J. E., Cook, R. J., Lipton, A., Coleman, R. E., *Clin. Cancer Res.*, **2012**, 18, 6348-55.

- ⁴Akune, T., *Clin Calcium*, **2014**, *24*, 695-701.
- ⁵Toivanen, A. T., Heliovaara, M., Impivaara, O., Arokoski, J. P., Knekt, P., Lauren, H., *Rheumatology (Oxford)*, **2009**, *49*, 308-14.
- ⁶Simopoulou, T., Malizos, K. N., Iliopoulos, D., *Osteoarthr. Cartil.*, **2007**, *15*, 872-83.
- ⁷Bray, G.A., *Ann. N.Y. Acad. Sci.*, **1987**, *499*, 14-28.
- ⁸Sulsky, S. I., Carlton, L., Bockmann, F., Ellegast, R., Glitsch, U., Hartmann, B., *PLOS ONE*, **2012**, *7*, 315-21.
- ⁹Holliday, K. L., McWilliams, D. F., Maciewicz, R. A., Muir, K. R., Zhang, W., Doherty, M., *Osteoarthr. Cartil.*, **2011**, *19*, 37-43.
- ¹⁰Deniz, D., Sibel, E., Aytul, Ç., Mehmet, S., Başak, K., Timur, G., İsmail, Ö., Gül, M. and Hatice, K., *J. PMR Sci.*, **2015**, *18*, 107-114.
- ¹¹Rong, Y., Wu, W., Ni, X., Kuang, T., Jin, D., Wang, D., *Tumor Biol.*, **2013**, *34*, 1523-30.
- ¹²Veys, E. M., Wieme, R. J., **1968**, *Ann. Rheum. Dis.*, *27*, 569-576.
- ¹³Walter, E. L., Spreng, D., Schmöckel, H., Schawalder, P., Tschudi, P., Friess, A. E., Stoffel, M. H., *Histochem Cell Biol.*, **2007**, *128*, 7-18.
- ¹⁴Hurter, K., Spreng, D., Rytz, U., Schawalder, P., Ott-Knüsel, F., Schmöckel, H., *Vet. J.*, **2005**, *169*, 281-285.
- ¹⁵Krachler, M., Domej, W., (2001). *Biol. Trace Elem. Res.*, **2001**, *79*, 139-148.

Received: 24.01.2016.

Accepted: 25.02.2016.